New enhancement strategies for plasmon-enhanced fluorescence biosensors

Dissertation

zur Erlangung des Grades

“Doktor der Naturwissenschaften”

am Fachbereich Biologie

der Johannes Gutenberg-Universität

in Mainz

Martin Bauch

geb. am 24.06.1985 in Hoyerswerda

Mainz 2014

Dekan:

1. Berichterstatter:

2. Berichterstatter:

Tag der mündlichen Prüfung: 19.11.2014

Abstract

This thesis investigates metallic nanostructures exhibiting surface plasmon resonance for the amplification of fluorescence signal in sandwich immunoassays. In this approach, an analyte is captured by an antibody immobilized on a plasmonic structure and detected by a subsequently bound fluorophore labeled detection antibody. The highly confined field of surface plasmons originates from collective charge oscillations which are associated with high electromagnetic field enhancements at the metal surface and allow for greatly increased fluorescence signal from the attached fluorophores. This feature allows for improving the signal-to-noise ratio in fluorescence measurements and thus advancing the sensitivity of the sensor platform. In particular, the thesis presents two plasmonic nanostructures that amplify fluorescence signal in devices that rely on epifluorescence geometry, in which the fluorophore absorbs and emits light from the same direction perpendicular to the substrate surface.

The first is a crossed relief gold grating that supports propagating surface plasmon polaritons (SPPs) and second, gold nanoparticles embedded in refractive index symmetric environment exhibiting collective localized surface plasmons (cLSPs). Finite-difference time-domain simulations are performed in order to design structures for the optimum amplification of established Cy5 and Alexa Fluor 647 fluorophore labels with the absorption λ_{ab} and emission wavelengths λ_{em} in the red region of spectrum. The design takes into account combined effect of surface plasmon-enhanced excitation rate at λ_{ab}, directional surface plasmon-driven emission at λ_{em} and modified quantum yield for characteristic distances in immunoassays. Homebuilt optical instruments are developed for the experimental observation of the surface plasmon mode spectrum, measurements of the angular distribution of surface plasmon-coupled fluorescence light and a setup mimicking commercial fluorescence reading systems in epifluorescence geometry.

Crossed relief grating structures are prepared by interference lithography and multiple copies are made by UV nanoimprint lithography. The fabricated crossed diffraction gratings were utilized for sandwich immunoassay-based detection of the clinically relevant inflammation marker interleukin 6 (IL-6). The enhancement factor of the crossed grating reached $EF \approx 10^2$ when compared to a flat gold substrate. This result is comparable to the highest reported enhancements to date, for fluorophores with relatively high intrinsic quantum yield of $\eta_0 \approx 0.3$. The measured enhancement factor excellently agrees with the predictions of the simulations and the mechanisms of the enhancement are explained in detail. Main contributions were the high electric field intensity enhancement at λ_{ab} (30-fold increase) and the directional fluorescence emission at λ_{em} (4-fold increase) compared to a flat gold substrate.

Collective localized surface plasmons (cLSPs) hold potential for even stronger fluorescence enhancement of $EF \approx 10^3$, due to higher electric field intensity confinement. cLSPs are established by diffractive coupling of the localized surface plasmon resonance (LSPR) of metallic nanoparticles and result in a narrow resonance. Due to the narrow resonance, it is hard to overlap the cLSPs mode with the absorption and emission bands of the used fluorophore, simultaneously. Therefore, a novel two resonance structure that supports SPP and cLSP modes which overlap with λ_{ab} and λ_{em}, respectively, was proposed. It consists of a 2D array of cylindrical gold nanoparticles above a low refractive index polymer and a silver film. A structure that supports the proposed SPP and cLSP modes was prepared by employing laser interference lithography and the measured mode spectrum was compared to simulation results.

List of abbreviations

SPP	Surface plasmon polariton
LSP	Localized surface plasmon
1D	One-dimensional
2D	Two-dimensional
PEF	Plasmon-enhanced fluorescence
EF	Enhancement factor
cLSP	Collective localized surface plasmon
SPR	Surface plasmon resonance
LSPR	Localized surface plasmon resonance
SAM	Self-assembled monolayer
BRE	Bio-recognition element
SPCE	Surface plasmon coupled emission
SPFS	Surface plasmon fluorescence spectroscopy
FDTD	Finite-difference time-domain
PML	Perfectly matched layer
AFM	Atomic force microscopy
SEM	Scanning electron microscope
IL-6	Interleukin 6
c-AB	Capture antibody
d-AB	Detection antibody
SA	Streptavidin
PBS	Phosphate buffered saline
FWHM	Full width at half maximum

Table of contents:

1 Introduction

1.1 Biosensors

The detection of trace amounts of analytes such as biomarkers, pathogens and toxins are important challenges in medicine, food science and water control. A prominent example in food and water control is the detection of pathogens like *E. Coli* [1-3]. Clinical importance of biosensors include early detection and identification of pathogens, in time for appropriate treatments before level of toxins produced by the infectious agent is too high or resistance develops [4]. Highly sensitive biosensors are also utilized for cancer diagnostics, for instance prostate cancer, that can be efficiently detected by cancer-biomarkers such as prostate specific antigen (PSA) which also allows early identification of relapse after therapy [5, 6]. Another example for early disease diagnosis is the detection of interleukin 6 (IL-6), a marker indicating sepsis [7], that subsequently affects the success of therapy and survival. Biosensors are very promising tools to address these needs for their rapid detection and high sensitivity.

In general, biosensors consist of a biointerface with recognition elements for specific interaction with an analyte and a transducer that transforms this binding event into an electrical signal. Possible recognition elements can be antibodies, enzymes, peptides and nucleic acids, that bind specifically to a certain analyte. There is a variety of transducers, with which the binding of an analyte to the biorecognition element can be measured. For example, detection of changes in electrical parameters by impedance measurements or other physical properties such as light intensities with a photodiode or weight changes by a quartz crystal microbalance, among numerous others. In addition, chemically transducers have a broad field of application [8]. The broad variety of biosensors can be classified by the analyte to be detected or the readout system, as depicted in the scheme shown in Figure 1.1. Continuous, real-time and in vivo measurements can be realized with biosensors, furthermore allow monitoring for extended periods [9]. In addition, biosensors give the possibility of high throughput in microarray biosensors enabling the detection of multiple analytes in parallel [10].

Optical biosensors based on surface plasmons shown superiority to other approaches due to its rapid and highly sensitive response [1]. There are two detection schemes utilizing surface plasmons for biosensing, direct label-free detection and where labels are used for further amplification of the response. In label-free detection, the surface plasmons change their optical resonance wavelength when an analyte binds to the surface and thus a change in refractive index around the metal

interface occurs. The wavelength change of the resonance can be accurately monitored [11, 12] and information on binding events can be gathered.

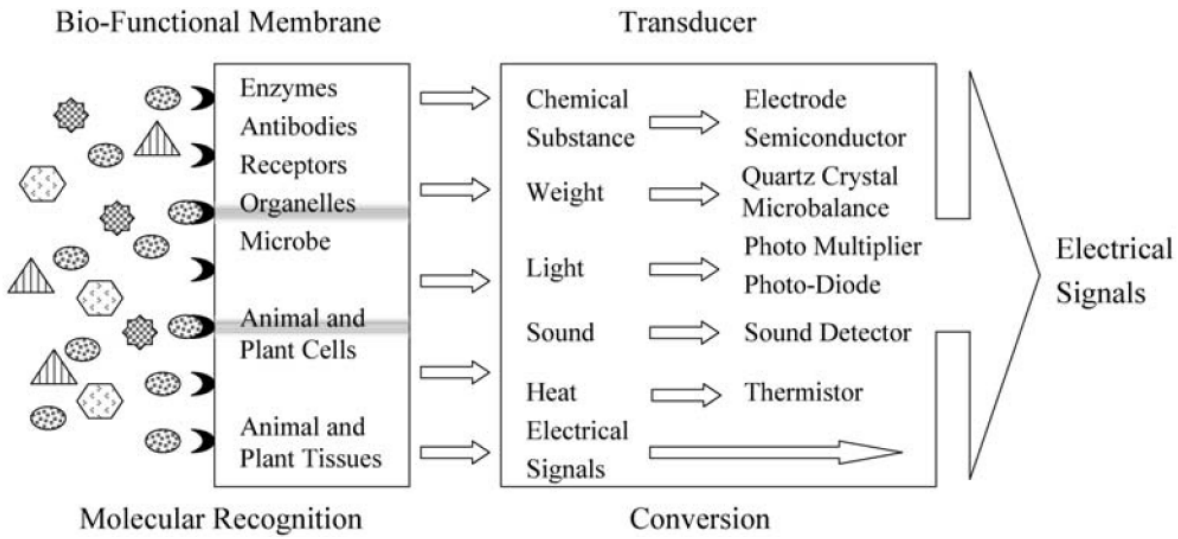

Figure 1.1 Schematic of a biosensor (graphic from [13]). Reprinted figure with permission from H. Nakamura et al., Analytical and Bioanalytical Chemistry, vol. 377, pp. 446-468, 2003, http://dx.doi.org/10.1007/s00216-003-1947-5 .

Detection of bound analytes decorated with a fluorescence label to a noble metal surface exhibiting surface plasmons is a widely applied method [14]. In this detection scheme, referred to as plasmon-enhanced fluorescence (PEF), one takes advantage of the confined field close to noble metal surfaces and consequently an enhanced fluorescence signal from fluorescence label. In this thesis we will focus on detection with fluorescence labels, owing to its greatly enhanced sensitivity compared to label-free detection [1, 6, 15].

1.2 Surface plasmons

Surface plasmons originate from free collective charge oscillations on metallic surfaces. There are two types of plasmon modes on metallic surfaces, namely localized surface plasmons (LSP) and propagating surface plasmons also referred to as surface plasmon polaritons (SPP). Localized surface plasmons are observed at optical wavelength for subwavelength-sized particles, while SPPs are observed on flat or corrugated continuous surfaces.

1.2.1 Localized surface plasmons

Localized surface plasmons can be excited directly by an incident light beam. The oscillating electromagnetic field associated with the incident light interacts with the conduction electrons in the metal particle and displaces them with respect to the ionic lattice of the metal. Upon displacement of the electrons, an attracting force arises that pulls the electrons back into equilibrium. Thus the metal nanoparticle can be seen as an oscillating system, where the light represents an external force, which drives an oscillator. As a typical oscillating system, metallic nanoparticles exhibit resonance frequencies. The resonance frequency (or resonance wavelength) is dependent on the size, the shape, the metal used and the dielectric environment surrounding the metal nanoparticle. Highest fields at the surface of nanoparticles can be observed when the incident light has the same wavelength as the resonance wavelength.

The by far simplest particle is a sphere, that can be analytically described by Mie-theory [16]. Mie theory describes the electromagnetic field enhancement within and out of the particle and allows calculation of the scattering cross section σ_{sca}, absorption cross section σ_{abs} and extinction cross section σ_{ext}. The scattering cross section describes the ability to scatter the incident light into different directions with respect to the incident plane wave, while the absorption cross section describes the absorption of energy within the particle. The extinction cross section, also called total cross section is given as the sum of both:

$$\sigma_{ext} = \sigma_{sca} + \sigma_{abs} \tag{1.1}$$

When dividing the cross section by the cross-sectional area of a particle one achieves the coefficient Q [17]. This coefficient describes how much bigger or smaller the actual interaction area of light with a particle is. In Figure 1.2 the extinction, scattering and absorption coefficient of a gold sphere (diameter $D = 100\ nm$) are shown.

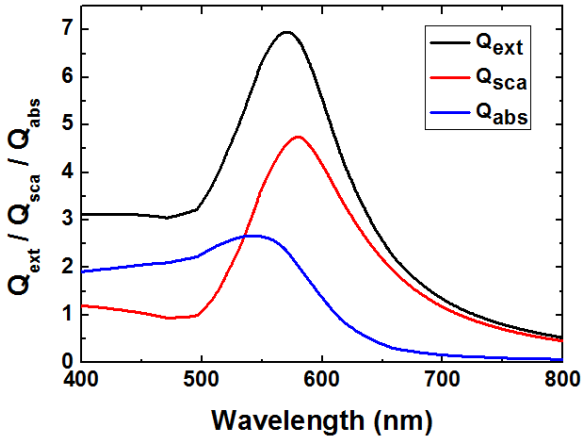

Figure 1.2 Wavelength dependent extinction coefficient Q_{ext}, scattering coefficient Q_{sca} and absorption coefficient Q_{abs} of a gold sphere (diameter $D = 100\,nm$) in aqueous environment (data calculated with MiePlot4210).

It can be seen that the extinction coefficient peaks at the wavelength of $\lambda_{LSPR} = 570\,nm$ and has an extinction coefficient of $Q_{ext} = 7$, which suggests that the particle interacts with a much bigger area, than its actual size is. This fact is illustrated in Figure 1.3.

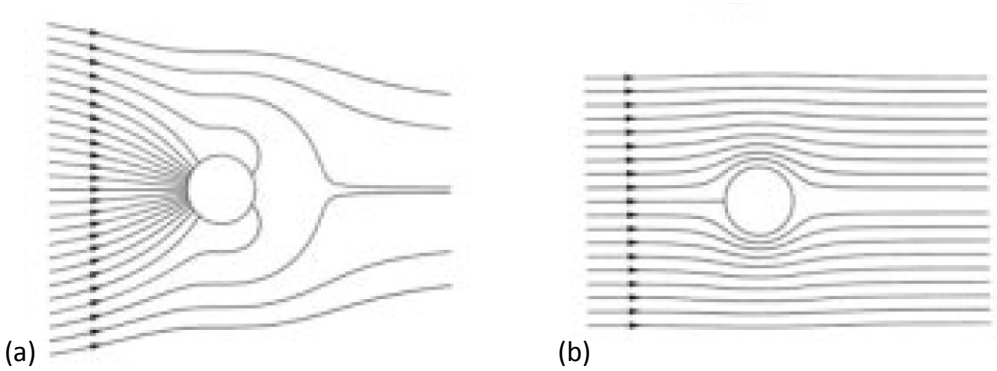

Figure 1.3 Poynting vector lines for spherical particles in (a) resonance and (b) off resonance (graphics from [18]). Reprinted figure with permission from C. F. Bohren et al., Absorption and Scattering of Light by Small Particles, Wiley-VCH Verlag GmbH & Co. KGaA.

In Figure 1.3 (a) the interaction of an incident plane wave with a spherical particle in resonance is illustrated. The lines are indicating the Poynting vector and are a measure of the energy flux. It can be seen that the Poynting vector lines are bent into the particle and therefore a much bigger area is interacting with the incident light, than the actual particle size. In Figure 1.3 (b) the situation is shown for a different wavelength, where no resonance occurs and thus the interaction area is much smaller. The influence of the dielectric environment and the sphere size on the resonance position is illustrated in Figure 1.4.

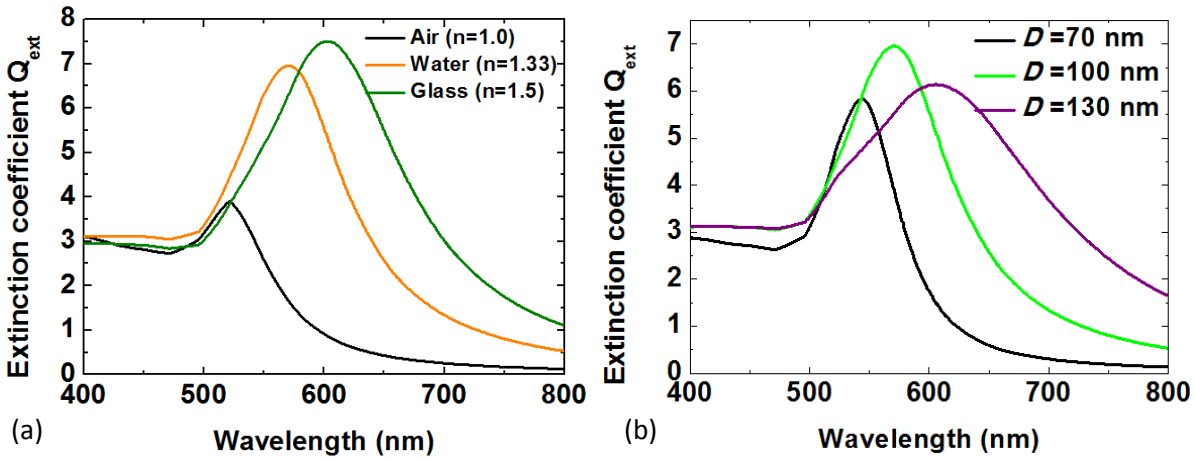

Figure 1.4 (a) Influence of the refractive index of the surrounding medium on the resonance position of extinction coefficient of a gold sphere with diameter $D = 100\ nm$. (b) Influence of gold sphere diameter D on the resonance position of extinction coefficient in aqueous environment ($n = 1.33$) (data calculated with MiePlot4210).

When the refractive index increases, the resonance position shifts to higher wavelengths, as can be seen from Figure 1.4 (a) (data shown for gold sphere with diameter $D = 100\ nm$). In addition to the shift, the peak value of the extinction coefficient is increasing with refractive index. Figure 1.4 (b) illustrates, that the resonance position shifts to higher wavelengths, when the particle diameter$D$ increases (data shown for gold sphere in aqueous environment). The dependency of resonance position on dielectric environment and the particle size, though only been shown for gold spheres, is valid for all kinds of plasmonic nanoparticles.

A simpler formalism than Mie theory, to predict the optical properties of spherical particles is the quasi static approximation [17]. In this approximation it is assumed that the wavelength of the incident light is much larger than the particle diameter D, hence the electric field varies only in time in the volume occupied by the particle, but does not vary in space. By using such approximation it can be shown, that the electric field E outside a metal sphere decays with $\propto D^3/d^3$, where d is the distance from the metal surface.

1.2.2 Surface plasmon polaritons

In general, surface plasmons can be excited, when the real part of the dielectric function of the metal ε_m' is negative and the absolute value is larger than the dielectric function of the dielectric $\varepsilon_d$on top of the metal [19].The dispersion relation of surface plasmon polaritons on a flat metal surface is given as [20]:

$$k_{SPP} = k_0 \sqrt{\frac{\varepsilon_m \varepsilon_d}{\varepsilon_m + \varepsilon_d}} \tag{1.2}$$

with $\varepsilon_m = \varepsilon_m' + i\varepsilon_m''$ the complex frequency ω dependent dielectric function of a metal, where ε_d is the dielectric function of the dielectric above the metal and k_0 is the vacuum wave vector. One can rewrite this equation into a complex and an imaginary part of the propagation constant under the assumption that ε_d is real and $\varepsilon_m'' < |\varepsilon_m'|$ [20]:

$$k_{SPP} = k_{SPP}' + ik_{SPP}'' \tag{1.3}$$

$$k_{SPP}' = k_0 \sqrt{\frac{\varepsilon_m' \varepsilon_d}{\varepsilon_m' + \varepsilon_d}} \tag{1.4}$$

$$k_{SPP}'' = k_0 \left(\frac{\varepsilon_m' \varepsilon_d}{\varepsilon_m' + \varepsilon_d} \right)^{3/2} \frac{\varepsilon_m''}{2(\varepsilon_m')^2} \tag{1.5}$$

The propagation length $L_P$of SPPs on the metal surface is defined as the length of propagation until the electric field intensity of the SPPs decreases by a factor of 1/e and is given as [20]:

$$L_P = \frac{1}{2k_{SPP}''} \tag{1.6}$$

It can be seen that the propagation length is inversely proportional to ε_m'', that can be directly related to the absorbed power P_{abs} in a metal as [21]:

$$P_{abs} \propto \varepsilon_m'' |E|^2 \tag{1.7}$$

The electric field amplitude of the SPPs decays exponentially normal to the metal surface into the dielectric. The penetration (skin) depth is the length at which the electric field amplitude decreases to 1/e and is given as [20]:

$$z_p = \frac{\lambda}{2\pi} \sqrt{\frac{|\varepsilon_m'| + \varepsilon_d}{\varepsilon_d^2}} \tag{1.8}$$

To excite SPPs with light, energy and momentum of the incident light must be matched with those of the surface plasmon. In Figure 1.5 (c) the dispersion relation of SPPs on an air/gold interface is shown. In addition, the dispersion relation of light in air is shown. It is seen that both dispersion

relations do not intersect at any point, which means that one cannot excite SPPs by shining light directly at a flat meal surface. The in-plane momentum component of the incident light under a certain angle θ is given by:

$$k_x = \sqrt{\varepsilon_d} k_0 \sin\theta \qquad (1.9)$$

To excite SPPs an additional momentum is needed. By shining light to a prism with dielectric function ε_P with $\varepsilon_P > \varepsilon_d$ the momentum can be increased and is expressed as:

$$k_{x,prism} = \sqrt{\varepsilon_p} k_0 \sin\theta \qquad (1.10)$$

A possible realization of this prism coupling to SPPs based on attenuated total reflection (ATR) in an arrangement called Kretschmann configuration [22] is shown in Figure 1.5 (a). In this configuration, the base of a prism is coated with a metal. When light is shining at a higher angle than the critical angle, an evanescent field can penetrate the metal and excite SPPs at the metal dielectric interface. Figure 1.5 (c) depicts that the additional momentum Δk can lead to an intersection point of the light inside the prism and the dispersion relation of the surface plasmons, therefore describes the resonance position of surface plasmons.

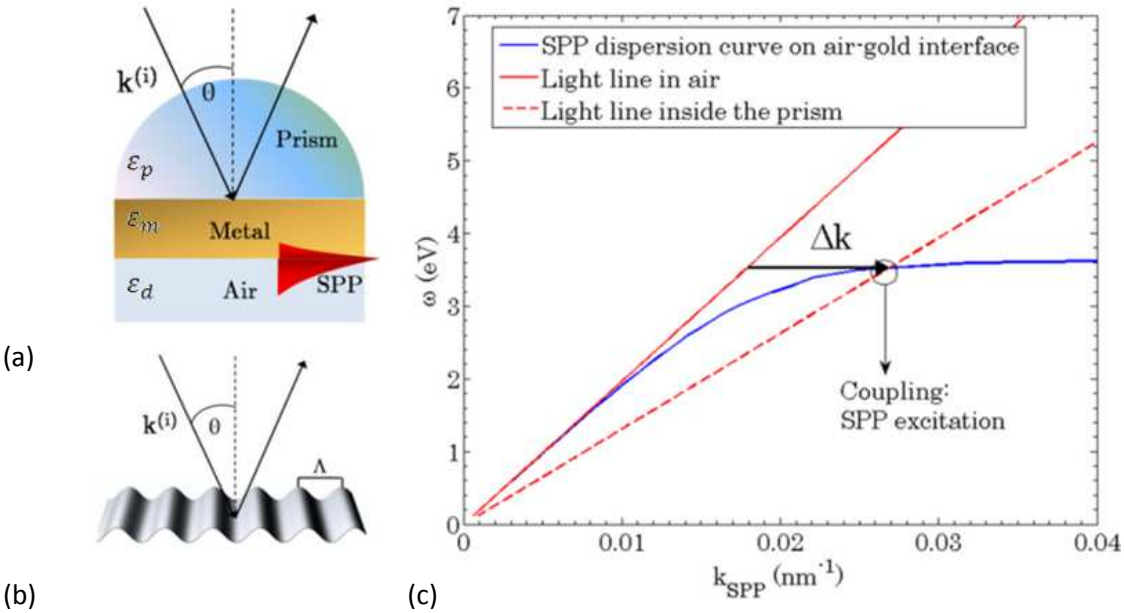

Figure 1.5 (a) Excitation of surface plasmons by Kretschmann configuration, (b) excitation of plasmons by grating, (c) dispersion relation of surface plasmon polaritons (SPPs) and of light in air and prism (graphics from [23]).

The distance dependent electric field intensity enhancement $|E/E_0|^2$ for SPPs on a gold-water interface excited by Kretschmann configuration is shown in Figure 1.6. The simulation was performed at wavelength $\lambda = 633\ nm$ for resonance angle $\theta = 57\ deg$ and an off resonance angle $\theta = 48\ deg$. The distance d is given from the gold surface and optical constants are taken from literature [24]. The thickness of the gold metal film is 50 nm. The highest electric field intensity enhancement is around $|E/E_0|^2 = 19$ close to the gold water interface.

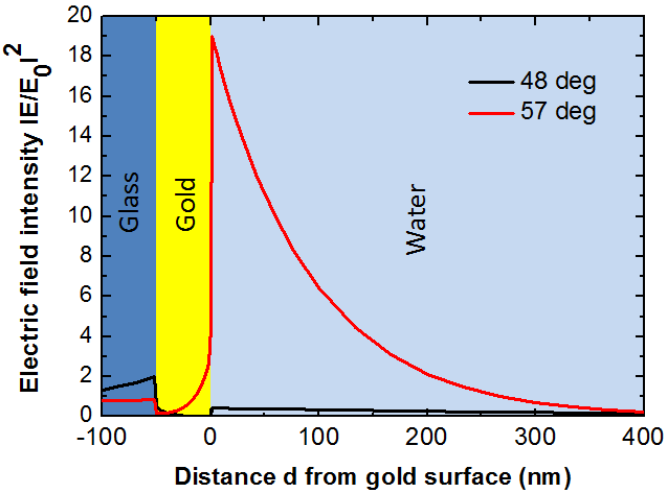

Figure 1.6 Distance dependent electric field intensity $|E/E_0|^2$ at $\lambda = 633\ nm$ calculated for Kretschmann configuration at resonance angle$\theta = 57\ deg$ and off resonance angle $\theta = 48\ deg$.

Another method of exciting SPPs is by the use of a grating (see Figure 1.5 (b)), where the metal surface is corrugated with a certain period Λ. The grating can increase the momentum of the incident light by a grating vector $k = (2\pi)/\Lambda$. In Figure 1.7 (a) a 2D grating with Cartesian coordinates and spherical angles is shown. SPPs can be excited on a grating when the length of the SPP wave vector k_{SPP} is equal to the length of the sum of the grating vectors and the in-plane component of the incident light. This situation is illustrated in Figure 1.7 (b) as a vector diagram.

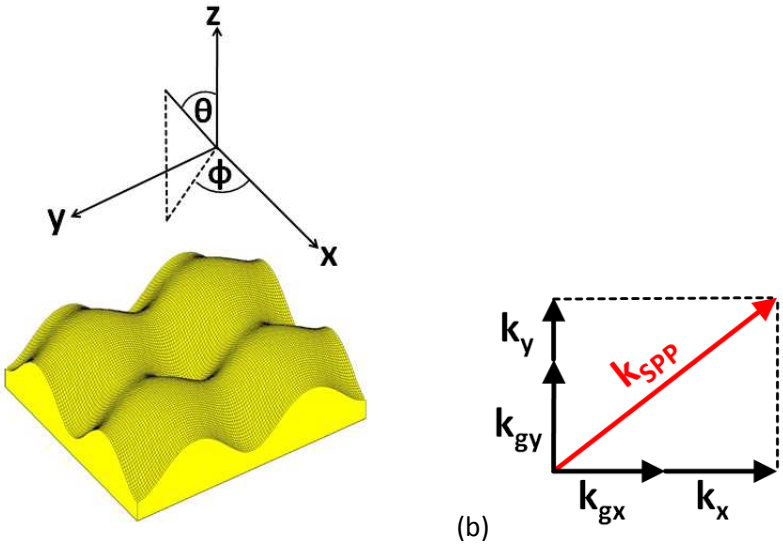

(a) (b)

Figure 1.7 (a) Sketch of a 2D grating with Cartesian coordinates and spherical angles. (b) Vector diagram for the excitation of SPPs.

By setting the squared length of the wave vector of the surface plasmons k_{SPP} (see Eq. (1.2)) equal to the squared length of grating wave vector and the wave vector of the incident light one achieves the following equation [25]:

$$k_{SPP}^2 = (k_{gx} + k_x)^2 + (k_{gy} + k_y)^2 \qquad (1.11)$$

with the grating vector k_{gx} in x-direction:

$$k_{gx} = m\frac{2\pi}{\Lambda} \text{for} \qquad m = 0, \pm 1, \pm 2, \ldots \qquad (1.12)$$

and the grating vector k_{gy}in y-direction:

$$k_{gy} = n\frac{2\pi}{\Lambda} \qquad \text{for} \qquad n = 0, \pm 1, \pm 2, \ldots \qquad (1.13)$$

where m and n are the grating orders and are written in the following notations (m, n). For reasons of simplicity, the period Λ in x-direction and y-directions was chosen to be the same. The in-plane component of the wave vector of the incident light in x-direction k_x is given as:

$$k_x = n_d k_0 \sin\theta \cos\varphi \qquad (1.14)$$

and in y-direction as:

$$k_y = n_d k_0 \sin\theta \sin\varphi, \qquad (1.15)$$

where n_d is the refractive index of the material above the grating and $k_0 = \frac{2\pi}{\lambda_0}$ is the vacuum wave vector. For normal incident light $(\theta = 0, \varphi = 0)$ and using the real part of the SPP wave vector k'_{SPP} only, equation Eq. (1.11) simplifies to:

$$\Lambda = \frac{\lambda_0 \sqrt{\mathrm{m}^2 + \mathrm{n}^2}}{\sqrt{\frac{\varepsilon'_\mathrm{m}\varepsilon_\mathrm{d}}{\varepsilon'_\mathrm{m}+\varepsilon_\mathrm{d}}}} \tag{1.16}$$

With this equation one can calculate which period Λ to choose for a grating, to get the desired resonance frequency at λ_0. For a 1D grating and thus n=0, the equation yields:

$$k_{SPP}^2 = m^2 k_g^2 + 2mk_g k_0 \sin\theta \sin\varphi + k_0^2 sin^2\,\theta \tag{1.17}$$

Surface plasmons can be excited on a big variety of gratings, including 1D sinusoidal grating [26-30], 1D groove gratings [31, 32], nanoparticles on noble metal films [33] and nanoholes [34, 35] in a continuous metal film. Let us note that the resonance condition defined by Eq.(1.11) is changed depending on the degree of perturbation of the surface. While for small amplitudes the resonance position can be nicely predicted, for bigger amplitudes the resonance position shifts to a different resonance wavelength.

1.3 Mechanisms of plasmon-enhanced fluorescence

Fluorescence is the spontaneous emission of light of a system relaxing from an electronically excited state to its ground state. Systems which exhibit fluorescence are called fluorophores. Fluorophores are excited at a certain wavelength λ_{ab} and emit light at a higher or equal wavelength λ_{em}. The difference between λ_{ab} and λ_{em} is called the Stokes-shift. Fluorescence can be found in various systems such as organic molecules, polymers and quantum dots. The excitation and emission rate of a fluorophore can be dramatically changed when it is brought in the vicinity of a metallic nanostructure. There are three mechanisms that can change the behavior of the fluorophore [36, 37] and enhance the emitted fluorescence intensity, namely the excitation rate, the change of intrinsic quantum efficiency and the directivity of emitted fluorescence light. The excitation rate describes with which rate a fluorophore is excited from the ground state into an excited state. The excitation rate below saturation is given as [38, 39]:

$$\boldsymbol{\gamma_e} \propto \left|\vec{\boldsymbol{E}}(\boldsymbol{\lambda_{ab}}) \cdot \vec{\boldsymbol{\mu}}_{\boldsymbol{ab}}\right|^2 \tag{1.18}$$

with $\vec{E}(\lambda_{ab})$ the electric field vector at the absorption wavelength λ_{ab} and $\vec{\mu}_{ab}$ the electric absorption dipole moment of the fluorophore. A measure of how much a plasmonic nanostructure can enhance the excitation rate is given by the field intensity enhancement $|E/E_0|^2$ where E_0 is the electric field amplitude in the absence of a nanostructure.

After a fluorophore is excited from a ground to excited state it returns to the ground state by emission of a photon or by a nonradiative process. The ratio of the emitted photons to the number of absorbed photons is called the quantum efficiency η and is always $\eta \leq 1$. The intrinsic quantum efficiency η^0 (fluorophore in homogenous environment) of a fluorophore is defined as [38]:

$$\eta^0 = \frac{\gamma_r^0}{\gamma_r^0 + \gamma_{nr}^0} \ , \tag{1.19}$$

where γ_r^0 is the radiative decay rate and γ_{nr}^0 is the nonradiative decay rate. The superscript 0 denotes the absence of a nanostructure. Let us note that the intrinsic quantum efficiency itself depends on the solution, in which the fluorophore is found [40]. By bringing the fluorophore in the proximity of an interface or a nanostructure, additional decay channels are available and the total decay rate γ_{total} can be written as [41, 42]:

$$\gamma_{total} = \gamma_{abs} + \gamma_{r,plasmon} + \gamma_r^0 + \gamma_{nr}^0 \tag{1.20}$$

with γ_{abs} absorption rate in the metal (also referred to as quenching) and $\gamma_{r,plasmon}$ the emission of light via plasmons. Thus the new modified quantum efficiency can be given as [43]:

$$\eta = \frac{\gamma_{r,plasmon} + \gamma_r^0}{\gamma_{abs} + \gamma_{r,plasmon} + \gamma_r^0 + \gamma_{nr}^0} \tag{1.21}$$

By defining the radiative decay rate of the metal-fluorophore system as $\gamma_r = \gamma_{r,plasmon} + \gamma_r^0$ and using the definition of Eq. (1.19), Eq. (1.21) can be rewritten as [38, 44, 45]:

$$\eta = \frac{\gamma_r \,/\, \gamma_r^0}{\gamma_r/\gamma_r^0 + \gamma_{abs}/\gamma_r^0 + \,(1-\eta^0)\,/\,\eta^0} \tag{1.22}$$

The nonradiative decay rate of the metal-fluorophore system is given as $\gamma_{nr} = \gamma_{abs} + \gamma_{nr}^0$. The excitation and decay process of a metal-fluorophore system is shown in the Jablonski diagram in Figure 1.8.

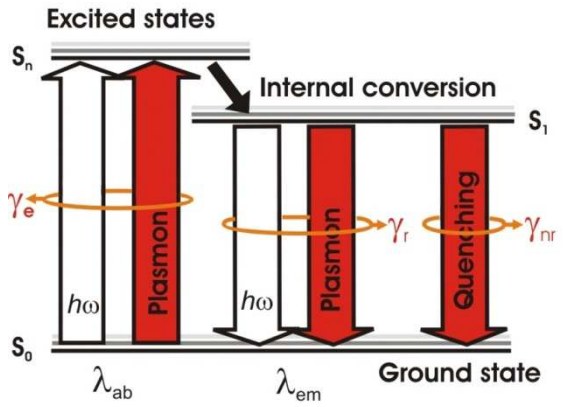

Figure 1.8 Jablonski diagram including the metal fluorophore interaction (graphic from [46]).

The enhancement of quantum efficiency is given as η/η_0. While for high intrinsic quantum efficiency dyes the ratio will be $\eta/\eta_0 < 1$ and thus a decrease of quantum efficiency is achieved. For low intrinsic quantum efficiency dyes the ratio can be $\eta/\eta_0 > 1$ and can give a significant contribution to fluorescence enhancement [44]. The interaction strength of a fluorophore with a metallic nanostructure is highly dependent on the metal-fluorophore distance f. In Figure 1.9 the distance dependent quantum efficiency enhancement η/η_0 for a flat gold surface and a gold nanodisk is shown.

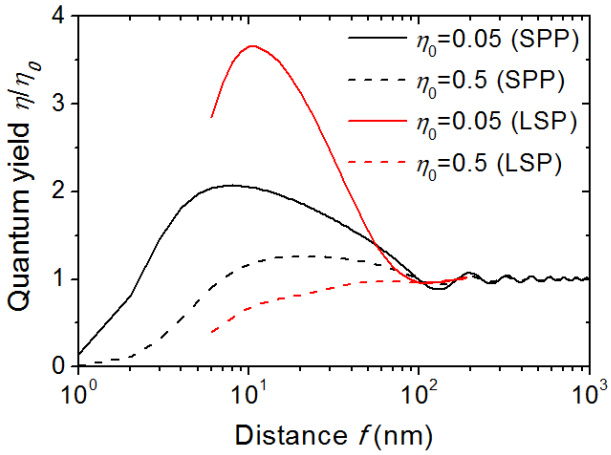

Figure 1.9 Calculated distance dependence of quantum efficiency enhancement η/η_0 for a flat gold surface (black) and a gold nanodisk (red) with disk height 50 nm and disk diameter D =110 nm. The date is shown for two different intrinsic quantum efficiencies η_0 with $\eta_0 = 0.05$ (solid line) and $\eta_0 = 0.5$ (dotted line) (graphic from [46]).

While for small distances f to the metal surface the absorption in the metal (quenching) dominates and thus $\eta/\eta_0 < 1$, for higher distances f one can gain from the modified decay rates of the metal

fluorophore system. For distances higher than $f = 100\,nm$ the influence of the metal to the fluorophore gets negligible and $\eta/\eta_0 \approx 1$.

The life-time τ of an excited state describes, how fast the fluorophore returns back to its ground state. It is related to the decay rates by [42]:

$$\tau = \frac{1}{\gamma_{total}} \tag{1.23}$$

A fluorophore in the vicinity of a metal can have a highly reduced lifetime [42, 47-50].

The third contribution to plasmon enhanced fluorescence is the increase in directivity of emitted fluorescence light. A fluorophore in homogeneous aqueous environment emits isotropic. This can be dramatically changed when the fluorophore is in the vicinity of a plasmonic nanostructure [37, 51-53], where the fluorescence emission can be shaped into certain directions. The directivity $D(\theta, \varphi)$ is defined as [54-56]:

$$D(\theta, \varphi) = \frac{4\pi P(\theta, \varphi)}{\int_0^{\pi} \int_0^{2\pi} P(\theta, \varphi) \sin\theta \; d\varphi d\theta} \tag{1.24}$$

with $P(\theta, \varphi)$ the intensity emitted into a certain spherical angle defined by the polar angle θ and the azimuthal angle φ. The directivity describes the deviation of the fluorescence emission from the isotropic emission. In a typical fluorescence setup the emitted fluorescence light is rather collected in an angle range by a lens, rather than in a single point $P(\theta, \varphi)$. Therefore we define the collection efficiency CE as the ratio of the light collected by a lens divided by the fluorescence light emitted in all directions.

$$CE = \frac{\int_0^{\theta_{max}} \int_0^{2\pi} P(\theta, \varphi) \; \sin\theta \; d\varphi d\theta}{\int_0^{\pi} \int_0^{2\pi} P(\theta, \varphi) \sin\theta \; d\varphi d\theta} \tag{1.25}$$

θ_{max} is the maximum acceptance angle of a collection lens defined by the numerical aperture NA of the lens by:

$$\theta_{max} = asin\left(\frac{NA}{n}\right) \tag{1.26}$$

with n the refractive index of the medium in which the lens is operated. The overall fluorescence enhancement factor EF comprising all the three afore mentioned mechanisms can be written as:

$$EF = \frac{\langle \gamma_e \cdot \eta \cdot CE \rangle}{\langle \gamma_e^0 \cdot \eta^0 \cdot CE^0 \rangle} \quad (1.27)$$

The superscript 0 denotes the absence of a nanostructure and thus represents the case of a fluorophore in a homogenous environment. The brackets ⟨ ⟩ indicate that the average of different polarization directions of the absorptions dipole $\vec{\mu}_{ab}$ and emission dipole $\vec{\mu}_{em}$ moments were taken and different position of the fluorophore close to the nanostructure are considered. This equation gives the enhancement of a fluorophore close to a nanostructure compared to a fluorophore in aqueous environment.

1.4 Surface architectures for immobilization of biomolecules

In biosensors the target analytes to be detected need to be captured at the surface by bio-recognition elements (BRE). The surface architecture should be anti-fouling to minimize non-specific binding, while biological activity of the bound biomolecules is maintained. Surface architectures that fulfill these needs are self-assembled monolayers (SAM), polymer brushes [57] and lipid bilayers, to name a few. The binding of bio-recognition elements to gold surfaces is conventionally realized by self-assembled monolayers. Self-assembled monolayers are formed of molecules that attach to a surface (substrate) from a liquid or gas phase and arrange spontaneously [58]. The ordered 2D, tightly packed and stable nature of these layers is due to intermolecular forces and makes them suitable for a variety of applications [59]. The molecules that build this monolayer consist of three main parts and are illustrated in Figure 1.10. A ligand group, that attaches to the surface, a spacer and a functional group, that can be used for further modification [58]. The ligand group can be chosen according to the substrate it should bind to. For gold and silver surfaces a sulfurhydryl group (-SH) is used.

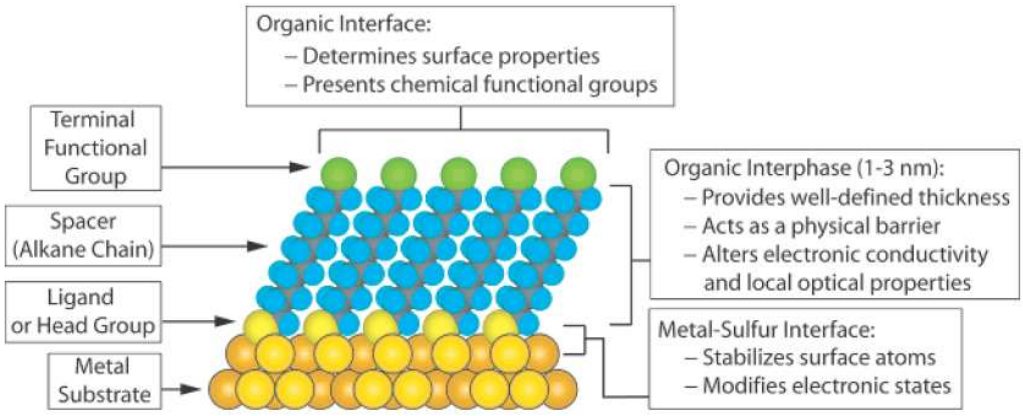

Figure 1.10 Schematic of a self-assembled monolayer of alkane thiols on a metal surface (graphic from [60]). Reprinted figure with permission from J. C. Love et al., Chemical Reviews, vol. 105, pp. 1103-1169, 2005, http://dx.doi.org/10.1021/cr0300789 . Copyright (2005) by the American Chemical Society.

The spacer is used to create a certain distance between the substrate surface and the functional group. The spacer is most commonly an alkane chain, with preferably a short sequence of polyethylene glycol (PEG) group. Alkane thiols are an efficient and mostly favored way to modify noble metal surfaces. The properties of the thiol SAM can have hydrophilic and hydrophobic properties depending on the functional group [58]. A widely used functional group is biotin. The biotin end groups can be efficiently bound to streptavidin which has four binding sites for biotin. The

remaining unbound binding sites of the streptavidin can be used to further bind molecules with biotin tags [61].

It can be shown, that for the binding of streptavidin to a SAM with biotin functional groups it is favorable to mix the SAM with non-biotinylated thiol molecules at a certain ratio. This is due to the fact, that a too dense packed film of biotin binding sites will hinder the binding of streptavidin [62]. A typical mixture for SAMs is alkane thiols with OH-endgroup and biotinylatedalkane thiol with a molar ratio of 1:9, that achieves the maximum binding of streptavidin [62]. The length of the molecules shown in Figure 1.11 can be determined from the bond lengths of the alkanes, taking into consideration the aspects of bond angles. The length for a single bond between two carbon atoms is (120 - 154) pm, carbon to oxygen is (143 - 215) pm and carbon to sulfur bond is (181 - 255) pm [63]. By calculating the sum of the bond lengths of the biotinylatedthiol shown in Figure 1.11 (b) we achieve a length of around 3 nm. In addition it has to be taken into account that the thiols chains assemble under a certain angle to the surface normal to maximize van der Waals interactions [64].

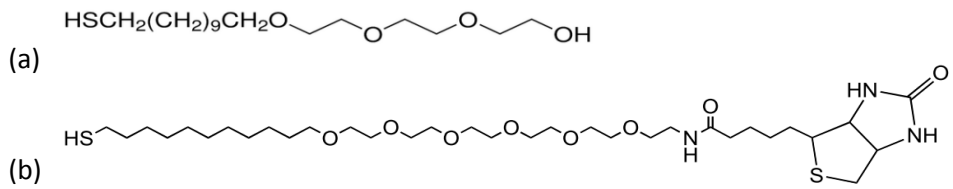

Figure 1.11 Structure of thiol molecules used in the current study. (a) Triethylene glycol mono-11-mercaptoundecyl ether ($C_{17}H_{36}O_4S$) (b) biotinylated PEG alkane thiol ($C_{33}H_{63}N_3O_8S_2$) (graphics obtained from company material data sheets (a) Sigma Aldrich (b) Senso Path Technologies).

Carboxyls as functional groups are widely used for covalently coupling proteins through their terminal primary amine groups.

1.5 Assays for affinity biosensors

Typical bio-recognition elements used in affinity biosensors are antibodies and aptamers [65, 66].The binding of an analyte to an antibody is highly specific and is the principle of immunoassays [67-69]. There are different kinds of immunoassay such as competitive, noncompetitive and direct immunoassays [65]. In noncompetitive immunoassays also called sandwich immunoassay the analyte binds to an antibody immobilized on the sensor surface. The detection of the binding event is realized by a labeled secondary antibody. Antibodies are commercially available for a wide range of biomarkers and make them therefore widely spread materials for sensing [46]. A schematic of a sandwich immunoassay is shown in Figure 1.12.

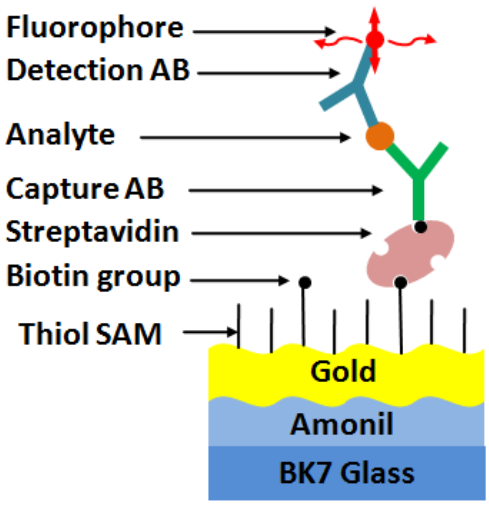

Figure 1.12 Schematic of a sandwich immunoassay.

Antibodies can be immobilized onto a self-assembled monolayer by amine coupling, where an activated carboxyl terminus of the SAM binds to the amine moiety of the antibody [70]. Another approach of binding an antibody to the SAM is through streptavidin, which binds to the biotinylated thiol and has remaining open binding sites for a biotinylated antibody. The analyte is captured by this immobilized antibody (capture antibody). To detect the presence of the analyte, a second fluorescently labeled antibody is used.

The distance of the fluorophore to the metal surface is of special importance. To estimate this distance we need to know the size of the components of the assay. The streptavidin size can be estimated as 4 nm [62]. An IgG molecule was estimated to have a dimension of height=14.5 nm, width=8.5 nm, thickness = 4 nm [26, 71]. By taking into account, that the antibodies are not standing upright and the fluorophore label can be at different position on the detection antibody, the overall distance of fluorophore to metal surface for this kind of assay is around 20 nm [67].

1.6 Langmuir adsorption model

The binding of an analyte A to a biorecognition element B is given by the biomolecular reaction:

$$A + B \underset{k_{off}}{\overset{k_{on}}{\rightleftharpoons}} AB \qquad (1.28)$$

The kinetics of this binding can be written as:

$$\frac{dc_{AB}}{dt} = k_{on} c_A c_B - k_{off} c_{AB} \tag{1.29}$$

where c_A is the free analyte concentration in solution, c_B is the concentration of free binding sites, c_{AB} is the concentration of occupied binding sites of biorecognition element, k_{on} the association rate constant and k_{off} the dissociation rate constant. In equilibrium $dc_{AB}/dt = 0$ and the binding constant K_a can be described by:

$$K_a = \frac{k_{on}}{k_{off}} = \frac{c_{AB}}{c_A c_B} = \frac{1}{K_d} \tag{1.30}$$

The binding constant K_a is inversely proportional to the dissociation constant K_d. The total concentration of initially inserted analyte is $c_{A,0} = c_A + c_{AB}$ and the initial free concentration of biorecognition elements is $c_{B,0} = c_B + c_{AB}$. Eq. (1.30) can be rewritten as:

$$c_{AB} = \frac{c_{A,0} c_B}{K_d + c_B} \tag{1.31}$$

Under the assumption that $c_{A,0} \ll K_d$, which is the case when there are much more binding sites than analytes in solution, $c_{B,0} \approx c_B$ and Eq. (1.31) can be further modified to:

$$c_{AB} = \frac{c_{A,0}}{\frac{K_d}{c_{B,0}} + 1} \tag{1.32}$$

which is also referred to as Langmuir isotherm.

The time dependent association can be correlated to the time dependent detected fluorescence signal $I(t)$ in a fluorescence assay by [72, 73]:

$$I(t) = I_{max}\left(1 - e^{-(k_{on} c_0 + k_{off})t}\right) \tag{1.33}$$

where I_{max} is the maximum intensity for $t \to \infty$, at a given concentration c_0 of dye labeled analyte that is specific captured to a biorecognition element. The above equation indicates, that the fluorescence signal increases faster for higher concentrations c_0 [72]. The time dependent dissociation is given by:

$$I(t) = I_{max} e^{-k_{off} \cdot t} \tag{1.34}$$

Let us note, that afore mentioned equations hold true only, if the mass transfer rate k_m is much bigger than association rate constant $k_m \gg k_{on}$ [74].
The mass transfer rate from a solution in a flow-cell containing a certain analyte can be given as [75-77]:

$$k_m \approx 1.378 \left(\frac{v_{max} D^2}{hL} \right)^{1/3} \tag{1.35}$$

where h and L are the height and the length of the flow cell, D is the diffusion constant and v_{max} is the flow velocity. This means that the biological species under study are transported the fastest to the sensor surface for a high flow rate, a high diffusion constant D and small flow-cell dimensions.

1.7 State-of-the-art plasmon-enhanced fluorescence biosensors

The following section discusses recently applied plasmonic structures for plasmon-enhanced fluorescence. It starts with a review of electric field intensity enhancements provided for various plasmonic structures, followed by the fluorescence enhancement performance.

This chapter is a summary of the paper "Plasmon-Enhanced Fluorescence Biosensors: a Review" [46] authored by Martin Bauch, Koji Toma, Mana Toma, Qingwen Zhang and Jakub Dostalek.

1.7.1 Electric field intensity enhancement

As shown in section 1.3 the excitation rate and thus fluorescence enhancement scales with the electric field intensity enhancement $|E|^2/|E_0|^2$. In enhancement strategies applying plasmon-enhanced fluorescence, the electric field intensity enhancement provides in most cases the largest contribution to plasmon-enhanced fluorescence. The intensity of the initial light is given by $|E_0|^2$, while the electric field intensity at a certain distance to the nanostructure is given by $|E|^2$. The electric field intensity in the literature is usually determined by simulations, but can be experimentally observed by scanning near-field optical microscopy (SNOM).

A crucial parameter for the plasmonic electric field intensity enhancement is the choice or the metal. To compare different materials in terms of their performance in enhancing the electric field intensity a quality factor Q has been defined generally as the ratio between the enhanced field intensity $|E|^2$ on a nanostructure and the incident field intensity $|E_0|^2$ [78]. The Q-factors are

determined by the complex and frequency dependent dielectric function $\varepsilon_m(\omega) = \varepsilon'_m(\omega) + i\varepsilon''_m(\omega)$ of the metals. For spherical nanoparticles the Q-factor can be given as [78]:

$$Q_{Sphere} = \frac{-\varepsilon'_m(\omega)}{\varepsilon''_m(\omega)} \tag{1.36}$$

The Q-factor for SPPs with a dielectric $\varepsilon_d(\omega)$ on top of the metal film is given as [20, 78]:

$$Q_{SPP} = \frac{\varepsilon'_m(\omega)^2 + \varepsilon'_m(\omega)\varepsilon_d(\omega)}{\varepsilon''_m(\omega)\varepsilon_d(\omega)} \tag{1.37}$$

It can be seen that both quality factors are inversely proportional to $\varepsilon''_m(\omega)$, which is associated with absorption in the metal. Therefore in a metal with low absorption (low $\varepsilon''_m(\omega)$), plasmons can propagate longer, resulting in higher electric field intensity enhancements. The figure of merit for SPPs for aluminum, silver and gold is shown in Figure 1.13. In the UV range aluminum is the best material while for higher wavelength silver and gold are better. By far the best material in the higher wavelength range is silver. The drawbacks for silver are the chemical instability, sensitivity to oxidation and consequently the need of an additional protection layer. Therefore gold is typically the metal of choice, as it is chemically stable.

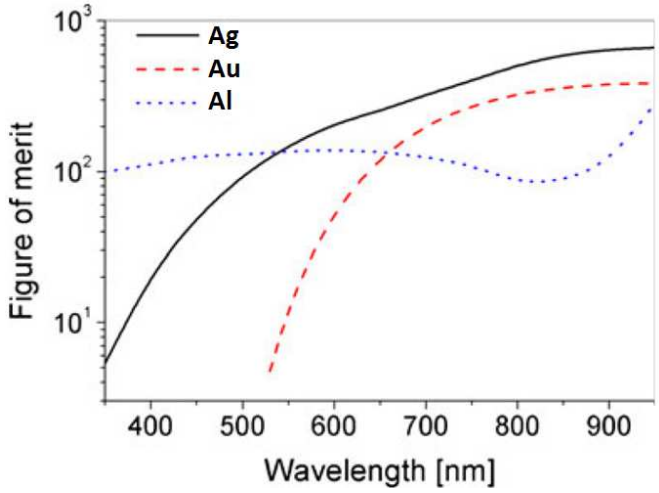

Figure 1.13 Figure of merit of SPPs for Au, Ag and Al (graphic from [46]).

The field intensity enhancement values discussed in the following are preferentially taken from studies where the simulations have been supported by transmission of reflectivity measurements of the structures. It is likely that, if the simulated reflectivity/transmission spectra of a structure is in agreement with the measured one, that also the electric field intensity enhancements agrees with the reality. Special care in simulations must be taken when sharp edges are simulated, as this usually

is not realized experimentally in nanostructures and therefore the field intensity enhancement is overestimated. Several nanostructures are compared in terms of their electric field intensity enhancement (intensities given at a distance from the surface of 10 nm to 20 nm) and are listed in Table 1.1. In addition, the fabrication method and the resonance wavelength are given.

Plasmonic Structure	Schematics	Fabrication	Wavelength	$\|E\|^2/\|E_0\|^2$	Ref.
LRSPP: Flat and corrugated Au films **SPP:** Flat and corrugated Au films	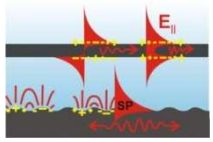	Nanoimprint lithography	λ=630 nm λ=630 nm	~90 ~20	
LSP: Au nanoshell and spherical nanoparticles	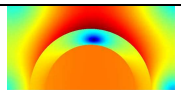 (a)	Chemical synthesis	λ=617 nm	~10	[79]
LSP: Au nanoparticle dimers	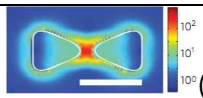 (b)	Electron beam and focused ion beam lithography	λ=780 nm λ=780 nm λ=630 nm	181 ~350 ~100	[44] [80] [81]
SPP and LSP: Au nanodisk and nanoholes arrays	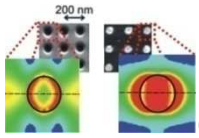 (c)	Electron beam and focused ion beam lithography	λ~630 nm	~10	[82]
LSP: Ag bow tie NP arrays	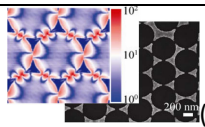 (d)	Colloidal lithography	λ=780 nm	~100	[83]
SPP and LSP: Concentric gratings with nanohole	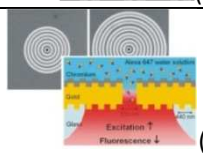 (e)	Electron beam and focused ion beam lithography	λ=633 nm	~10	[37, 52]
cLSP and SPP: Diffractive arrays of cylindrical nanoparticles	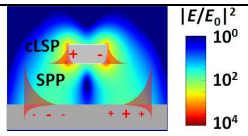	Interference lithography	λ=630-670 nm	~200	[84]

Table 1.1 Summary of electric field intensity enhancements for various structures (table from [46]). Reprinted figure (a) with permission from D. J. Wu et al., Applied Physics B-Laser and Optics, vol. 97, pp. 497-503, 2009, http://dx.doi.org/10.1007/s00340-009-3535-7 . Reprinted figure (b) with permission from A. Kinkhabwala et al., Natur Photonics, vol. 3, pp. 654-657, 2009, http://dx.doi.org/10.1038/nphoton.2009.187 . Reprinted figure (c) with permission from J. Parsons et al., Physical Review B, vol. 79, 073412, 2009, http://dx.doi.org/10.1103/PhysRevB.79.073412 . Copyright (2009) by the American Physical Society. Reprinted figure (d) with permission from F. Xie et al., Nano Research, vol. 6, pp. 496-510, 2013, http://dx.doi.org/10.1007/s12274-013-0327-5 . Reprinted figure (e) with permission from H. Aouani et al., Nano Letters, vol. 11, pp. 637-644, 2011, http://dx.doi.org/10.1021/nl103738d . Copyright (2011) by the American Chemical Society.

1.7.1.1 Flat and corrugated noble metal surfaces

By far the simplest structure is a flat metal film (thickness around 50 nm) on a substrate. As have been already shown, plasmons on such a system can be excited by Kretschmann configuration (see section1.2.2). Field intensity enhancements around $|E|^2/|E_0|^2$=20 at λ=630 nm can be achieved for gold and the field decays exponentially from the interface. The electric field enhancement in dependence of excitation wavelength is shown in Figure 1.14

Another system that can as well be excited by Kretschmann configuration is an even thinner metal film of around 20 nm in a refractive index symmetric environment. The plasmons excited in this system are called long-range surface plasmon polaritons (LRSPP). They are characterized by much narrower resonances compared to SPPs and thus higher electric field intensity. Field enhancements around$|E|^2/|E_0|^2$=90 at λ=630 nm can be reached. The excitation of SPPs on gratings have similar electric field intensity enhancements as excited by Kretschmann configuration, as seen in Figure 1.14.

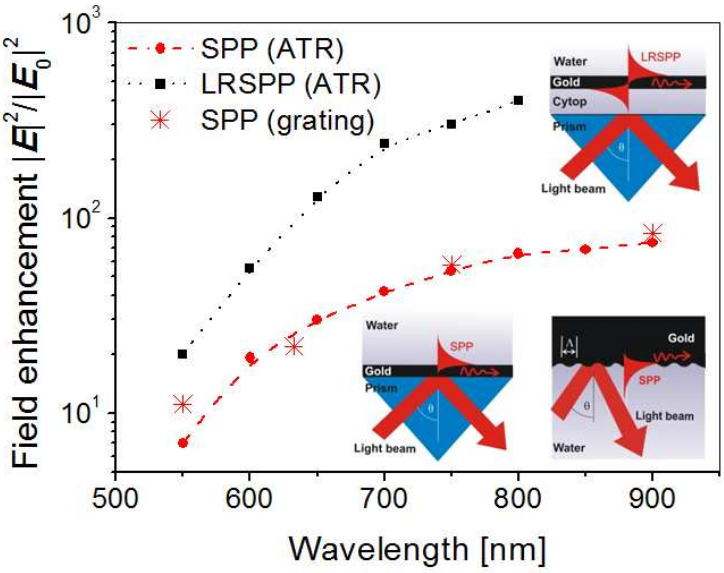

Figure 1.14 Electric field intensity enhancement at distance d=15 nm from the gold surface in dependence on the excitation wavelength for surface plasmons excited by Kretschmann configuration (red circles), SPPs excited by grating (red stars) and long range surface plasmons (black squares)(graphic from [46]).

The electric field of SPPs on a metal surface can be further confined by structuring the surface and consequently higher electric field intensity enhancements can be reached.

This can be done by nanoholes in the gold film [85, 86], which can serve in addition as a grating to excite SPPs. A single nanohole surrounded by a circular grating can yield field enhancement of EF=10 for gold at $\lambda = 633\ nm$ [52] and EF=40 for silver at $\lambda = 585\ nm$ [87].

A narrow gold groove grating (groove width of 60 nm, depth of 90 nm and period Λ=560 nm) at wavelength λ=820 nm shows a field enhancement of $|E|^2/|E_0|^2 \approx 1000$ within the groove [88].

1.7.1.2 Single metallic nanoparticles

Spherical gold nanoparticles are arguably the most studied plasmonic material. A gold sphere in aqueous environment with diameter $D = 20\,nm$ shows a maximum electric field enhancement at the surface of $|E|^2/|E_0|^2 \approx 18$ at a resonance wavelength of $\lambda = 521\,nm$.

Gold nanoshell particles consist of a dielectric core and a gold shell. Surface plasmons can occur at the inner core shell interface and on the outer shell surrounding medium interface. Both plasmon modes can interact with each other and form hybridized modes [89] which can show higher electric field enhancements, than uniform metallic nanospheres [90]. The electric field intensity on a system with core diameter of $D = 80\,nm$ and gold shell diameter $D = 108\,nm$ (see Table 1.1) is $|E|^2/|E_0|^2 \approx 100$ at $\lambda = 617\,nm$ [79].

For spheres the polarization of the initial light is not important, while for nanorods it is significant. Two different plasmon modes are supported depending on the orientation of the nanorod to the incident light polarization [49, 91]. The two modes can be seen by two peaks in the extinction cross section. The resonance at lower wavelength occurs when the light polarization is orthogonal to the long axis, while the resonance at higher wavelength is present, when the light is polarized parallel to the long axis. In this case the light is confined at the ends of the nanorod. Field enhancements of $|E|^2/|E_0|^2 \approx 100$ for a gold nanorod with 28 nm length and 77 nm width on a silicon substrate at $\lambda = 780\,nm$ have been reported [92].

Highest field enhancements for nanoparticles can be achieved at sharp edges. The field enhancement is dependent on the curvature of the tip and decays fast from the surface. Though such systems show high field enhancements, the enhancement occurs only at a small part of the surface of the nanoparticle. An equilateral triangle with side length 100 nm and height 20 nm on a glass substrate shows a field enhancement of $|E|^2/|E_0|^2 > 1000$ at the surface of the tip and resonance wavelength at $\lambda = 514\,nm$.

1.7.1.3 Nanoparticle dimers

Two nanoparticles placed close to each other can form a gap mode in which the electric field intensity is highly confined and increased. The coupling between the particles as well as the strength of the electric field intensity depends crucially on the gap size. Moreover the resonance, that

confines the electromagnetic field in the gap is redshifted when decreasing gap size [89, 93]. The gap mode can be fully exploited when the polarization of the light incident on the dimer is along the gap axis.

The electric field intensity enhancement of a gold nanosphere dimer with sphere diameter $D = 60\,nm$ and gap size 3 nm is $|E|^2/|E_0|^2 \approx 1600$. This enhancement is achieved at a wavelength of $\lambda = 633\,nm$ for light polarization along the dimer axis at a distance of 1 nm away from the surface. The enhancement for the same system is only $|E|^2/|E_0|^2 \approx 16$, when the light polarization is orthogonal to the dimer axis [94].

Two nanorods aligned to their long axis and with a gap size of 1 nm can enhance the electric field intensity up to $|E|^2/|E_0|^2 \approx 10^4$ for wavelength around $\lambda = 750\,nm$ [91].

A system that takes advantage of the high field intensity close to the tips of a nanotriangle and the gap modes of a dimer is a nanotriangle dimer also referred to as bowtie antenna. A gold bowtie antenna with gap size of 20 nm exhibits a field intensity enhancement of $|E|^2/|E_0|^2 \approx 180$, at 780 nm (see Table 1.1). This value is lower than the before mentioned values for dimers, due to the rather big gap size of 20 nm, which makes the structure suitable for fluorescence applications.

1.7.1.4 Arrays of nanoparticles

Nanoparticles placed on a substrate with a certain period Λ can interact via short-range or long-range coupling [89]. The resonance wavelength position and shape can be highly different from the localized surface plasmon resonance (LSPR) of an isolated particle. For short distances (period Λ much below the wavelength λ of the incident light) the particles near-field couple and form gap-modes. A dense packed array of gold nanodisks with spacing of 100 nm showed an electric field intensity enhancement of $|E|^2/|E_0|^2 \approx 10$ at wavelength between $\lambda = 530\,nm$ and $\lambda = 630\,nm$ [82, 95].

An individual nanohole in a continuous metal film shows a localized surface plasmon resonance similar to a nanoparticle and can couple, when arranged into an array [96]. A dense nanohole array with hole diameter of D=90 nm, depth 20 nm and period $\Lambda = 200\,nm$ in a gold film shows an enhancement of $|E|^2/|E_0|^2 \approx 16$ at $\lambda = 600\,nm$ [82].

Higher field intensities can be achieved between the nanoparticles when they are arranged with a smaller gap width and have sharper edges. An array of silver nanotriangles produced by colloidal lithography has shown to enhance the electric field intensity by $|E|^2/|E_0|^2 \approx 100$ at $\lambda = 780\,nm$ [83].

For higher distances (period Λ comparable to the incident light wavelength) the coupling of the dipole moments of the particles can occur in a diffractive manner. The light diffracted by one particle can be collected by the neighbouring and so on. Therefore the light is travelling in the particle plane, which results in high electric field enhancements and sharp resonances [97]. The resonance of the diffractive coupled modes of the nanoparticles also referred to as collective loacalized surface plasmons (cLSPs) depends on the period, the LSPR of the individual particle and the dielectric environment of the substrate and the superstrate [98]. For a gold disk array (with disk diameter D=180 nm, disk height 40 nm and period Λ=640 nm) an electric field enhancement of $|E|^2/|E_0|^2$ ≈2500 at λ=982 nm have been reported [99]. While for normal incident light the in-plane dipole moments of the nanoparticles long range couple, for tilted incident light the out-of-plane dipole moments of the nanoparticles can couple and lead as well to very sharp resonances and highest field enhancements of around $|E|^2/|E_0|^2 \approx 10^3$ for a gold nanodisk array (height 100 nm, diameter D=160 nm period Λ =400 nm) at wavelength around λ=800 nm [100].

1.7.2 Plasmon-enhanced fluorescence

This section discusses the efficiency of metallic structures for plasmon-enhanced fluorescence. It aims at deconvoluting key contributions to plasmon-enhanced fluorescence, namely excitation rate enhancement, increase of intrinsic quantum efficiency and directivity. An overview of structures reported in literature for enhancing the fluorescence intensity of single fluorophores and ensemble of fluorophores will be presented. In Table 1.2 the fluorescence enhancement of selected representative structures is summarized, ranging from continuous metal films, nanoclusters, chemically synthesized nanoparticles to nanoparticles based on lithographic techniques. For every structure presented, the intrinsic quantum efficiency η_0 of the used fluorophore is given, as well as a rough estimate of the directivity D of the emitted fluorescence light. A crucial parameter is the used reference structure, as the enhancement factor EF is highly dependent on it.

1.7.2.1 Flat noble metal surfaces

SPPs on flat metal surfaces can be excited by Kretschmann configuration in order to enhance the electric field intensity close to the dielectric-metal interface. When a fluorophore is attached to the metal surface, the excitation rate is increased due to the enhanced electric field intensity. There are two ways to collect the emitted fluorescence light in Kretschmann configuration. Collecting the light from the prism-side is called surface plasmon coupled emission (SPCE) [101, 102] and is illustrated in

Figure 1.15 (a). Spherical prisms can be used for this purpose. The light transmitted through the prism is highly directional and shows a sharp conical profile. The polar angle θ of this cone is slightly lower than the excitation angle, as the wavelength of the emitted fluorescence light is higher than the excitation wavelength. Special setups have been designed to fully collect the emitted fluorescence light cone such as a paraboloid mirror [69, 103] or additional grating elements [104].

The second method to collect fluorescence light in Kretschmann configuration is called surface plasmon fluorescence spectroscopy (SPFS) [105] and is shown in Figure 1.15 (b). In this configuration the light is collected from the opposite side of the prism, where no sharp fluorescence emission peak occurs.

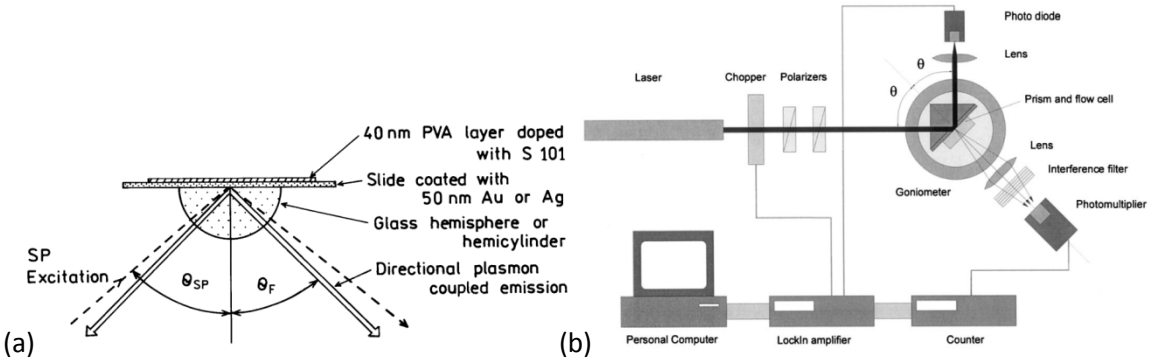

Figure 1.15 (a) SPCE setup (graphic from [101]) and (b) SPFS setup (graphic from [105]). Reprinted figure (a) with permission from I. Gryczynski et al., Journal of Physical Chemistry B, vol 108, pp. 12568-12574, 2004, http://dx.doi.org/10.1021/jp040221h . Copyright (2004) by the American Chemical Society. Reprinted figure (b) with permission from T. Liebermann et al., Colloids and Surfaces A-Physiochemical and Engineering Aspects, vol. 169, pp. 337-350, 2000, http://dx.doi.org/10.1016/S0927-7757(00)00449-0 .

A 55 nm Ag film modified with fluorophore rhodamine-6G dye ($\eta_0 = 0.95,\ \lambda_{ab} = 530\ nm,\ \lambda_{em} = 550\ nm$) was excited with a 543 nm laser at resonance and showed EF=32 at fluorescence emission peak (in SPCE configuration) compared to a plane glass substrate. Fluorescence enhancements in the same range are achieved for a gold film in Kretschmann configuration with SPFS and a Cy5 dye ($\eta_0 = 0.28, \lambda_{ab} = 640\ nm,\ \lambda_{em} = 670\ nm$) at excitation wavelength 633 nm [72].

As already mentioned LRSPPs can exhibit much higher electric field intensity enhancement and therefore fluorescence enhancement is two to three times higher for AlexaFluor 647 ($\eta_0 = 0.33$, $\lambda_{ab} = 650\ nm,\ \lambda_{em} = 665\ nm$) and Cy5, compared to regular SPP fluorescence enhancement [106, 107]. The fluorescence emission from a structure supporting LRSPP shows in addition sharper fluorescence emission peaks than normal SPPs [108].

1.7.2.2 Noble metal grating surfaces

Noble metal gratings provide alternative versatile means for exciting SPPs on metal surfaces. They show electric field intensity enhancements in the same range of SPPs excited in Kretschmann configuration on flat metal surfaces. The emitted fluorescence light of a fluorophore attached to a grating is highly directional [109, 110] and the emission angle can be efficiently controlled by the grating period Λ. As it has been seen in section 1.3 the lifetime of an excited state in a fluorophore correlates with the change in quantum efficiency. It has been shown for a 1D sinusoidal silver grating (silver thickness 200nm) with period $\Lambda = 415\ nm$, that the lifetimes of excited states are similar for flat silver and grating when the grating amplitudeA_0 is small (around $A_0 = 20\ nm$), while they differ significantly when the amplitude is getting bigger (above $A_0 = 40\ nm$) [30]. These findings indicate that the change of intrinsic quantum efficiency is dependent on the grating shape.

A 1D silver groove grating showed EF=40, while for a 2D silver hole array the enhancement was EF=100 for Cy5 dye. The enhancement values are given for a plain glass reference, while compared to flat silver it is less by more than a half [34]. In a study where a thin silver grating has been excited from the substrate side showed fluorescence intensity enhancements of EF=100 for a Cy5 molecule [111].

The enhancement of the fluorophore rhodamine-6G on a sinusoidal silver grating (with silver thickness 50 nm) was reported to be above EF=30 compared to the grating structure without metal on top [28].

A nanohole in a gold film that is surrounded by a circular grating with a certain number of grooves is called “bulls eye”. The collected fluorescence signal of Alexa Fluor 647 dyes diffusing into the nanohole is highly enhanced by a factor of EF=120 [37]. The enhancement is due to a moderate electric field intensity enhancement at λ_{ab} and a highly directional emission of fluorescence light at λ_{em}.

1.7.2.3 Rough metallic surfaces and island films

Rough metallic surfaces and island films show moderate field intensity enhancements and can increase the intrinsic quantum efficiency of a dye, similar to nanoparticles. Random structures don’t show a high directivity of emitted fluorescence and emission is rather isotropic.

A gold nano-island film covered with an amorphous silicon-carbon alloy showed an enhancement of EF=35 compared to flat glass for a Cy5 dye [112]. The nano-island film was prepared by depositing a thin layer of metal on a substrate, followed by a high temperature annealing process, which resulted in the formation of nano-islands.

A rough silver surface have been shown to enhance the fluorescence signal of rhodamine-6G by a factor of EF=30 compared to flat glass and by a factor of EF=15 compared to flat silver in a broad wavelength range from $\lambda = 600\ nm$ to $\lambda = 700\ nm$ [113].

For a silver island film, enhancements of EF=10-15 are reported for a sandwich immunoassay and an Alexa Fluor 647 dye compared to a flat glass substrate [114].

1.7.2.4 Nanoparticles and random nanoparticle assemblies

In the current section, structures for plasmon-enhanced fluorescence are presented in which the nanoparticles have been prepared by chemical synthesis. The structures can show medium to high electric field intensity enhancements and can strongly influence the quantum efficiency of a fluorophore. Due to the random orientation and position of the nanoparticles to each other they do not show high directivity of emitted fluorescence light.

The fluorescence signal of NileBlue-dye ($\eta_0 = 0.27,\ \lambda_{ab}$~$627\ nm,\ \lambda_{em}$~$630\ nm$) close to a $D = 80\ nm$ gold sphere attached to a glass tip was EF=8-9 for excitation wavelength of $\lambda = 637\ nm$ [38]. A silver sphere with same size, likewise attached to a glass tip showed enhancements of EF=13-15 for Alexa Fluor 488 ($\eta_0 = 0.92,\ \lambda_{ab}$~$495\ nm,\ \lambda_{em}$~$519\ nm$) at excitation wavelength $\lambda = 488\ nm$ [38]. The distance between nanoparticle and fluorophore was in both cases varied and values are given for the distance, where the highest enhancement is observed.

Aggregated silver spheres with average diameter of $D = 34\ nm$ have been shown to increase the fluorescence of the fluorophore Atto-655 ($\eta_0 = 0.3,\ \lambda_{ab}$~$663\ nm,\ \lambda_{em}$~$684\ nm$) compared to a fluorophore in free solution by EF=170 [47]. The high enhancement can be attributed to the high gap mode density between the silver spheres and thus the high electric field intensity enhancements. In addition, fluorophore lifetime measurements have shown, that the lifetime in the excited state is reduced by a factor of 300 compared to free dyes [47].

For a gold nanorod, where the resonances of the longitudinal and transversal modes were matched to the excitation wavelength of the laser and the peak emission wavelength of an Oxazine-725 fluorophore, high fluorescence intensity enhancements of EF=20.8 compared to dye in solution have been reported [49].

Very high enhancements of EF=1000 have been shown for a perylene diimide fluorophore in a 2-3 nm gap between a $D = 80\ nm$ silver sphere and a flat silver surface. The enhancement is compared to a flat silver surface without additional silver sphere [115]. The high enhancement factor EF can be attributed to the high electric field intensity in the gap, but also to the choice of the reference structure. Fluorophores on flat metal surfaces are highly quenched for such small distances between metal and fluorophore (see Figure 1.9).

1.7.2.5 Ordered metallic nanostructures

The fluorescence signal of an individual TPQDI fluorophore ($\eta_0 = 0.025$, λ_{ab}~$790\,nm$, $\lambda_{em} = 850\,nm$) with a very low intrinsic quantum efficiency $\eta_0 = 0.025$ has been enhanced by a factor of EF=1340 when attached in the gap of a gold bowtie antenna (two triangular nanoparticles with a gap between the triangle tips) [44]. The high enhancements are attributed to the high electric field intensity enhancement of $|E|^2/|E_0|^2 \approx 181$ and an increase of quantum efficiency by $\eta/\eta_0 = 9.3$, while directivity of emitted fluorescence light is not significantly changed [44]. For higher quantum efficiency dyes at around $\eta > 0.25$ no quantum efficiency enhancement would have been observed and the fluorescence enhancement would have been solely due to electric field intensity enhancement [44]. Let us note that the high single fluorescence enhancements are only achieved in the gap of the bowtie antenna, while in other regions no significant enhancement is achieved.
A similar enhancement of EF=1100 is observed for an individual Alexa Fluor 647 fluorophore with additional quencher ($\eta_0 = 0.08$) diffusing into a gap between two half sphere gold particles (diameter $D = 76\,nm$) [81].

A structure that provides high directivity of the emitted fluorescence light is the so called Yagi-Uda antenna which consists of 5 nanorods of different sizes. The emitted light of a quantum dot placed in proximity of such an antenna can emit fluorescence light 6.4 times more directional [53, 55].

A dense silver disk array (disk diameter $D = 120\,nm$, period $\Lambda = 200\,nm$) on substrate showed a localized surface plasmon resonance at $\lambda = 550\,nm$. Fluorescence enhancement of a moderate EF=15 for Cy3 ($\eta_0 = 0.04$, $\lambda_{ab} = 550\,nm$, $\lambda_{em} = 570\,nm$) labeled DNA was achieved [116].

Similar system of gold disk arrays (disk diameter $D = 100\,nm$, period $\Lambda = 200\,nm$), showed fluorescence enhancement of EF=14 for a CdSe-ZnS quantum dot attached to the gold disks by a molecular linker at distance $f = 16\,nm$ [117].

Dense gold nanodisk arrays (disk diameter $D = 135\,nm$, period $\Lambda = 200\,nm$) with each disk sitting on a SiO_2 pillar closely above a flat-gold film with additional small gold clusters in the gap and in addition covered with 5 nm SiO_2 showed high fluorescence enhancements of EF=2970 for ICG fluorophore ($\eta_0 = 0.012$, $\lambda_{ab} = 783\,nm$, λ_{em}~$850\,nm$) and EF=600 for IR800 fluorophore ($\eta_0 = 0.07$) [118]. The reference structure was flat glass substrate. The high enhancements are attributed to high electric field enhancement in the gap region and an increase in quantum efficiency.

Silver nanotriangle arrays produced by colloidal lithography showed a fluorescence enhancement of EF=83 for Alexa Fluor 790 ($\eta_0 = 0.04$, $\lambda_{ab} = 782\,nm$, $\lambda_{em} = 804\,nm$) compared

to flat glass substrate [83]. In the study it was shown that the enhancement factor EF is equally contributed by the electric field enhancement and an increase of intrinsic quantum efficiency.

Plasmonic structure	*EF*	Fluorophore (η_0)	*D*	Ref.
Continuous metallic films:				
Ag, ATR-coupled SPP	32	Rhodamine-6G (0.95)	High	[119]
Au, ATR-coupled SPP	17	MR 21		[120]
Ag, 2D grating-coupled SPP	100	Cy5 (0.28)	High	[34]
Au, 1D grating-coupled SPP	13	CdSe-ZnS QD (0.45)	High	[31]
Au, 1D grating-coupled SPP	24	Cy5 (0.28)	High	[121]
Au bulls eye, hybrid SPP & LSP	77	AF 647 (0.3)	High	[37]
Ag, 1D grating SPP	30	Rhodamine-6G (0.95)	High	[28]
Ag, 1D grating SPP	100	Cy5 (0.28)	High	[111]
Nanoclusters:				
Ag/Au, 2D nanoclusters, LSP	9.4	Cy5 (0.28)		[122]
Ag/Au, 2D nanoclusters, LSP	35	Cy5 (0.28)		[112]
Ag, rough nanopourous film, LSP	30	Rhodamine-6G (0.95)		[113]
Ag, island film, LSP	50	Bis benzimidazo perylene		[123]
Chemically synthesized nanoparticles:				
Au core dielectric shell, LSP	40	IR800 (0.07)		[124]
Ag spherical NP, LSP	13-15	AF488 (0.92)		[38]
Au spherical NP, LSP	8-10	Nile Blue (0.8)		[125]
Ag spherical NP aggregated, LSP	170	Atto 655 (0.13)		[47]
Ag spherical NP on Ag film, SPP coupled with LSP	1000	Perylene diimide	High	[115]
Au nanorod, LSP	20.8	Oxazine-725		[49]
Ag spherical hollow NP, LSP	300	Cy5 (0.28)		[126]
Ag core dielectric shell, LSP	94	Octadecyl Rhodamine B (R18)		[127]
Lithography fabricated nanoparticles:				
Bow tie NP, LSP	1340	TPQDI (0.025)		[44]
Au gap-antenna, LSP	1100	Alexa Fluor 647 with quencher (0.08)		[81]
Au D2PA, LSP	2970	ICG (0.012)		[118]
Ag nanodisks, LSP	15	Cy3 (0.04)		[116]
Au nanodisks, LSP	15	CdSe–ZnS QDs (0.3-0.5)		[117]
Au nanoholes, hybrid SPP & LSP	82	Oxazine 720 (0.6)		[128]
Ag nanoholes, hybrid SPP & LSP	110	Cy5 (0.28)		[129]
Au nanodisk over metal film, LSP	600	IR800 (0.07)		[118]
Au nanotriangle, LSP	83	Alexa Fluor 790 (0.04)		[83]

Table 1.2 Comparison of different structures for plasmon-enhanced fluorescence. Data of single molecule fluorescence detection is marked with red numbers (table from [46]).

A silver nanohole array with period $\Lambda = 400\ nm$, hole diameter $D = 260\ nm$ and hole depth 25 nm showed enhancements of EF=100 compared to flat glass for a Cy5 dye. The thickness of the silver was 200 nm and the array was additionally coated with 20 nm SiO_2 [34]. The angle of the

incident laser beam (632.8 nm) was adjusted to be in resonance with the SPP resonance and the fluorescence light was collected at the maximum emission angle. The fluorescence enhancement is attributed to the electric field intensity enhancement and the increased directivity by the nanohole grating.

Similar results with fluorescence enhancement of EF=82 are reported for a hole array in a 100 nm thick gold film with a polystyrene film doped with oxazine 720 dyes ($\eta_0 = 0.6,\ \lambda_{ab} = 620\,nm,\ \lambda_{em} = 650\,nm$) on top. The holes were milled into the gold by focused ion beam with a period of $\Lambda = 553\,nm$ and diameter of $D = 100\,nm$. The given enhancement is for a glass substrate as reference [128].

1.7.2.6 Summary

Various structures have been reviewed for plasmon-enhanced fluorescence including flat and corrugated noble metal surfaces, rough surface, chemically synthesized particles and ordered metallic nanostructure produced by lithography. Enhancements have been distinguished between single molecule detection, where the fluorescence signal of a fluorophore within a hot spot was detected and surface averaged fluorescence enhancement with the fluorescence signal of a fluorophore ensemble attached at random points on the surface were detected. Highest fluorescence enhancement of EF=1340 [44] have been reported for single fluorescent molecules attached to the gap of a bow tie antenna. Nevertheless these high enhancements are due to the low intrinsic quantum efficiency of the used dye and the high electric field intensity in the gap region of the bow tie antenna. Nanocluster are easy to prepare structures and give moderate enhancements. Assemblies of chemical synthesized particles can profit from a high gap density and can lead to fluorescence enhancements of EF=170 [47].

Highest enhancements for the frequently used fluorophore Cy5 (η_0=0.28), that has a medium quantum efficiency, are achieved for a 2D silver nanohole grating [34] and a 1D silver groove grating [111]. Both showed enhancements of EF=100 compared to a flat glass substrate.

2 Research goals

This thesis aims at the design, preparation, characterization and implementation of metallic nanostructures for plasmon-enhanced fluorescence. Plasmonic biosensors can significantly enhance the fluorescence signal of a fluorophore in proximity to a metallic surface and therefore increase the sensitivity. In particular the structures are designed to operate in epifluorescence geometry in which the fluorophore labels are exited and emitted light is collected in the direction perpendicular to the surface (see Figure 2.1). A widely used method for the fluorescence based analyte detection is an immunoassay in which an analyte is immobilized by a capture antibody and the binding is detected by a detection antibody (see Figure 2.1).

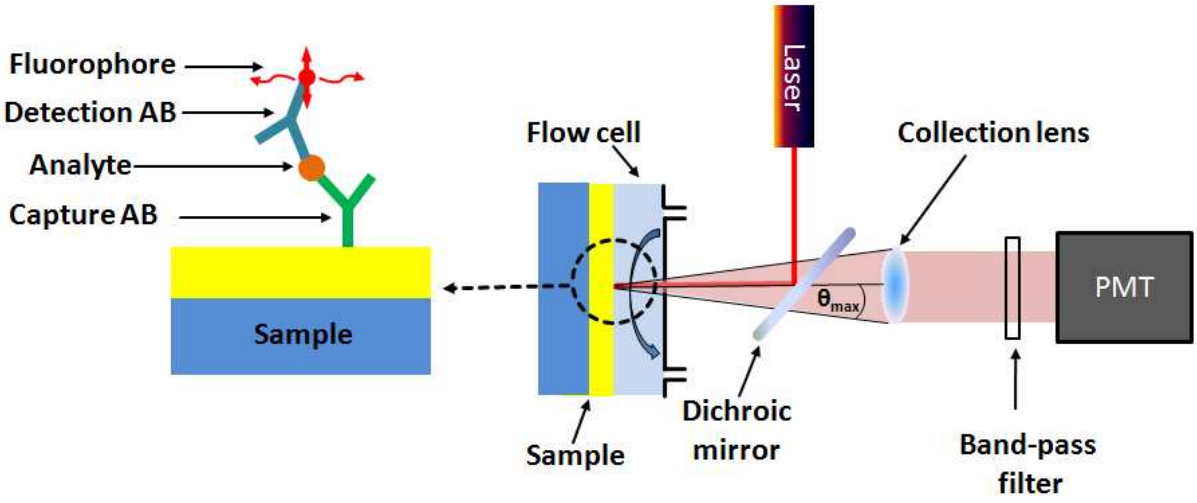

Figure 2.1 Schematic of epifluorescence geometry. The inset shows an analyte immobilized to the sample surface by a sandwich immunoassay.

The thesis covers the following areas in order to realize efficient structures for plasmon-enhanced fluorescence.

a) Two types of structures for fluorescence enhancement in immunoassay-based detection will be proposed. Firstly, a corrugated gold surface supporting surface plasmon polaritons (SPPs) (section 4). This approach takes advantage of the electromagnetic field intensity confined at the metal surface. Secondly, arrays of metallic nanoparticles supporting collective localized surface plasmons (cLSPs) which benefit from diffractive coupling and high field confinement around the nanoparticle surface (section 5). Both SPP and cLSP structure will be designed in order to efficiently excite fluorophores and for efficient out-coupling of fluorescence light by surface plasmon modes to far-field radiation perpendicular to the surface.

b) Establishing a model that fully describes the near-field interaction between a fluorophore and metallic nanostructures. The model needs to take into account the modified surface plasmon-driven excitation at the fluorophore absorption wavelength λ_{ab}, the out-coupling of fluorescence light via plasmon modes at the emission wavelength λ_{em} and the change of intrinsic quantum yield. In addition, the model has to address the coupling of surface plasmon modes to the far-field. Finite-difference time-domain (FDTD) method will be used in order to predict the overall fluorescence intensity enhancement for fluorophores placed in vicinity to investigated metallic nanostructures. The simulations will help to decompose the enhancement factor to key contributions due to a) enhanced excitation strength, b) directional fluorescence emission, and c) increased quantum yield. The results can be found in sections 4.3 and 5.3.

c) Development of protocols for the preparation of large areas of periodic metallic structures with characteristic sizes as small as 100 nm and periods of several hundreds of nm. Laser interference lithography and nanoimprint lithography represent suitable tools for the preparation of the targeted structures. The protocols together with characterization of the morphology by atomic force microscopy and scanning electron microscopy can be found in sections 4.4 and 5.4.

d) Experimental verification of simulated results will be carried out by homebuilt optical systems that allow measurement of the spectrum of surface plasmon modes and angular distribution of emitted fluorescence light. Respective results are presented in sections 4.4 and 5.4.2.

e) A sandwich immunoassay will be established on the surface of the prepared plasmonic nanostructures for specific capture of a target analyte from liquid sample. An optical system that allows for measurements compatible with epifluorescence microscopes and microarray fluorescence scanners will be developed. The fluorescence signal of the plasmonic nanostructure will be compared to conventional substrates in order to determine an enhancement factor and evaluate the performance. The assay readout will be done in a flow-cell in order to measure kinetics of fluorescence signal, associated with association and dissociation phase of molecular affinity interaction, seen in section 4.5.

3 Methods

This chapter comprises the computational and experimental methods used in this thesis. It starts with the finite-difference time-domain (FDTD) method as a strong numerical tool to predict the interaction of light with nanostructures. This computational method was used to design efficient structures for plasmon-enhanced fluorescence, as well as to understand measurement results. The next section concerns the nanostructure fabrication methods. Followed by a section introducing a setup for the measurement of angle and wavelength dependent reflectivity.

3.1 FDTD simulations

FDTD method is a strong numerical tool for simulations of the interaction of various structures with electromagnetic waves. It can predict the near-field close to a structure as well as far-field properties such as reflectivity and transmission. The following chapter gives an introduction to the method and the various quantities that can be derived from it. The FDTD method is implemented in various commercial and open source software solutions. The software used to produce the results in this thesis are MEEP [130] as an open source software and the commercial available software Lumerical FDTD Solution.

3.1.1 Basic concept of FDTD

This thesis focuses on the interaction of plasmonic nanostructures with light. As light is an electromagnetic wave, the interaction can be described by Maxwell equations. Finite-difference time-domain [131] is a fundamental numerical method to solve Maxwell equations. The electric field vector $\vec{E}$ and the magnetic field $\vec{H}$ are calculated on a discrete rectangular grid for discrete time steps. Thus every structure one is interested in is meshed in 3D first. The result of FDTD simulations are the time dependent field components on every grid point. Compared to other numerical methods such as finite element method (FEM), which is a time independent approach to solve Maxwell equations, it is possible to simulate a wide range of frequencies (wavelength) in one simulation run. This is possible, because one can perform a Fourier transformation in time after the simulation and get by this the frequency information at every grid point. The basic numerical concept of FDTD is explained as follows. Faraday's and Ampere's law for isotropic and linear media are given as [131]:

$$\frac{\partial \vec{H}}{\partial t} = -\frac{1}{\mu}\nabla \times \vec{E} - \frac{1}{\mu}\left(M + \sigma^* \vec{H}\right) \tag{3.1}$$

and

$$\frac{\partial \vec{E}}{\partial t} = \frac{1}{\varepsilon}\nabla \times \vec{H} - \frac{1}{\varepsilon}\left(J + \sigma \vec{E}\right) \tag{3.2}$$

with μ magnetic permeability, ε electrical permittivity, M magnetic current density, J electric current density, σ electric conductivity and σ^* magnetic loss. As the magnetic and electric fields are vectors, Eq. (3.1) and Eq. (3.2) are actually 6 equations in total. The equations can be solved numerically by using the Yee algorithm, where electric and magnetic field components are solved on a rectangular grid over time. The so called Yee cell is shown in Figure 3.1. The finite mesh size of the grid is Δx, Δy and Δz while the time is discretized by Δt. The grid position can be given by the integers i, j, k and the number of the time Δt step by the integer n.

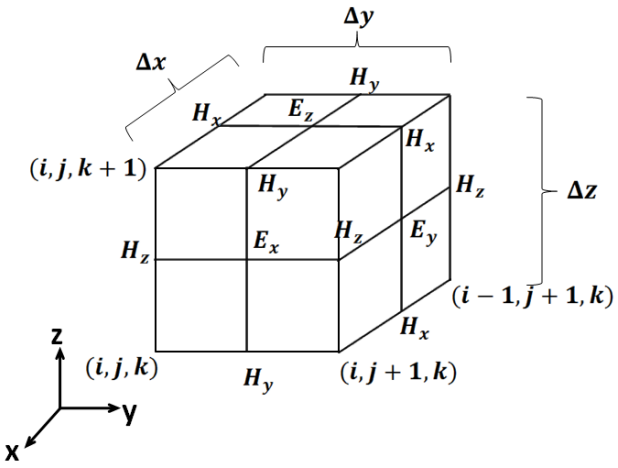

Figure 3.1 Yee cell (graphic adapted from [131]).

The magnetic and electric field components are sequentially calculated. The magnetic field components are calculated at full time steps $n \cdot \Delta t$, while the electric field components are calculated at half time steps $(n + 1/2) \cdot \Delta t$. Exemplary for the work mechanism of the Yee algorithm the calculation of the E_x component will be described. The electric field component E_x at grid point $(i, j + 1/2, k + 1/2)$ at a certain time $t = (n + 1/2) \cdot \Delta t$ can be calculated by the knowledge of the electric field E_x at the same grid position but previous time step $t = (n - 1/2) \cdot \Delta t$ and by the knowledge of the magnetic field components $H_{y(i,j+1/2,k+1)}$, $H_{y(i,j+1/2,k)}$, $H_{z(i,j+1,k+1/2)}$ and $H_{z(i,j,k+1/2)}$, surrounding E_x at the time $t = n \cdot \Delta t$. Therefore for determining a field component at a new time step, the previous field components are needed. The magnetic field components can be

calculated in a similar way from the magnetic field component at same grid point of the previous time step and by the knowledge of the electric field components surrounding it, at a half time step before.

The explicit equations for determining the electric and magnetic field components are rather complex and given in the book “Computational Electrodynamics: The Finite-Difference Time-Domain Method” [131].

3.1.2 Boundary conditions

In a usual experiment (e.g. a reflectivity measurement) the nanostructure is irradiated by a light source several centimeters away. It is not possible to include the whole nanostructure and light source in a FDTD simulation, as the grid size of the simulation has to be chosen in the sub wavelength range of the incident light. This would result in an extremely huge simulation, which would exceed the capacity of today’s PCs. Therefore to truncate the simulation region, boundary conditions are needed. In Figure 3.2 a gold grating on a substrate is shown. For the rest of this chapter this example will be discussed, nevertheless the statements which are made in the FDTD section are valid for all periodic structure. For reasons of simplicity all figures and equations in this FDTD chapter are shown in 2D, but can be simply expanded to 3D.

In a typical FDTD-simulation a short pulse of a Gaussian wave packet is emitted by a source at a certain position into the simulation region (see Figure 3.2). The light of the wave packet interacts with the structure and is then absorbed, scattered or transmitted. Depending on the structure under study the light stays for different duration in the structure. As FDTD is a time dependent method one has to wait until the fields in the structure decay before analyzing the simulation results. For example for the simulation of SPPs the light travels over several micrometers on the interface between a noble metal and a dielectric before it gets completely absorbed. In Figure 3.2 two commonly used boundary conditions are shown.

Perfectly matched layers (PMLs) are applied in the minus z and plus z-directions. PMLs can be seen as perfect absorbing layers, designed to be without reflections for light at any angle and wavelength [132]. Let us note that the efficiency of PMLs decreases when light at steep angles is incident on them. In Figure 3.2 a plane wave source irradiates the grating and the light reflected from the grating is absorbed in the PML. Therefore the PMLs act like a virtual extension of the region of the air and it seems the light propagates further into the air. The same is true for the PML at minus z positions where the PML absorbs the transmitted light through the grating and therefore it seems that the glass continues to infinity. By use of the PMLs, the simulation was truncated in the z-direction.

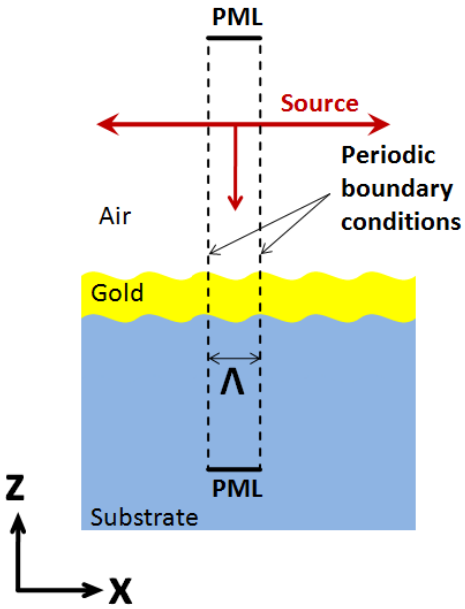

Figure 3.2 Schematic of gold grating with periodic boundary conditions and perfectly matched layers (PMLs).

In the x-direction the grating can be truncated by periodic boundary conditions. A periodic structure can be fully described by one unit cell, which continues with a period Λ. In periodic boundary conditions it is assumed, that the electric field at the one side of a unit cell is equal to the electric field on the other side:

$$\vec{E}(x) = \vec{E}(x + \Lambda). \tag{3.3}$$

While this is true for normal incident light, for incident light under a certain angle θ_i the boundaries are described by Bloch boundary conditions:

$$\vec{E}(x) = \vec{E}(x + \Lambda) \cdot e^{ik_x \Lambda}, \tag{3.4}$$

where $k_x = k_0 \sin\theta_i$ is the wave vector of the incident plane wave in x-direction. Eq. (3.4) includes an additional phase shift $e^{ik_x \Lambda}$, which compensates for the incident angle θ_i.

In a configuration like shown in Figure 3.2 it is also possible to achieve a spatial distribution of electric or magnetic fields (so called near-field maps) of the structure, by collecting all field values in the desired region.

3.1.3 Transmission/Reflectivity

The most important far-field properties, which can be directly measured are transmission and reflectivity. In the following, it is shown how the transmission and reflectivity spectra are calculated in a simulation. The power transported by an electromagnetic wave is described by the Poynting vector $\vec{P}$:

$$\vec{P} = \vec{E} \times \vec{H} \tag{3.5}$$

with the unit $[Wm^{-2}]$. The direction of the Pointing vector gives the direction of the energy transport. In Figure 3.3 two detectors are shown, a reflectivity detector and a transmission detector.

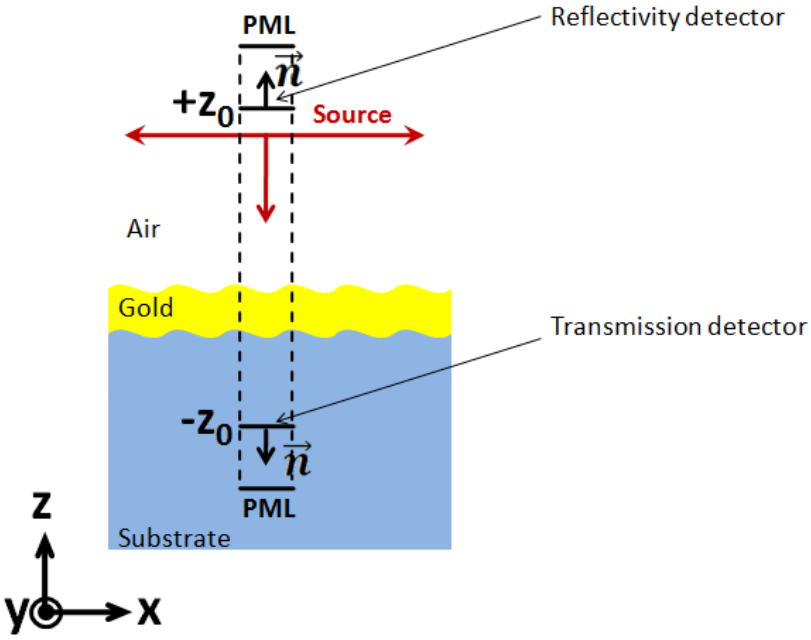

Figure 3.3 Schematic for simulation of transmission and reflectivity spectra.

Both detectors have a surface normal vector $\vec{n}$. In the detector planes the electric field values $\vec{E}(x, \pm z_0)$ and magnetic field values $\vec{H}(x, \pm z_0)$ are collected at every grid point. The reflectivity R is calculated as:

$$R = \int_{x_0}^{x_0+\Lambda} \vec{P}(x, +z_0) \cdot \vec{n} dx \tag{3.6}$$

and analogues for the transmission when changing $+z_0$ to $-z_0$. For reflectivity or transmission simulations on periodic structures such as gratings, additional statements need to be made to

simulate reasonable data. The simulated reflectivity or transmission values considered so far include all the light that passes the detector independent of the direction of the scattered light. In an experiment, however, the reflectivity spectra is measured under a certain angle θ, e.g. at the negative angle of the incident light $\theta = -\theta_i$. Measuring in this configuration only allows to detect the $m = 0$ diffraction order. The diffraction at a 1D grating can be described by the grating equation [133]:

$$m\frac{\lambda_0}{n_d} = \Lambda(\sin\theta_m + \sin\theta_i) \tag{3.7}$$

with m the diffraction order, λ_0 the vacuum wavelength, n_d the refractive index of the surrounding medium, Λ the grating period, θ_m the angle of the diffracted light at the m-th diffraction order and $\theta_i$the angle of the incident light. The different diffraction orders of a grating are sketched in Figure 3.4. A diffraction order vanishes when θ_m becomes equal or bigger than 90 deg. For normal incident light $\theta_i = 0\ deg$ the vanishing of the first diffraction order $m = 1$ occurs therefore at:

$$\lambda = n_d \cdot \Lambda \tag{3.8}$$

Above this wavelength no higher diffraction orders exist.

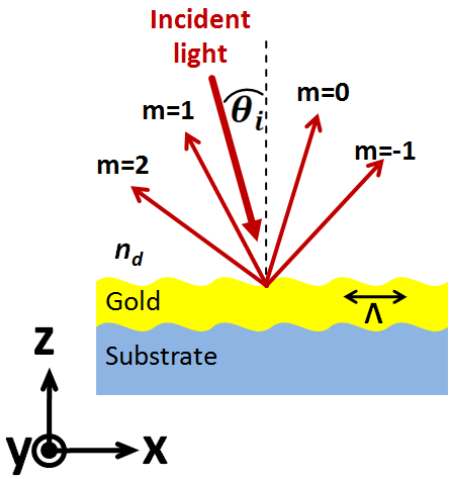

Figure 3.4 Schematic of diffracted beams with different diffraction orders m.

To overcome the additional part of higher order diffraction in simulated reflectivity or transmission spectra one has to perform a near-field to far-field transformation in the detector plane and see under which angle in the far-field light is reflected or transmitted. By this, one can distinguish between the different diffraction orders.

3.1.4 Quantum efficiency

While the reflectivity, transmission and spatial distribution of fields are calculated for a plane wave incident on a structure, the situation is quite different for the interaction of fluorophore with a structure. The first difficulty is, how to introduce a quantum mechanical object as a fluorophore into classical electromagnetism simulations. Fortunately it can be shown, that a fluorophore can be treated as an electric dipole which is a purely classical object [44, 134]. The simulation setup for determining the modified quantum efficiency is shown in Figure 3.5. The dipole (fluorophore) is shown with a red double arrow.

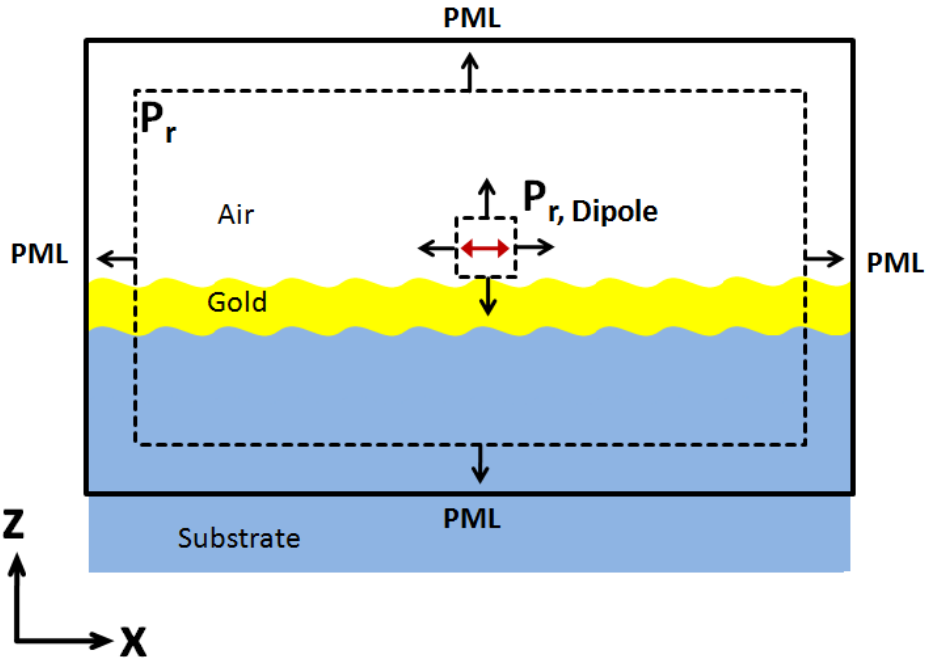

Figure 3.5 Sketch of simulation setup for determining the modified quantum efficiency. Boxes for calculation of P_r and $P_{r,Dipole}$ are shown by black dotted lines. Dipole indicated by red double arrow.

As can be seen, no periodic boundary conditions are used. If one would use periodic boundary conditions, it would mean, that in every unit cell is a dipole. The dipoles would all oscillate coherently and this would not correspond to the situation in experiment, where dipoles are excited at different times, emit at different times and have no fixed phase correlation. Therefore one has to simulate one dipole close to several periods of the nanostructure [135]. The number of periods has to be big enough to allow the fields of the involved modes to decay to a certain amount. For this, it is necessary to choose the number of periods in a way, that the simulation region is several times bigger than the propagation length of the involved modes. The computational volume is surrounded by PMLs and no periodic boundaries are used.

It has been shown in section 1.3, that the change of the intrinsic quantum efficiency can be described by [38, 44, 45]:

$$\eta = \frac{\gamma_r \,/\, \gamma_r^0}{\gamma_r/\gamma_r^0 + \gamma_{abs}/\gamma_r^0 + \,(1-\eta^0)\,/\,\eta^0} \tag{3.9}$$

The ratios of the decay rates $\gamma_r \,/\, \gamma_r^0$ and $\gamma_{abs} \,/\, \gamma_r^0$ can be obtained by $\gamma_r/\gamma_r^0 = P_r \,/\, P_r^0$ and $\gamma_{abs}/\gamma_r^0 = P_{abs} \,/\, P_r^0$ [44, 134], with P_r^0 power radiated by a dipole in the absence of a nanoantenna, P_r power radiated in the presence of a nanostructure and P_{abs} the power which is absorbed in the metallic nanostructure and thus not radiated to the far-field. The absorbed power can be calculated by $P_{abs} = P_{r,Dipole} - P_r$, where $P_{r,Dipole}$ is the total power radiated by the dipole in presence of the nanostructure. In Figure 3.5 it is shown how to get access to $P_{r,Dipole}$ and P_r, by black dotted boxes. The power radiated by the dipole $P_{r,Dipole}$ is achieved by surrounding the dipole by a small box with 4 detectors (in 3D, 6 detectors) which detect the Poynting vector and thus the energy flux through this box. The calculation of the power through a surface by a Poynting vector is the same as described in section 3.1.3. It is important that the box is not intersecting with the structure, as then absorption in the metal would be included. The radiated power P_r can be calculated by surrounding the whole structure with detectors, which collect the information of the Poynting vector and thus the energy flux can be calculated. P_r is a measure for all the power that is radiated to the far-field and is not absorbed in the structure (e.g. in the gold). Let us note, that when the structure consists of dielectric materials only (which show no absorption) $P_{r,Dipole} = P_r$. Eq. (3.9) can be rewritten with the above definitions as:

$$\eta = \frac{P_r/P_r^0}{P_{r,Dipole}/P_r^0 + \,(1-\eta^0)\,/\,\eta^0} \tag{3.10}$$

3.1.5 Far-field emission

Another important feature in the metal-fluorophore interaction is the fluorescence emission. First of all it is important to clarify what is a far-field and what is a near-field. The Near-field describes the electric and magnetic field, at distances d within several wavelength λ of the light close to the nanostructure. The far-field describes the fields at far distances d from the structure $d \gg \lambda$. In a typical fluorescence experiment the far-field is detected, while one has no access to the near-field. For practical reasons the intensity radiated to far-field $P(\theta, \varphi)$ is commonly given in spherical coordinates.

The setup for the simulation of far-field emission is almost similar to section 3.1.4 and is shown in Figure 3.6. The only difference is, that instead of detecting the Poynting vector in the box around the structure (dotted line) one collects the electric and magnetic field components.

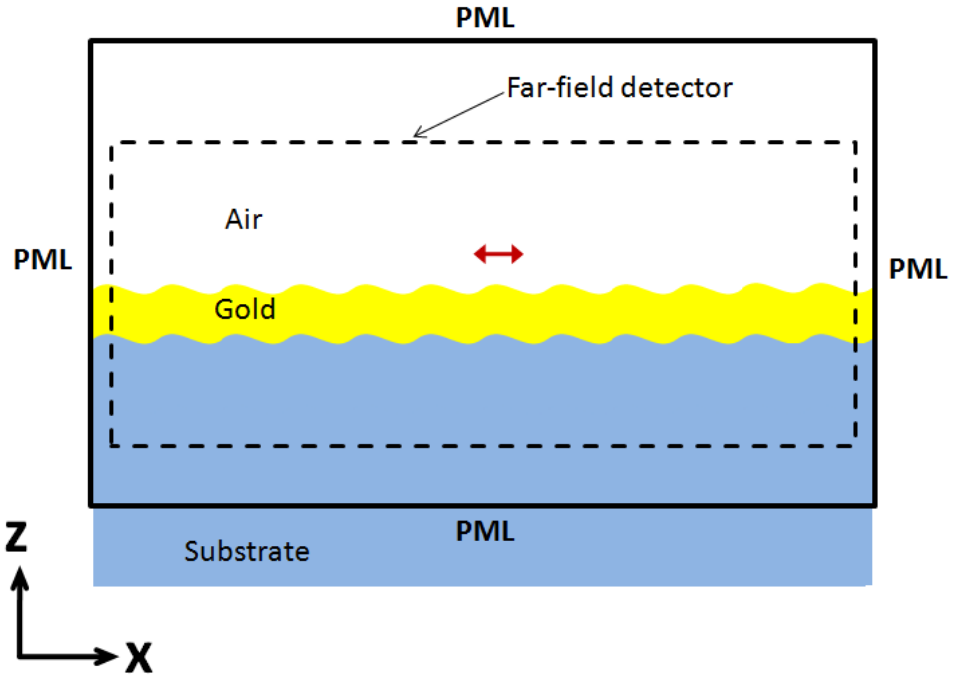

Figure 3.6 Simulation setup for far-field simulation. Dipole indicated by red double arrow.

In the far-field detector shown in Figure 3.6 the near-field components of the electric and magnetic field are collected. By solving complex integrals of the electric and magnetic fields over these surfaces one can achieve by a far-field transformation the intensity $P(\theta, \varphi)$ radiated into certain spherical angels. The equations for this far field transformation are rather complicated, and can be found in "Computational Electrodynamics - The Finite-Difference Time-Domain Method" [131]. A useful approach to quantitatively evaluate the ability of a nanostructure to direct fluorescence light into a certain direction is the collection efficiency CE.

$$CE = \frac{\int_0^{\theta_{max}} \int_0^{2\pi} P(\theta, \varphi) \sin\theta \; d\varphi d\theta}{\int_0^{\pi} \int_0^{2\pi} P(\theta, \varphi) \sin\theta \; d\varphi d\theta} \qquad (3.11)$$

CE shows how much light emitted by a fluorophore within a nanostructure is collected by a potential lens placed over the structure with a maximal acceptance angle of θ_{max}.

3.1.6 Performance calculations

This section introduces a mathematical formalism used in this thesis, in order to compare the ability of fluorescence intensity enhancement of different substrates and nanostructures. There are three quantities influencing the performance of a biosensor system utilizing plasmon-enhanced fluorescence. The excitations rate γ_e, the increase of intrinsic quantum efficiency and the angular distribution of the emitted fluorescence light $P(\theta, \varphi)$ that affects the collection efficiency CE defined in Eq. (3.11). The excitation rate is accessible by the electric near-field enhancement and can be simulated like stated in section3.1.2.

To get a realistic measure of the enhancement, these three features need to be averaged for different fluorophore positions on a nanostructure and different fluorophore orientations. In general, the enhancement factor EF of a structure for plasmon-enhanced fluorescence can be given as:

$$EF = \frac{\langle \gamma_e \cdot \eta \cdot CE \rangle}{\langle \gamma_e^0 \cdot \eta^0 \cdot CE^0 \rangle} \tag{3.12}$$

The superscript 0 denotes the absence of a nanostructure and thus represents the case of a fluorophore in a homogenous environment (e.g. in water). The brackets ⟨ ⟩ denote average over different fluorophore positions and all possible orientations of the absorption dipole $\vec{\mu}_{ab}$ and the emission dipole $\vec{\mu}_{em}$. Eq. (3.12) gives the enhancement of a fluorophore close to a nanostructure compared to a fluorophore in aqueous environment. Before writing the equation for the EF in more detail, we need to distinguish between two different cases of dipole orientation shown in Figure 3.7.

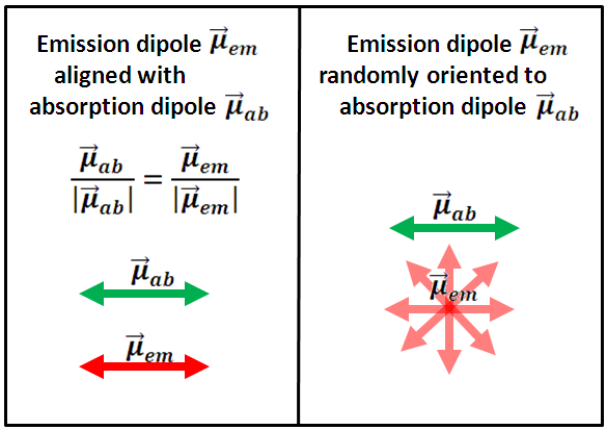

Figure 3.7 Sketch of different dipole orientations of absorption dipole $\vec{\mu}_{ab}$ to emission dipole $\vec{\mu}_{em}$respective to each other.

Firstly, let us assume that the absorption dipole $\vec{\mu}_{ab}$ and the emission dipole $\vec{\mu}_{em}$ point in the same direction. This situation holds when the emitter dipole is not rotating after excitation or the rotation is much slower than the decay rate of the fluorophore. The equation describing this condition is:

$$EF = \frac{\sum_p \sum_k \gamma_{e,pk} \cdot \eta_{pk} \cdot CE_{pk}}{\sum_p \sum_k \gamma^0_{e,pk} \cdot \eta^0_{pk} \cdot CE^0_{pk}} \tag{3.13}$$

The index of summation p is performed over different dipole positions on the nanostructure surface. As the electric field intensity enhancement, change of intrinsic quantum efficiency and the directive emission of fluorescence light can differ very strong for different positions p, it is very important to choose proper, representative positions p to calculate the fluorophore interaction with the structure. The index of summation k is performed over all different orientations of the dipole. It can be shown, that a randomly oriented dipole at certain position p is completely described by the three orthogonal polarization directions (orientations) [136-138], through the superposition principle in linear optics. Therefore at a certain position p, three simulations have to be performed to describe a randomly oriented dipole.

Secondly, let us describe the more general case when the emission dipole $\vec{\mu}_{em}$ has a random orientation with respect to the absorption dipole $\vec{\mu}_{ab}$. This holds true, when the fluorophore rotates between the excitation and emission process. The equation for calculating the enhancement factor then yields:

$$EF = \frac{\sum_p \sum_k \sum_l \gamma_{e,pk} \cdot \eta_{pl} \cdot CE_{pl}}{\sum_p \sum_k \sum_l \gamma^0_{e,pk} \cdot \eta^0_{pl} \cdot CE^0_{pl}} \tag{3.14}$$

where the index p runs over different dipole positions and k and l over different dipole orientations. It can be seen in Eq. (3.14), that the dipole orientation index k for the excitation process $\gamma_{e,pk}$ is a different one than for the quantum efficiency η_{pl} and the collection efficiency CE_{pl}, where the index l is used. This is due to the fact, that these two features are associated with the dipole emission process.

3.2 Nanostructure fabrication methods

Various methods for the preparation of nanostructures became recently available including electron beam lithography (EBL), focused ion beam milling (FIB), colloidal lithography, interference lithography and nanoimprint lithography (NIL). EBL and FIB are highly versatile methods, that are well suited for prototype fabrication with resolution below 10 nm [139, 140]. Nevertheless these techniques are time consuming, require expensive equipment and are limited to the micro to millimeter range in the writing area. Thus they are not suitable for mass production of nanostructures. Contrary to these, nanoimprint lithography [141] and interference lithography are methods that allow for structuring of large areas in a short time. Nanoimprint lithography has been shown to reproduce feature sizes below 10 nm [142].

3.2.1 Interference lithography

Interference lithography takes advantage of the wave-nature of light to produce an interference pattern, when two coherent beams intersect. In the following a configuration called Lloyd's mirror (see Figure 3.8) is described to realize such an interference pattern. A narrow beam of a UV-laser (HeCd laser system, output power 4 mW, model IK 3031 R-C from Kimmon) operating at $\lambda = 325\ nm$ is focused by a 40x microscope objective lens (LMU-40X-NUV, Thorlabs) to a pin hole with diameter $D = 10\ \mu m$. The combination of a microscope objective lens and a pinhole works as a spatial filter to improve the beam homogeneity. At a distance of 1 m away from the pinhole a lens (with f=100 cm) is placed to collimate the divergent beam. The microscope objective lens – pinhole – lens complex works as a beam expander. The beam expander allows for increasing the beam diameter and makes it possible to radiate large areas with high intensity homogeneity. The expanded beam is incident on a sample holder consisting of a rectangular dielectric mirror (RM-50.0-30.00-12.7-UV, CVI Melles Griot) and a space to fix the sample. The dielectric mirror and the sample are arranged perpendicular to each other. The sample holder can be rotated by an angle θ. The intensity interference pattern on the sample originates from the interference of the expanded incident beam on the sample and the fraction of the beam which is reflected by the dielectric mirror.

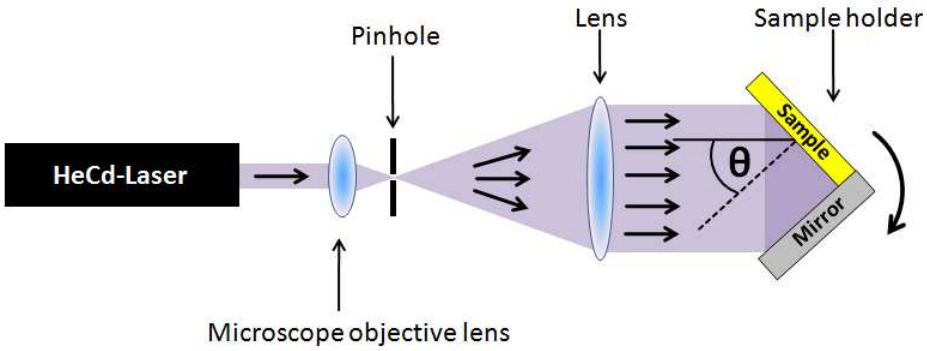

Figure 3.8 Schematic of laser interference lithography setup (Lloyd's mirror configuration).

The interference leads to the occurrence of alternating high and low light intensities on the sample. The sample can be in general, a substrate with several layers and a top layer of UV sensitive resist. The positive resist used in the presented work is Shipley MicropositS1805. In a positive photoresist, the regions which are exposed to a higher dose get dissolved easier in a developer (AZ 303 developer from MicroChemical). Crucial parameters for the aspect ratio of a nanostructure in this setup configuration are the exposition time, laser beam intensity and development time.

As the intensity profile on the sample is crucial for the shape of the developed resist pattern, it is important to know the spatial dependence of the electric field intensity. In the following, the spatial dependence will be derived. In Figure 3.9 the interference of two plane waves is illustrated.

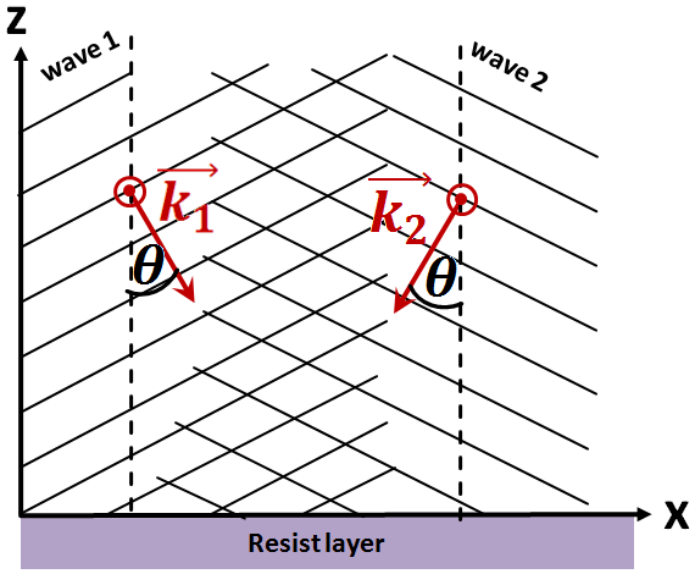

Figure 3.9 Schematic of two interfering plane waves. The directions of the wave vectors $\vec{k_1}$ and $\vec{k_1}$ are shown by red arrows. The polarization of the incident waves is in y-direction.

Let us assume two plane waves with the same amplitude E_0 and polarization in y-direction $\overrightarrow{E_0} = E_0\overrightarrow{e_y}$ and wave vectors $\overrightarrow{k_1}$ and $\overrightarrow{k_2}$ with same magnitude $\left|\overrightarrow{k_1}\right| = \left|\overrightarrow{k_2}\right| = k_0$. The plane waves can be mathematically described by the electric field $\vec{E}$:

wave 1: $\overrightarrow{E_1}(x,z,t) = \overrightarrow{E_0}e^{i(\overrightarrow{k_1}\cdot\vec{r}-\omega t)}$ with $\overrightarrow{k_1} = k_0\begin{pmatrix}\sin\theta\\0\\-\cos\theta\end{pmatrix}$

and

wave 2: $\overrightarrow{E_2}(x,z,t) = \overrightarrow{E_0}e^{i(\overrightarrow{k_2}\cdot\vec{r}-\omega t)}$ with $\overrightarrow{k_2} = k_0\begin{pmatrix}-\sin\theta\\0\\-\cos\theta\end{pmatrix}$

where $\vec{r}$ is the position vector, ω is the angular frequency and t is the time. The summation of the electric fields of wave 1 and wave 2 will give us the total electric field $\vec{E}_{total}$ and therefore the interference pattern of this configuration:

$$\vec{E}_{total}(x,z,t) = \overrightarrow{E_1}(x,z,t) + \overrightarrow{E_2}(x,z,t) \tag{3.15}$$

$$\vec{E}_{total}(x,z,t) = \overrightarrow{E_0}\cdot e^{-i\omega t}\cdot e^{-ik_0\cos(\theta)z}\cdot\left(e^{ik_0\sin(\theta)x} + e^{-ik_0\sin(\theta)x}\right) \tag{3.16}$$

Using the relation $\cos(x) = \frac{1}{2}\left(e^{ix} + e^{-ix}\right)$:

$$\vec{E}_{total}(x,z,t) = \overrightarrow{E_0}\cdot e^{-i\omega t}\cdot e^{-ik_0\cos(\theta)z}\cdot 2\cdot\cos(k_0\cdot\sin(\theta)\cdot x) \tag{3.17}$$

The quantity that defines the contrast in the resist is the intensity, given by $I = \frac{cn\epsilon_0}{2}\left|\vec{E}_{total}\right|^2$ and thus:

$$I(x) = 2cn\epsilon_0 E_0^2\cdot cos^2(k_0\cdot\sin(\theta)\cdot x) \tag{3.18}$$

where n is the refractive index, c the speed of light and ϵ_0 is the vacuum permittivity. This equation can be simplified by the relation $cos^2(x) = \frac{1}{2}\cos(2x) + \frac{1}{2}$ to:

$$I(x) = cn\epsilon_0 E_0^2\cdot[cos(2k_0\cdot\sin(\theta)\cdot x) + 1] \tag{3.19}$$

It can be seen, that the intensity is independent of time and z-component. The intensity is oscillating with the cosine in x-direction. The period of this oscillation can be derived as:

$$\Lambda = \frac{\lambda_{laser}}{2\sin(\theta)} \tag{3.20}$$

where λ_{laser} is the wavelength of the laser.

3.2.2 Nanoimprint lithography

Nanoimprint lithography has gained a lot of attention during the last years, due to the ease of reproducing large areas of an already existing nanostructure. Feature sizes are basically only limited by the sizes of the master from which the structure is replicated. One can distinguish between two kinds of nanoimprint lithography which differ in the way to cure the used imprint resist. The first is thermal NIL where the resist is heat cured. The second is UV-NIL, where the resist is a UV cross linkable photoresist that is cured by UV-light. The process of nanoimprint lithography is sketched in Figure 3.10.

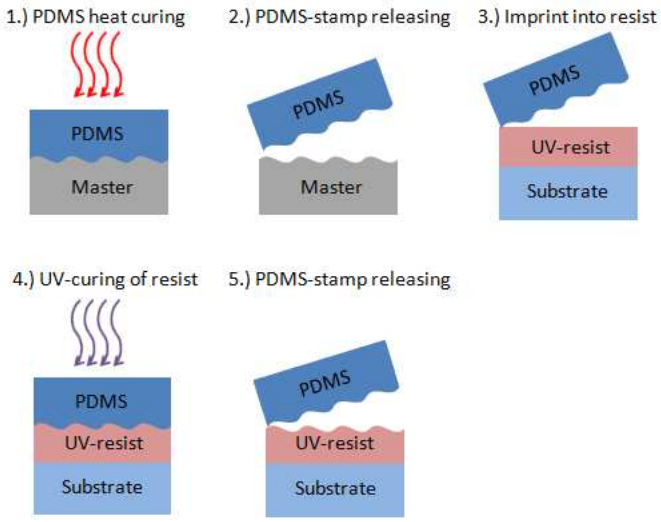

Figure 3.10 Schematic of nanoimprint lithography.

Firstly, liquid PDMS is cast over a master containing the structure that is to be reproduced. The structure on the master can be a patterned resist e.g. from interference lithography or made out of silicon. The PDMS is then heat cured at 60°C overnight or for 3 days at room temperature. After releasing the PDMS from the master it can be used for imprinting into a substrate with spin coated resist on top. The resist used in this work was Amonil MMS10 from AMO GmbH. For the UV-

imprinting, the weight of the stamp itself is enough. The substrate with resist and stamp on top is then put into a UV chamber to crosslink the UV photoresist. Afterwards the PDMS working stamp can be easily removed from the substrate with resist. After releasing the working stamp, further processing steps can follow, e.g. the deposition of a metal film, or additional dry etching steps for a lift-off process.

3.3 Optical characterization

3.3.1 Angular wavelength spectroscopy

The optical reflectivity characterization has been performed by a homebuilt setup shown in Figure 3.11. With the system, a wavelength range of 400 nm to 1000 nm and angles between 0.6 deg and almost 90 deg can be covered. The system consists of a white light source (halogen lamp LSH102 from LOT-Oriel), that is connected to an optical fiber (M25L02 from Thorlabs) and is collimated by an achromatic lens (f=6 mm, 14 KLA 001 from CVI Melles Griot) [143]. The beam diameter of the collimated light is reduced to 1 mm by an aperture and passes then a polarizer. The light is incident on a sample mounted on a two stepper motor system (from Huber GmbH). One motor controls the angle θ of the sample to the incident beam, while the second motor controls the position of the detection optics at angle 2θ. The reflected light from the sample is collected by a lens and coupled to an optical fiber. The fiber is connected to a spectrometer (HR4000 from Ocean Optics). The data acquisition and angle control of the motors is performed by a LabVIEW program [143]. The samples are mounted to a sample holder with a flow-cell clamped on top, with which water is flowed during the measurement.

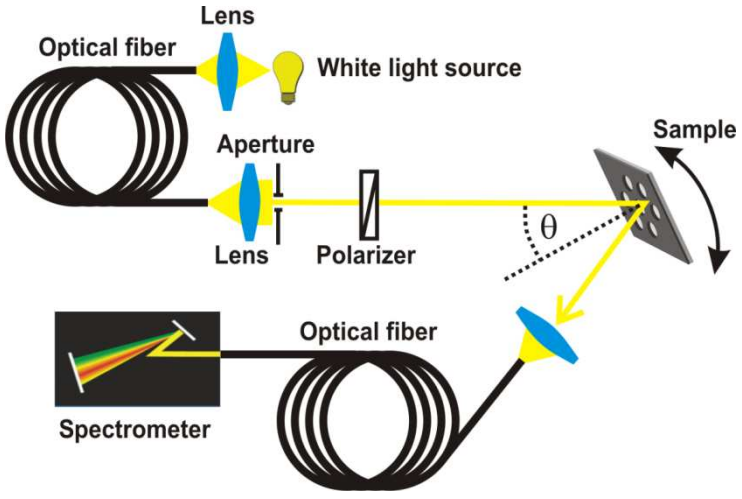

Figure 3.11 Schematic of angular wavelength spectrometer.

A typical measurement is performed in the angle range from 0 deg to 11 deg with angle step size of 0.1 deg. At each angle step the complete wavelength spectra is measured. Recording a reflectivity spectra requires three steps:

1) Background: Measuring the background by blocking the incident light. This background will be subtracted from all following measurements
2) Reference: The white light source has its unique own spectrum. This spectrum would overlap with all measurements which are performed. To compensate for the source spectrum, a reference spectra from a reference spot on the sample need to be measured. In this work, samples are prepared in a way that every sample has a region without nanostructure, the so called reference spot. For example, if the studied structure is a gold grating, a meaningful reference would be a flat gold surface.
3) Sample: The last step is to measure the spectra of the reflected light of the nanostructured region.

The reflectivity spectra normalized to the reference spot is then achieved by the intensities I of the three measurements by:

$$R = \frac{I_{Sample} - I_{Background}}{I_{Reference} - I_{Background}} \qquad (3.21)$$

4 Fluorescence biosensor amplified by crossed diffraction grating-coupled SPPs

4.1 Introduction

This section concerns the amplification of fluorescence signal from fluorophores (that operate in the red part of the spectrum, such as Alexa Fluor 647) on the surface of gold crossed periodically corrugated grating that supports propagating surface plasmon polaritons modes (SPPs) associated with high electric field intensity enhancements. The periodic corrugation of a metallic surface provides an additional momentum (of the grating vector) needed for the excitation of SPPs (see section 1.2.2). Therefore gratings offer an alternative to Kretschmann configuration for SPP excitation, which requires additional optical components. In addition, SPPs on gratings provide an efficient way to out-couple fluorescence light to directional far-field emission and allows for efficient collection of fluorescence light by a detector. The emitted fluorescence light of a fluorophore attached to a grating is highly directional [109, 110] and the emission angle can be efficiently controlled by the grating period Λ. The interaction of fluorophore labels with SPPs at the absorption wavelength λ_{ab} and emission wavelength λ_{em} allows for increased emission rate which enables for the detection of smaller amounts of target molecules and therefore allows for improved limit of detection (LOD) of assays in analytical applications. In general, the fluorescence signal can be mainly amplified by the combination of (locally) increased excitation rate by SPP-enhanced field intensity at λ_{ab} and directional SPP-coupled emission [43, 46, 144].

Previous research in the field of plasmon-enhancement fluorescence utilizing gratings is mainly limited to structures prepared of silver, due to its better plasmonic properties. Nevertheless, the use of silver requires an additional protection layer. In most studies, the grating is irradiated under a certain angle θ_{ex} to match the resonance position of the grating and fluorescence light is collected at the maximum emission angle θ_{em}. This approach needs a two motor system to adjust to the angles θ_{ex} and θ_{em} and thus is rather unpractical for commercial applications. A 1D [111] and 2D [34] silver grating with SiO_2 protection layer showed enhancement factor up to $EF = 10^2$ when compared to flat glass substrate. To our knowledge, no study so far has utilized a 2D gold grating structure for plasmon-enhanced fluorescence.

The presented work describes a complete numerical model that takes into account SPP-driven excitation and emission of fluorophores on the surface of metallic gratings in order to predict the enhancement factor (EF) from randomly oriented fluorophores compared to a reference substrate. Based on the predictions of the simulations, the crossed gratings are fabricated with interference

lithography and replicated by nanoimprint lithography. Finally, the crossed gratings are employed for signal amplification in fluorescence-based immunoassay. In addition, the substrates are designed to assure further compatibility with existing fluorescence readers that rely on epifluorescence geometry. Such devices include various microscopes and fluorescence scanners.

4.2 Investigated geometry

The investigated structure is schematically shown in Figure 4.1. It is composed of a periodically corrugated gold film that is optically thick (thickness of $d_m = 100\,nm$) with an emitter placed at certain distance f perpendicular from gold surface. The height profile $h(x,y)$ of the grating can be described by the following function where Cartesian coordinates x, y, and z are used as defined in Figure 4.1:

$$h(x,y) = h_0 + \alpha\left[\sin\left(\frac{2\pi}{\Lambda}x\right) + \sin\left(\frac{2\pi}{\Lambda}y\right)\right] + \beta\left[\sin\left(\frac{2\pi}{\Lambda}x\right) + \sin\left(\frac{2\pi}{\Lambda}y\right)\right]^2 \qquad (4.1)$$

where Λ is the period, h_0 is an offset of the grating surface, and α and β are constants that describe the corrugation depth. The fluorophore is represented as a dipole that is randomly oriented and radiates to a spatial angle range $d\Omega = \sin(\theta)d\theta d\varphi$. The fluorescence intensity is described by $P(\theta,\varphi)$, where θ and φ are polar and azimuthal angles defined in Figure 4.1.

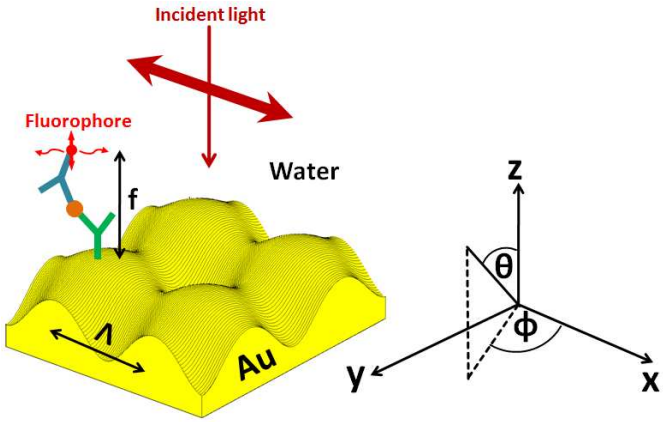

Figure 4.1 Schematic of investigated geometry composed of a crossed grating with an emitter placed above surface at a distance f. The emitter represents a fluorophore label attached to a detection antibody in a sandwich immunoassay with capture antibody (green), analyte (orange), and detection antibody (blue).

As an emitter, an organic Alexa Fluor 647 dye was used with the emission band centered at the wavelength $\lambda_{em} = 670\ nm$. The wavelength of the excitation beam $\lambda_{ex} = 633\ nm$ was chosen close to the peak absorption wavelength $\lambda_{ab} = 650\ nm$.

4.3 Simulations

A FDTD model was used for the simulation of the reflectivity, spatial distribution of the electric near-field intensity and far-field emission from an emitter as described in section 3.1. Material constant for gold was taken from literature [24] and the refractive index of water was taken as $n_b = 1.33$ (the dependence on wavelength was omitted). Electrical field intensity enhancement $|E/E_0|^2$ and reflectivity spectra were calculated with a single unit cell and periodic boundary conditions were applied in plus and minus *x*- and *y*-direction. Below the optically thick gold film (thickness 300 nm), a perfect metallic conductor was placed and in plus *z* direction (*z*=1500 nm) above the structure a perfectly matched layer (PML) was placed. A uniform mesh of 1 nm was chosen for the simulation region. The simulations for the reflectivity of the crossed grating include only reflected beam (diffraction order *m*=0, see section 3.1.3). In further simulations, the period of $\Lambda = 434\ nm$ was used and the coefficients describing the corrugation profile $h(x, y)$ of $\alpha = 4\ nm$ and $\beta = 2.5\ nm$.

As was explained in section 3.1.4, the periodic boundary conditions cannot be used for the simulation of far-field emission of a dipole representing the fluorophore emitter in vicinity to a periodic structure. Instead, a big simulation cell containing a certain number of periods was defined and a dipole current source was positioned in the middle. The lateral size of the cell (of 46 periods in x and y directions) was chosen in order to achieve convergence. At boundaries of the cell (plus and minus, x-, y-, and plus z-direction) PMLs were placed. Below the optically thick gold grating perfect electric conductor was used as boundary condition (minus z direction). The wavelength of the dipole emitter was chosen to be $\lambda = 670\ nm$. The center part of the structure including one period (each in x- and y-direction) and the dipole source was modeled with a maximum mesh size of 2.5 nm, while the rest of the structure was modeled with a maximum mesh size of 5nm.

The enhancement factor EF defined by Eq. (3.13) and Eq. (3.14) was determined by taking into account two different positions of the dipole at the grating surface to include subtle differences in the SPP-mediated emission in different positions. The position of the randomly oriented emitter are shown in Figure 4.2 and are placed above the minimum and maximum of the surface corrugation $h(x, y)$. The perpendicular distance from the surface of *f*=15 and 20 nm was used, which takes into account typical size of sandwich immunoassay depicted in Figure 4.1.

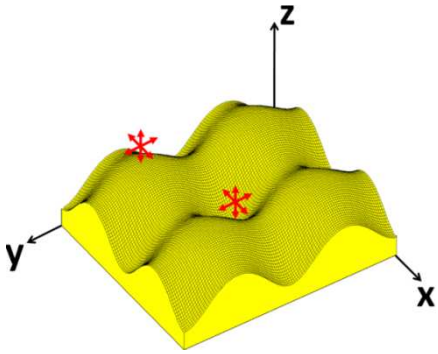

Figure 4.2 Sketch of emitter positions and orientations (red double arrows) for simulation of far-field emission and enhancement factor EF calculations.

4.3.1 Spectrum of modes

A plane wave hitting the surface of periodically corrugated surface of investigated Au grating can excite SPPs when the resonance condition Eq. (1.11) is fulfilled. As seen in the reflectivity spectrum in Figure 4.3, the resonance for normal incident light occurs at the wavelength of $\lambda = 636\,nm$ for the chosen geometry. The resonant coupling to SPPs through first order diffraction ($m = \pm 1$) is manifested as a narrow dip in the reflectivity spectrum and at its minimum at $\lambda = 636\,nm$ the reflectivity almost drops to zero (i.e., all incidence energy is coupled to SPPs and dissipated to heat due to the absorption losses in the Au). The full width half maximum (FWHM) of the resonance is $\Delta\lambda = 14\,nm$. The diffraction edge can be seen at $\lambda = 577\,nm$. As described by Eq. (3.8) below this wavelength $\lambda < 577\,nm$, the normal incident light can couple to $m = \pm 1$ diffraction orders. Above the diffraction edge $\lambda > 577\,nm$, only reflected beam (m=0) propagates to the far field.

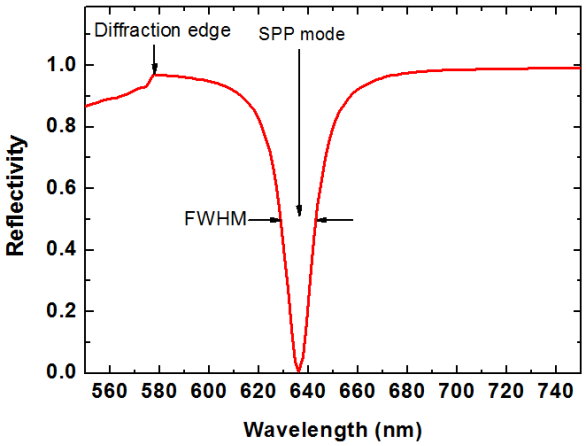

Figure 4.3 Simulated reflectivity spectra for normal incident light.

4.3.2 Near-field characteristics of diffraction-coupled SPPs

At the wavelength of the resonant excitation of SPPs, the intensity of incident light is confined at the grating surface, which leads to an electric field intensity enhancement $|E/E_0|^2$.

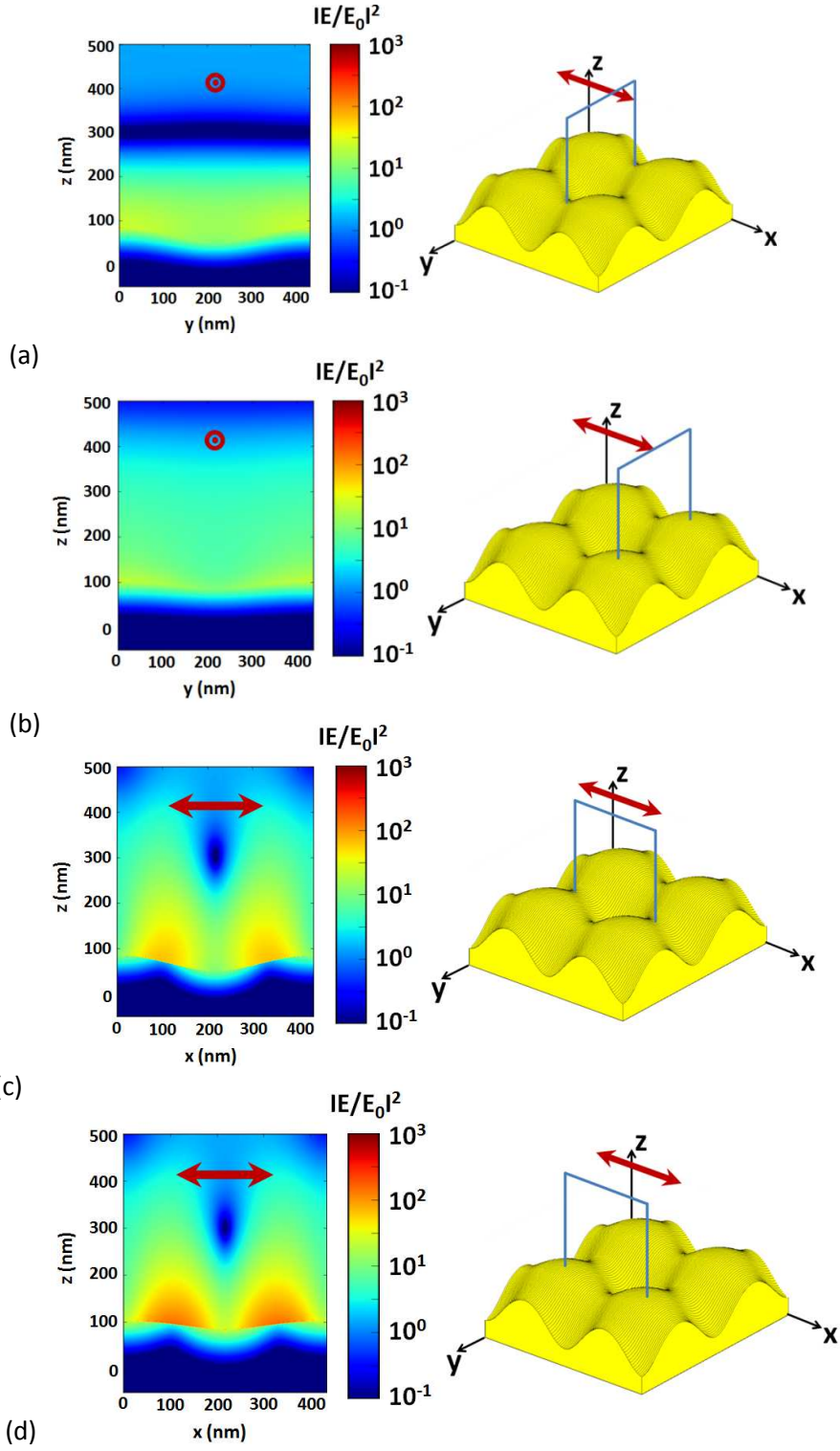

Figure 4.4 Electric near-field intensity distribution upon irradiation of Au grating with a normally incident plane wave at $\lambda = 636\ \mathrm{nm}$. The polarization (E vector) of the incident wave is indicated by a red arrow and the respective cross-sections as blue frames (graphic adapted from [145]).

Figure 4.4 shows several cross sections of the electric near-field intensity distribution that concentrate the energy of incident field at the distance up to about 100 nm from the gold surface. Different cross sections illustrate that the field substantially varies when moving around the surface of the unit cell and peaks at the walls of the modulation.

As in the experiments, emitters are randomly placed at the Au surface in the unit cell, let us calculate the average electric field intensity depending on the distance d from the gold surface. In Figure 4.5, the surface averaged field intensity enhancement in dependence of the distance d to the gold surface is shown. As seen in Figure 4.5 (b), for certain distance d, a virtual conformal modulated surface was defined and the average electric field intensity enhancement $|E/E_0|^2$ was calculated. The data presented in Figure 4.5 (a) was obtained for a mesh size of 1 nm. The highest average field intensity enhancement of $|E/E_0|^2$=60 occurs at the Au surface and the field exponentially decays into the dielectric water medium with a penetration depth of $z_p = 115\,nm$ (the distance at which the electric field drops by a factor of 1/e). At the distance of *d*=20 nm from the surface, where a fluorophore label is assumed to be attached, the average field intensity enhancement reaches $|E/E_0|^2$=44. The strongest component of SPP electric field intensity is the out-of-plane component (E_z), which agrees with other previous studies [17].

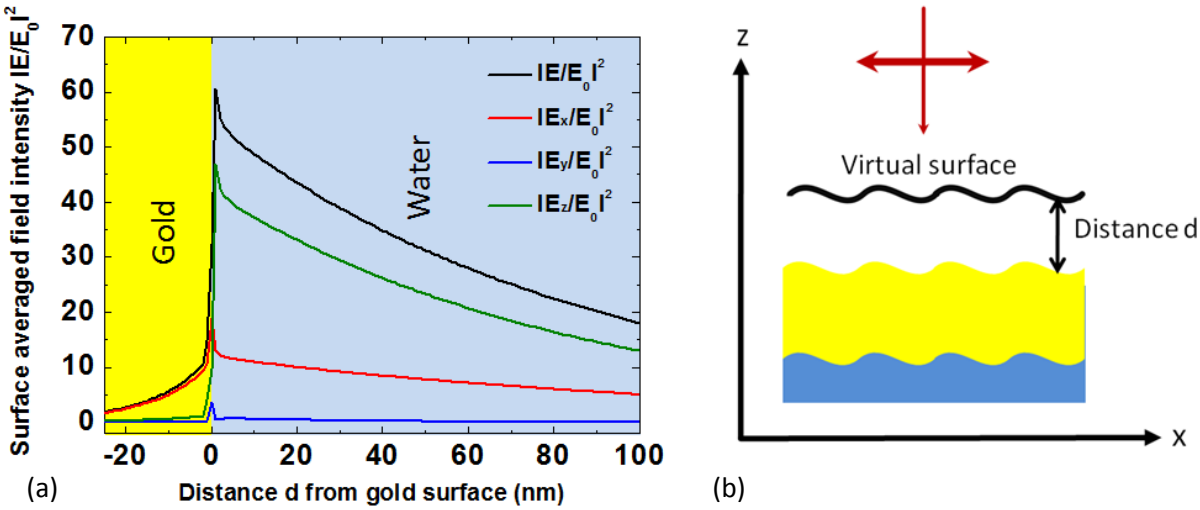

Figure 4.5 (a) Surface-averaged field intensity enhancement of the grating dependent on the distance d to the gold surface for normally incident plane wave. The incident field intensity in Cartesian components is $E_{x0}=E_0$, $E_{y0}=0$, and $E_{z0}=0$. (b) The method for calculation of the averaged field intensity is depicted.

Let us note that the average field intensity enhancement $|E/E_0|^2$ is significantly higher for investigated grating coupled-SPP structure compared to that observed for Kretschmann configuration [105]. Even when the same material constants of Au and water are used, the field intensity due to coupling to SPPs via diffraction is about three-fold higher than that by ATR with

Kretschmann geometry. This can be explained by the difference in the angle of incidence θ. The illuminating of a surface at tilted angle (e.g. θ=71 deg for ATR with BK7 glass prism) leads to a decrease of the intensity by a factor of cos (θ) which is roughly 1/3, compared to normal incident light.

To evaluate the field intensity enhancement of the grating, the electric field intensity distribution of a normal incident plane wave from a flat and thick reference Au surface is shown in Figure 4.6. These results show an oscillating intensity profile due to the interference between the incident and reflected wave. At the interface between the gold and water, the electric field intensity decays exponentially into the gold. The field strength at the distance $d = 20\ nm$ reaches the value of $|E/E_0|^2 = 1.36$.

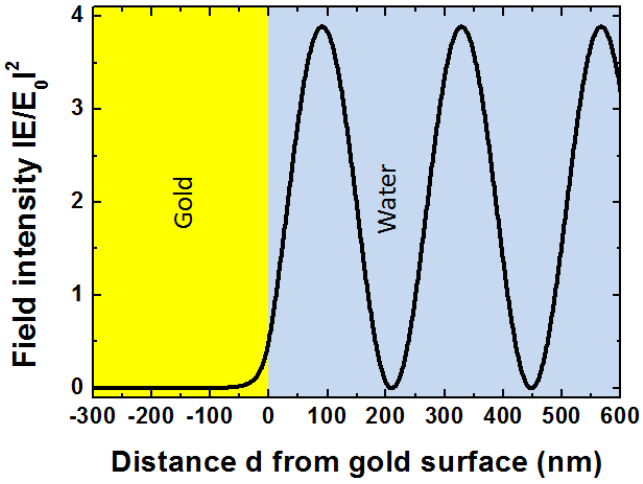

Figure 4.6 Distance d dependent electric field intensity for a normal incident laser beam on a thick gold film.

4.3.3 Fluorescence emission mediated by diffraction-coupled SPPs

This sections presents the far-field angular distribution of light intensity emitted by a fluorophore emitter close to nanostructure that is represented as a dipole placed at the distance *f*=20 nm from the metal surface. The emitted light intensity at the wavelength of $\lambda_{em} = 670\ nm$ is obtained as a function of polar and azimuthal angles $P(\theta, \varphi)$, which is averaged over the position of the emitter on the surface of a unit cell (shown in Figure 4.2) and all possible orientations. $P(\theta, \varphi)$ is used for the prediction of collection efficiency CE (defined by Eq. (3.11)) when a lens with a finite numerical aperture of $NA = 0.2$ (corresponding to an angular cone with the polar angles $\theta_{lens} = 8.7\ deg$ in water and $\theta_{lens} = 11.5\ deg$ for air) is used for collection of the emitted light to a detector.

First the emission of a dipole above a flat metallic surface (as a reference system) is examined. Figure 4.7 (a) shows a normalized $P(\theta, \varphi)$, which shows a rather homogenous distributed intensity.

The integration of the intensity of emitted light to the chosen numerical aperture NA and its comparison with the total emitted power reveals that a small fraction of the emitted photons can be collected. The obtained results shows that the collection efficiency yields the value of $CE = 1.4\ \%$.

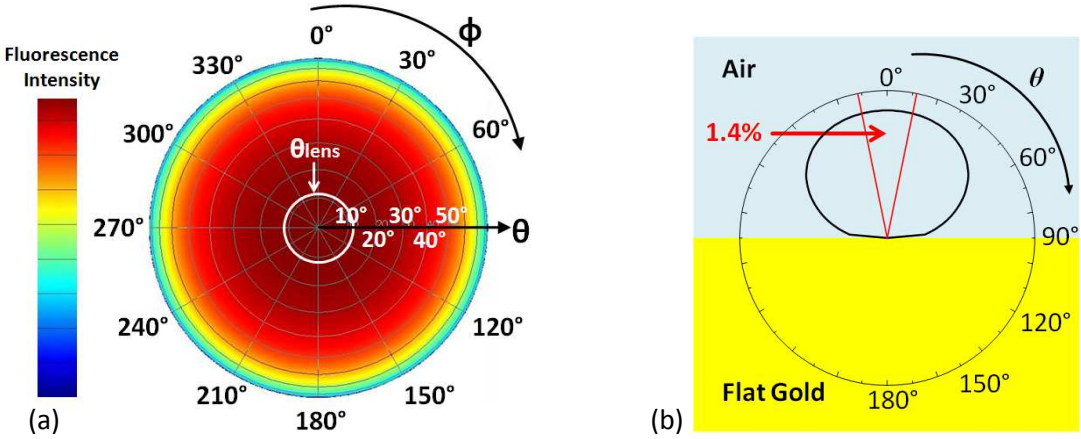

Figure 4.7 (a) Angular distribution of far-field fluorescence intensity $P(\theta, \varphi)$ for randomly oriented emitter at a distance of $f = 20\ nm$ from a flat gold surface in contact with water is shown. The emission wavelength is assumed to be $\lambda_{em} = 670\ nm$. The collection range of the lens θ_{lens} is represented as a white circle. (b) Shows a cross section $P(\theta, \varphi = 0)$ and the red marked area indicate the range of the lens θ_{lens} (for $NA = 0.2$). Angles θ and φ are taken in air (graphic adapted from [145]).

When the Au surface is corrugated, a dramatically different angular distribution $P(\theta, \varphi)$ is obtained (see Figure 4.8). It reveals that $P(\theta, \varphi)$ exhibits a series of bright bands, which correspond to diffraction out-coupling of the emitted light (generated by the radiating dipoles) by SPPs.

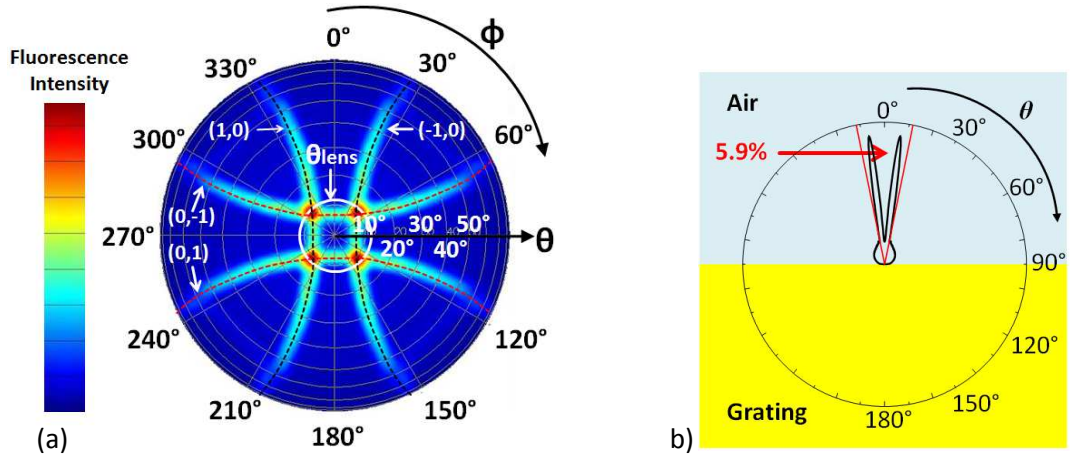

Figure 4.8 (a) Angular distribution of far-field fluorescence intensity $P(\theta, \varphi)$ for randomly oriented emitter at a distance of $f = 20\ nm$ from a corrugated gold surface in contact with water is shown. The emission wavelength is assumed to be $\lambda_{em} = 670\ nm$. The collection range of the lens θ_{lens} is represented as a white circle and the dotted lines indicate the SPP orders. (b) Shows a cross section $P(\theta, \varphi = 0)$ and the red marked area indicate the range of the lens θ_{lens} (for $NA = 0.2$). Angles θ and φ are taken in air (graphic adapted from [145]).

Similar to the reflectivity that exhibits narrow resonance feature associated with SPR (see Figure 4.3), the emitted angular bands are narrow and efficiently confine the emitted light intensity. For the chosen period Λ of the grating, the emission is substantially confined within the NA of the lens and provides about four times better collection efficiency of *CE*=5.9% with respect to the flat Au surface. In order to elucidate the origin of highly directional SPP-mediated emission, let us analytically analyze the diffraction out-coupling SPP modes on a crossed diffraction grating. The near-field excited SPPs become out-coupled to the far-field when the relation for conservation of momentum is fulfilled (see section 1.2.2):

$$k_{SPP}^2 = \left(k_0 \sin(\theta)\sin(\varphi) \pm m k_g\right)^2 + \left(k_0 \sin(\theta)\cos(\varphi) \pm n k_g\right)^2 \qquad (4.2)$$

where k_{SPP} is the wave vector of SPPs defined by Eq. (1.2), k_0 is the vacuum wave vector, k_g is the grating wave vector, and m and n denote the diffraction orders ($m, n = 0,1,2\ldots$). Eq.(4.2) has solutions for certain set of values of θ and φ. The solutions of Eq. (4.2) are sketched in Figure 4.8 and the bright branches are labeled with the diffraction order (m, n).

4.3.4 Amplification of fluorescence signal

As introduced in section 3.1.6, the previous simulations on the field intensity $|E/E_0|^2$ at the excitation wavelength and directional fluorescence emission at λ_{em} provides information based on which the fluorescence intensity enhancement factor EF can be calculated (see Eq. (3.13) and (3.14)). It need to be noted that for the EF calculation the surface averaged electric field intensity (see Figure 4.5) was considered rather than the electric field intensity at the different dipole positions (see Figure 4.2). This approach was pursued due to the inhomogeneous electric field distribution on the grating surface (see Figure 4.4), where otherwise a large number of simulations of different dipole positions would have been necessary. The results are summarized in Table 4.1 where the enhancement factor EF (fluorescence signal collected by a detector from an emitter above the metallic structure is compared to that from an emitter in water without any substrate) is compared for the flat Au surface and corrugated Au surface. The two different dipole positions considered in the simulation (see Figure 4.2) exhibit same results for change of intrinsic quantum yield and collection efficiency and therefore justify, that only two positions have been considered. The table shows the key contributions ($|E/E_0|^2$, CE, and change of quantum efficiency η/η_0) for the intrinsic quantum efficiency of $\eta_0 = 0.33$ that corresponds to Alexa Fluor 647 dye.

	Flat gold ***f*= 15 nm**	**Grating** ***f*= 15 nm**	**Flat gold** ***f*= 20 nm**	**Grating** ***f*= 20 nm**
$\|E\|^2/\|E_0\|^2$	1.12	46.1	1.36	43.6
η/η_0	0.68	0.68	0.84	0.82
CE	1.3 %	6.1 %	1.4 %	5.9 %
$EF_{grating}/\ EF_{flat}$ at respective distance	**134** ($\vec{\mu}_{ab}$ aligned to $\vec{\mu}_{em}$) **145** ($\vec{\mu}_{ab}$ random to $\vec{\mu}_{em}$)		**86** ($\vec{\mu}_{ab}$ aligned to $\vec{\mu}_{em}$) **96** ($\vec{\mu}_{ab}$ random to $\vec{\mu}_{em}$)	

Table 4.1 Performance characteristics of fluorescence signal delivered from a fluorophore emitter at two different distances *f* from the flat Au surface and the corrugated Au surface.

Let us note that the EF is not exactly a product of the three key contributions due to the averaging over the orientation of absorption and emission dipoles (see Eq. (3.13) and (3.14)). The EF depends only weakly on the orientation of the absorption dipole $\vec{\mu}_{ab}$ with respect to the emission $\vec{\mu}_{em}$ dipole (which relates to a situation when the emitter is rotating or is static upon the emission). The results show that the fluorescence signal amplification due to the corrugating of the Au surface is higher at the distance *f*=15 nm than at *f*=20 nm and reaches values between 86 and 145. The main reason for the higher *EF* at *f*=15 nm than *f*=20 nm is, that on the corrugated surface the field strength is decreasing with the distance f (see Figure 4.5) while on the flat surface it is increasing (see Figure 4.6).

Interestingly the change of quantum efficiency η/η_0 is almost identical on corrugated and flat Au surface for the two investigated distances f. The intrinsic quantum efficiency of a system is highly changed at sharp geometrical features [44]. As the crossed sinusoidal grating is only weakly modulated, the fluorophore interacts quasi with a flat surface. These findings are confirmed by lifetime measurements of Eu^{3+}-ions on top of an optically thick sinusoidal silver grating (silver thickness 200 nm) with period $\Lambda = 415\ nm$. The period is comparable to the period used in this work. It is shown that the lifetimes of excited states are similar for flat silver and grating when the amplitude is small (around 20 nm), while they differ significantly when the amplitude is increased (above 40 nm) [30].

4.4 Experimental

4.4.1 Grating preparation

A master of the corrugated structure has been prepared by interference lithography and afterwards multiple copies were prepared by UV nanoimprint lithography (see section 3.2 for details). Firstly, a cleaned BK7 glass substrate was coated (spin coating at 5000 rpm for 45 s) by a photoresist Microposit S1805 (from Shipley Company) and soft baked on a hot plate at 95°C for 2min. Afterwards the sample was mounted to a laser interference lithography setup. The angle of interfering beams from a HeCd laser (model IK 3031 R-C from Kimmon) at wavelength $\lambda = 325\,nm$ was set to 21.97 deg which corresponds to a period of $\Lambda = 434\,nm$ (see Eq. (3.20)). The photoresist layer on the BK7 glass substrate was exposed for 120 s to the interference field (with intensity of 15.7 μW/cm^2). Then the substrate was rotated by 90 deg and exposed one more time under the same conditions. After the exposition, the relief corrugation was etched to the resist by the developer AZ 303 (from MicroChemicals mixed with distilled water in the ratio 1:14 for t_{dev}=80 s).

This structure was used as a master for further replication by nanoimprint lithography. Firstly, polydimethylsiloxane elastomer (PDMS Sylgard 184 from Dow Corning) was casted to the corrugation and cured at room temperature for 3 days and served as a working stamp. Let us note that the period of the structure that was transferred to PDMS can be tuned by temperature in the curing process, as PDMS exhibits relatively high thermal expansion coefficient of $3 \cdot 10^{-4}\frac{1}{K}$ [146]. By using the PDMS working stamp, multiple copies of the structure were prepared by imprinting into UV-curable polymer Amonil MMS 10 (from AMO GmbH). The UV-curable polymer was spin coated on a cleaned BK7 glass substrate at 3000 rpm for 120 s which results in a layer thickness of (110 +/- 7) nm (after the curing). Then, the PDMS working stamp is placed on the top of the surface and irradiated to UV light (UV lamp Bio-Link 365, Vilber Lourmat) at λ=365 nm. The irradiation dose was $10\,J/cm^2$. Finally, the PDMS stamp was detached from the cured Amonil MMS 10 leaving a copy of the master structure. Let us note that more than 8 copies can be prepared by using a single working stamp.

The copied gratings were subsequently coated with 4 nm of Cr and 100 nm of Au by vacuum thermal evaporation (HHV AUTO 306 from HHV LTD) in vacuum better than $1 \cdot 10^{-6}\,mBar$. The thin Cr-layer promotes adhesion of Au to Amonil and prevents its delamination. Let us note that each grating sample comprised an area that was structured and an area that was flat and served as a reference in the further optical measurements.

4.4.2 Morphology of prepared gratings

In order to analyze the profile of periodic corrugation of prepared gratings, atomic force microscopy (AFM) in tapping mode was used. The used cantilever was PPP-NCHR (from NANOSENSORS with force constant 42 N/m and resonance frequency around 300 kHz). An example of AFM image of replicated grating coated with Au is shown in Figure 4.9 (a). This data reveals that the period of the fundamental spatial frequency is $\Lambda = 435 \pm 3\ nm$ which is in excellent agreement with the targeted period of $\Lambda = 434\ nm$. In addition, Figure 4.9 (b) shows two cross sections of the corrugation height that cut the peaks (red line in Figure 4.9 (a)) and valleys (black line in Figure 4.9 (a)) of the prepared grating. The comparison of both profiles reveal that the modulation profile is substantially different from two crossed gratings with each sinusoidal dependency (where in both profiles the amplitude of the oscillation would be the same). This is due to the fact that the crossed grating is not only composed of crossed sinusoidal modulations with the fundamental period Λ, but also other additional spatial periods are present.

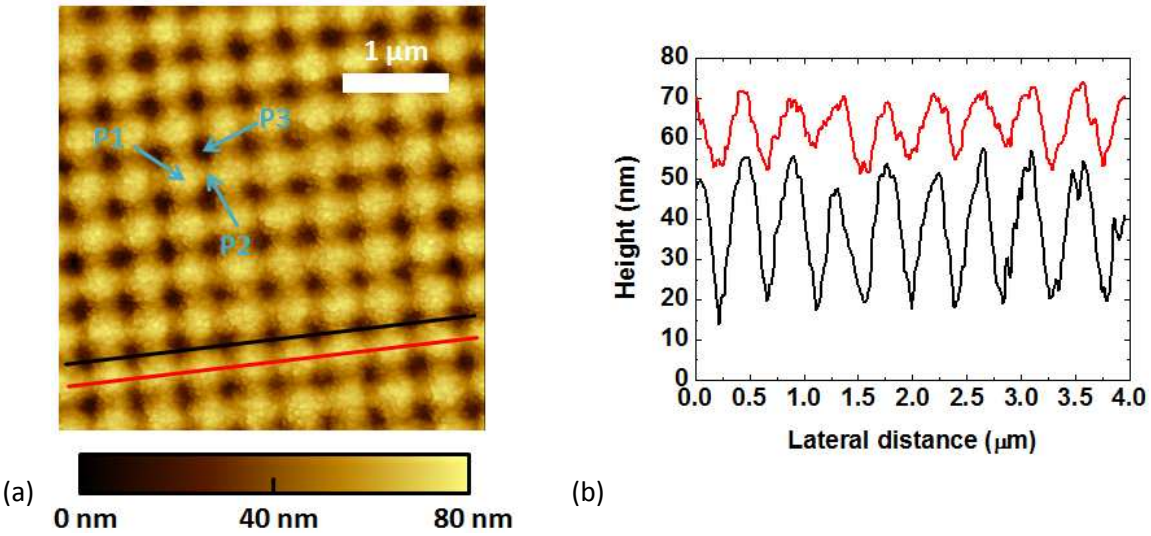

Figure 4.9 (a) AFM image of Au-coated replica prepared from a master that was developed for t_{dev}=80 s and (b) cross-sections of the modulation height of the grating as indicated with the red and black line in (a).

In order to describe the corrugation, Eq. (4.1) was used and the parameters, α and β were determined. Let us note that the parameter β takes into account non-linear behavior of the photoresist and possible deviations from sinusoidal profile of the interference field recorded:

$$\mathrm{I(x,y)} = \mathrm{I_0}\left\{cos\left(\frac{2\pi}{\Lambda}\cdot \mathrm{x}\right) + cos\left(\frac{2\pi}{\Lambda}\cdot \mathrm{y}\right) + 2\right\}, \tag{4.3}$$

with I_0 the intensity of the UV-laser beam incident on the substrate in interference lithography. In order to determine the parameters h_0, α and β, the grating height at three characteristic points P1, P2, and P3 that are marked in Figure 4.9 (a) were measured. Point P1 is located at the global maximum, P3 at the global minimum and P2 at the saddle point between two maxima. The height values h at these points with the respective interference light intensity from Eq. (4.3) are shown in Table 4.2:

Location	Height value h [nm]	Intensity
P1	70±2	$0 \cdot \mathrm{I}_0$
P2	53±2	$2 \cdot \mathrm{I}_0$
P3	18±2	$4 \cdot \mathrm{I}_0$

Table 4.2 Measured height values of the three chosen points and the respective interference light intensities.

By using equation (1.1) and solving three equations for the three different points, the parameters of $h_0 = 70\ nm$, $\alpha = 4\ nm$ and $\beta = 2.25\ nm$ were derived and used in simulations described before.

4.4.3 Spectrum of SPP modes

Series of master gratings were prepared by exposure of the resist to the interference field of HeCd laser and developed for different times between 40 s and 90 s that was followed by direct coating with Au (without replication by NIL) as specified in section 4.4.1. In order to optimize the grating depth to achieve full coupling of incident light beam to SPPs at the excitation wavelength λ_{ex} (that is close to the absorption band of a dye λ_{ab}), a series of wavelength reflectivity curves were measured at the angle of incidence $\theta = 0.6\ deg$. Let us note that the TM and TE reflectivity are almost identical as the deviation from normal incidence is very small. The results presented in Figure 4.10 (a) reveal that with increasing development time the resonant SPR dip due to the first diffraction order coupling to SPPs gets more pronounced and broader. In addition it can be seen that the resonance position shifts to higher wavelength with increasing etching time. The resonance shifts from λ_{SPR}=632.2 nm for 40 s development time to λ_{SPR}=639.5 nm for 90 s.

For further studies we replicated the structure with 80 s development time with NIL and evaporated 100 nm of Au on it. The reflectivity spectra is shown in Figure 4.10 (b) and shows that strong coupling of incident beam of about 97 percent at the resonance is achieved. In addition, one can see that the resonance on the replica is shifted by 8 nm to 631.5 deg, which excellently matches the excitation wavelength $\lambda_{ex} = 633\ nm$ (of the used HeNe laser) used for further experiments. As the resonance position is mostly determined by the period Λ of the grating, it can be assumed that

the change in resonance position is due to a slight change of period Λ due to NIL replication with the working stamp and its transfer to UV-curable Amonil MMS 10 resist. The period Λ of the grating can be determined from the diffraction edge at $(579 \pm 2)\, nm$ which is solely dependent on the period and the refractive index of the surrounding medium and not on the optical constants of the gold. The equation of this relation is $\lambda_{edge} = n\Lambda$ (introduced in section 3.1.3) with n the refractive index of the surrounding medium (in this case water) and Λ the grating period. Therefore the period derived from the optical measurement is $(435.3 \pm 1.5)\, nm$. This value is in good agreement with the period determined from AFM measurements ($\Lambda = (435 \pm 3)\, nm$). Additionally to the SPR resonance, another dip in the reflectivity spectra occurs at the wavelength λ=670 nm. The origin of this feature is not clear.

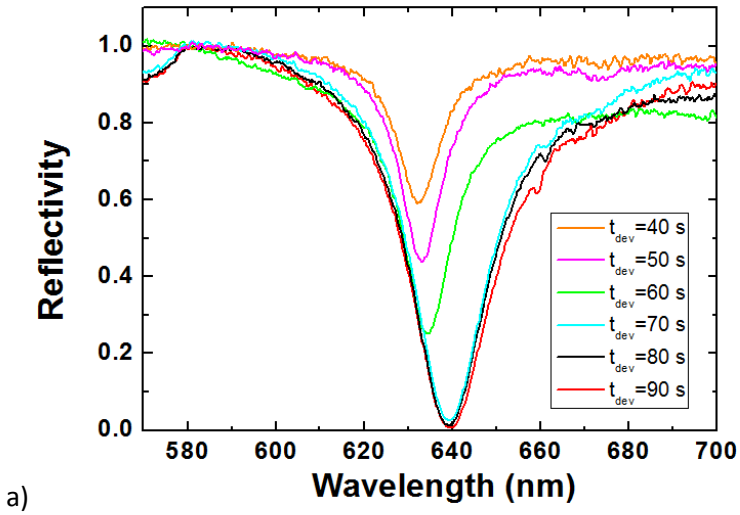

a)

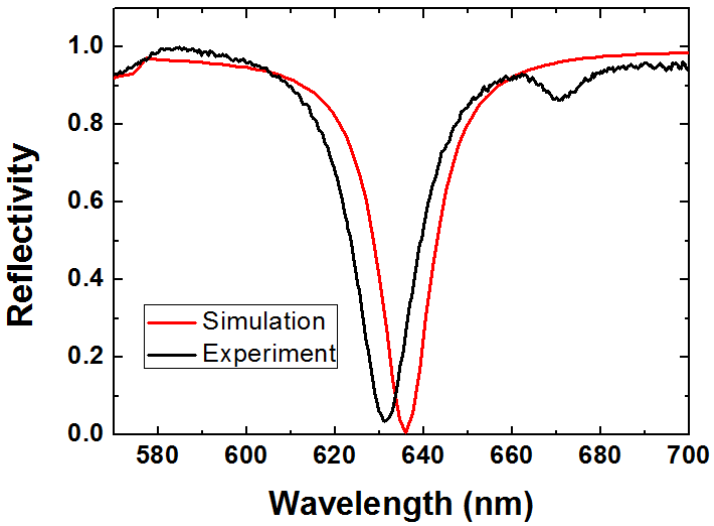

b)

Figure 4.10 Wavelength reflectivity curves for TE polarization and angle of incidence θ=0.6 deg for (a) master gratings and (b) replica grating coated with Au and brought in contact with water. In addition the simulated reflectivity curve from section 4.3.1 is replotted for comparison. The experimental reflectivity curves have been normalized to the intensity measured at the critical wavelength λ=580 nm.

For comparison, the simulated reflectivity curve of section 4.3.1 has been replotted in Figure 4.10 (b). The simulated curve shows slightly higher SPR at 636 nm and reflectivity drops to almost zero. The shape of the resonances of the experiment and the simulation are quite similar. The FWHM of the experiment is $\Delta\lambda = 16.4\,nm$, while the FWHM of the simulation is $\Delta\lambda = 13.8\,nm$. The width of a resonance is a measure of the lifetime of an excited state and in case of SPPs also a measure for the propagation length and near-field intensity. As the simulation gives a slightly smaller width as the experiment, the electric field intensities from the simulation will be likely marginally overestimated. The bigger FWHM in the experiment might be explained by the surface roughness of the gold surface, which was not considered in the numerical simulations. Surface roughness decreases the propagation length and thus increases the width of the resonance. It can be seen in Figure 4.10 (b) that the diffraction edge of the simulated and experimental results are in good agreement.

In Figure 4.11 the angle-wavelength maps for TM-polarized and TE-polarized light of the corrugated Au surface are shown. The TM-reflectivity map shows the typical behavior of a grating in which the one resonance at zero degree splits into two branches when increasing the angle. The two branches can be explained by the SPP dispersion and are the (m=+1, n=0)-mode and the (m=-1, n=0)-mode.

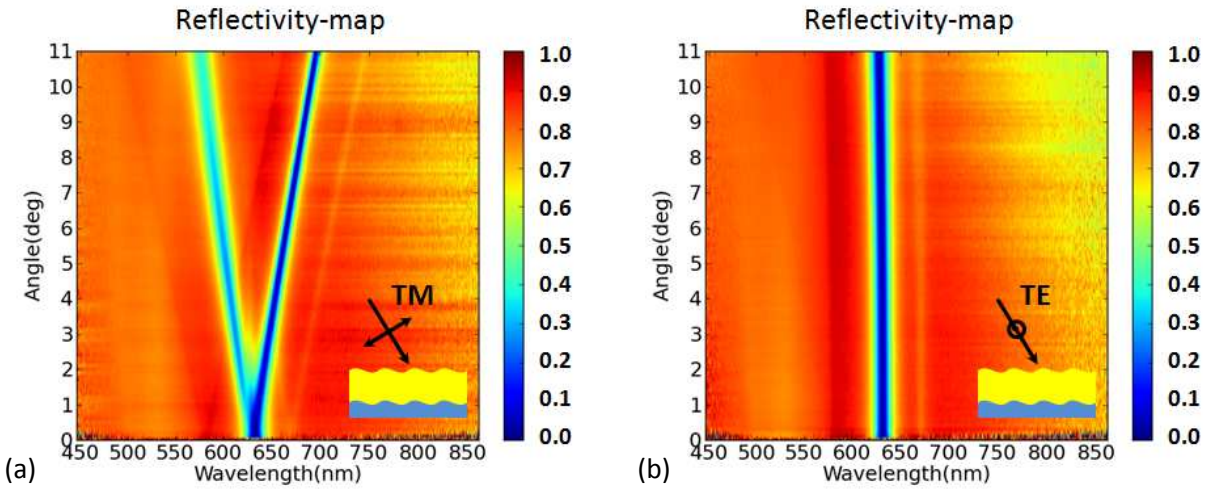

Figure 4.11 Angular and wavelength dependence of reflectivity for (a) TM-polarization and (b) TE polarization (graphic adapted from [145]).

The relation for excitation of SPPs on a 1D grating is given as:

$$k_{SPP}^2 = \left(k_{gx} + k_x\right)^2 \qquad (4.4)$$

with k_{SPP} wave vector of SPPs, k_{gx} grating wave vector and k_x wave vector of incident wave in x-direction (in-plane component). Substituting into this equation the definitions (see section 1.2.2) of the quantities and setting the azimuthal angle $\varphi = 0$, the equation can be rewritten as:

$$\left(\frac{2\pi}{\lambda}\cdot\sqrt{\frac{\varepsilon'_m(\lambda)\cdot\varepsilon_d}{\varepsilon'_m(\lambda)+\varepsilon_d}}\right)^2 = \left(m\cdot\frac{2\pi}{\Lambda} + n_d\cdot\frac{2\pi}{\lambda}\cdot\sin\theta\right)^2 \qquad (4.5)$$

with λ the wavelength of the incident light, $\varepsilon'_m(\lambda)$ the real part of the permittivity of gold, ε_d permittivity of water, m grating order, θ polar angle and n_d refractive index of water. As the real part of the permittivity of gold $\varepsilon'_m(\lambda)$ is not an analytical function, this equation cannot be solved analytically. Therefore in Figure 4.12 the equation is graphically solved by assuming the left and the right part of the equation is a function of λ. The intersection is thus the wavelength, at which the equation is fulfilled. The angle θ and the grating order m, can be set as parameters which can be varied.

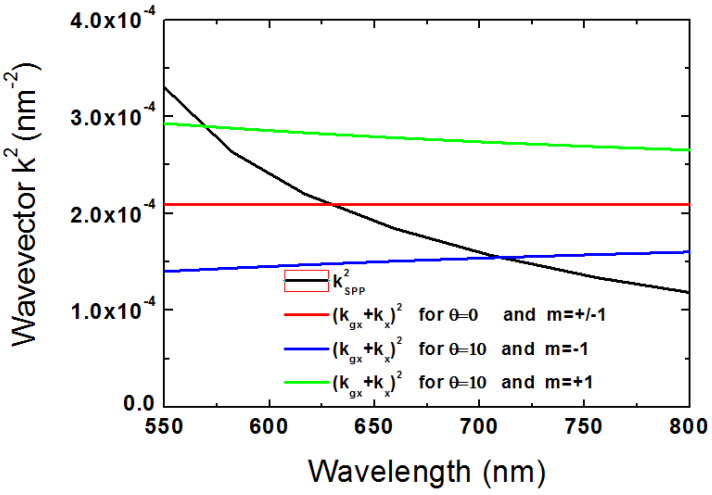

Figure 4.12 Graph of the wave vector of SPPs and grating vector plus incident light wave vector for different grating orders and different incident angles.

In Figure 4.12 the equation is solved for normal incident light at $\theta = 0$ deg and for $\theta = 10$ deg with m=-1 and m=+1. It can be seen that for $\theta = 0$ deg there is only one intersection for $m = \pm 1$ at 628 nm, which agrees to the experimental resonance position at 631.5 nm. For $\theta = 10$ deg there are two intersections for m=+1 at lower wavelength and m=-1 at higher wavelength. These findings explain the splitting of the dispersion relation in Figure 4.11 (a). The TE-reflectivity in Figure 4.11 (b) map does not show a pronounced angular dependence. Only a slight shift to lower wavelength is seen,

when increasing the angle. The resonance position is not shifted as the in plane component of the polarization is not changing in TE-mode.

4.4.4 Angular distribution of SPP-mediated fluorescence emission – optical setup

In order to characterize the angular distribution of emitted fluorescence light on crossed grating structure, a setup shown in Figure 4.13 was built up. The setup consists of a red He-Ne laser emitting at λ_{ex}=632.8 nm. Right after the laser there are two polarizers to first manipulate the polarization of the laser and second to be able to control the intensity of the laser. An additional laser band pass filter (FL632.8-10 from Thorlabs) is used to cut all wavelengths different from λ_{ex}. Afterwards the laser is incident on a dichroic mirror (XF2087 660DRLP from Omega Optical) and is reflected towards a microscope objective lens (36-133 from Edmund Optics). The dichroic mirror is designed to reflect the laser light at λ_{ex} for the angle of 45 deg and transmit the fluorescence light at λ_{em}=670 nm. The used microscope objective lens has a numerical aperture of *NA* = 0.65 (working distance WD=0.52 mm) and thus allows to collect fluorescence light in air from a cone with polar angle below θ=40.5 deg. The lens was arranged in a way that the sample with the flat gold or Au diffraction grating was at the focal length of the lens. The fluorescence light emitted from the sample was collected by the microscope objective lens and passed through the dichroic mirror followed by a set of filters. Firstly, a notch filter (XNF-632.8-25.0M from CVI Melles Griot) was used to block the excitation wavelength λ_{ex}.

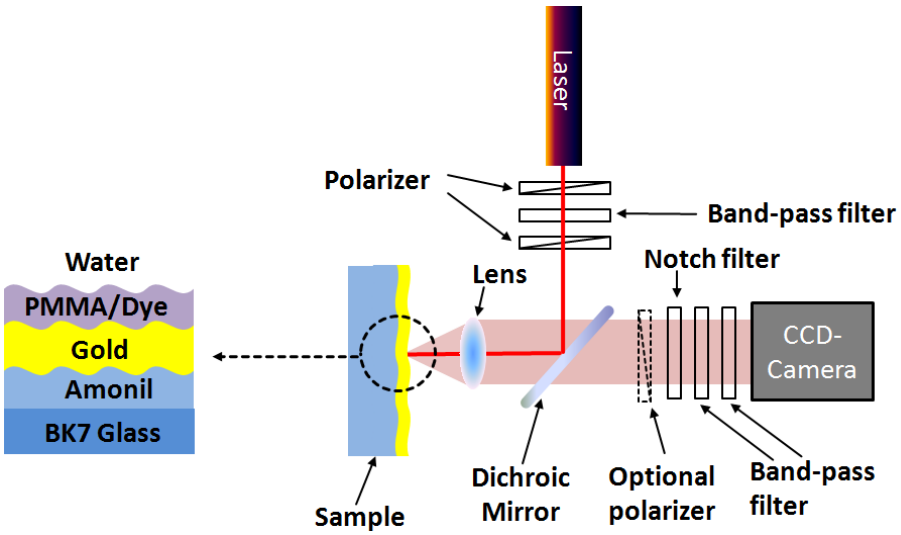

Figure 4.13 Sketch of the measurement system for detection of angular distribution of emitted fluorescence intensity. The inset shows the structure under study.

Afterwards two bandpass filters (FB670-10 from Thorlabs and 670FS10-25 from Andover Corporation Optical Filter) with the transmission window at the λ=670 nm were used. Let us note that the microscope objective lens converted the angular distribution of emitted light intensity to spatially resolved image detected by a CCD camera (EM-CCD iXon + 885 from Andor Tchnology). The CCD

camera was cooled by a Peltier element to -50 °C to reduce the pixel noise. Every measurement was background compensated. In order to achieve sufficient signal-to-noise ratio, images were accumulated for about 20 s and averaged.

The sample indicated in the inset in Figure 4.13 is a crossed grating that is subsequently coated by Au film and an organic dye dispersed in a poly(methyl methacrylate) (PMMA, Sigma-Aldrich). Firstly 1,1'-dioctadecyl-3,3,3′,3′-tetramethylindodicarbocyanine, 4 chlorobenzene-sulfonate salt (DiD, from Invitrogen) was dissolved in toluene at 1.8 mM concentration. In addition, PMMA was dissolved in toluene at a concentration of 0.25 wt%. The PMMA-toluene solution and the DiD-toluene solution were mixed in a ratio of 30 : 1. Afterwards this mixture was spin coated over the gold surface at 3000 rpm for 60 s and dried for 60 mins. The layer was intentionally kept thin in order to approximate the surface mass density of proteins in future assay experiments and not to shift the SPR too much from the initial wavelength of 631.5 nm. Figure 4.14 shows, that the resonance shifts due to the additional DiD-doped PMMA layer by 4 nm to the wavelength of λ=635.2 nm, which corresponds to the thickness of 6 nm. In order to approximate the conditions in assay experiments, a drop of water was placed on the surface and covered with a thin microscope cover glass.

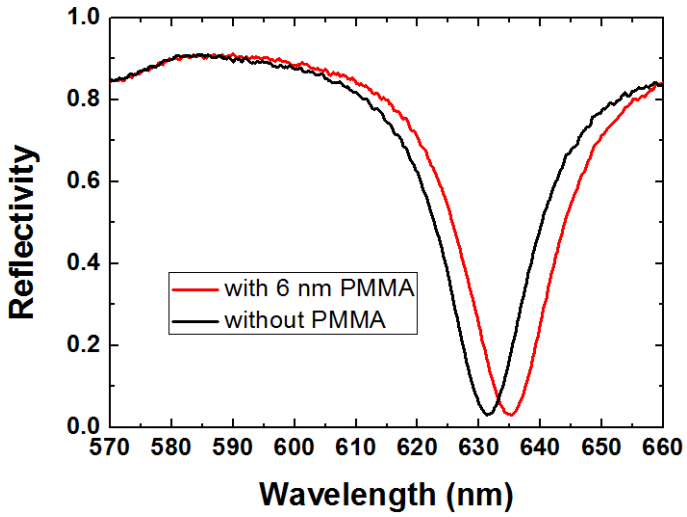

Figure 4.14 A crossed grating was brought in contact with water and the reflectivity was measured at the angle of incidence θ=0.6 deg. SPR shift due to the deposition of 6 nm of PMMA doped with DiD dye.

4.4.5 Angular distribution of SPP-mediated fluorescence emission – results

The DiD dye was chosen for the measurements of angular distribution of fluorescence emission mediated by grating-coupled SPPs. The reason is that it exhibits similar absorption ($\lambda_{ab} = 644\ nm$) and emission ($\lambda_{em} = 665\ nm$) wavelengths as Cy5 and Alexa Fluor 647 used as labels in assays. The angular distribution of fluorescence intensity $P(\theta, \varphi)$ emitted at $\lambda_{em} = 670\ nm$ from an identical DiD-doped PMMA layer deposited on developed crossed Au grating and a reference sample with flat Au surface are compared in Figure 4.15.

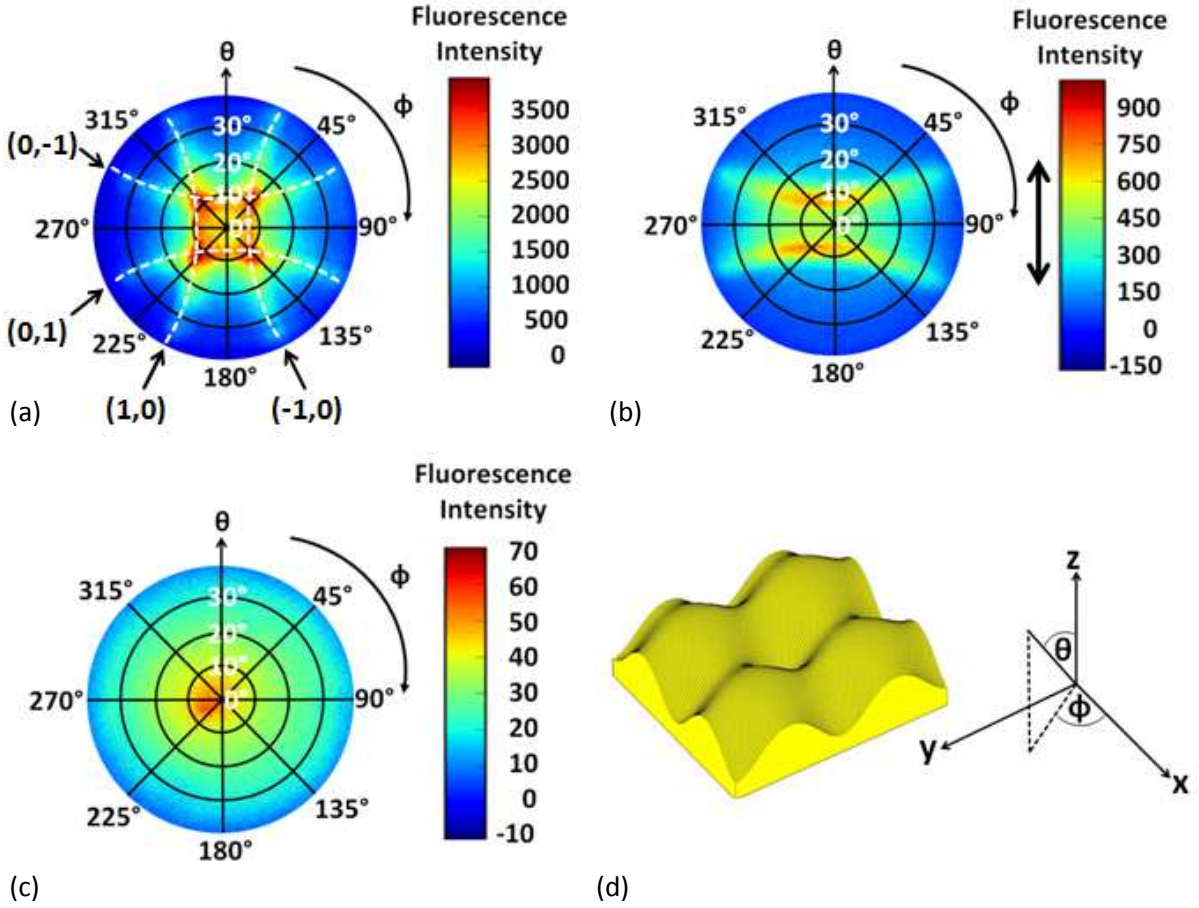

Figure 4.15 Angular distribution of fluorescence intensity $P(\theta, \varphi)$ at λ_{em}=670 nm for flat and corrugated Au coated with layer of DiD dye-doped PMMA. Crossed grating structure with (a) no polarizer before the CCD camera and (b) a linear polarizer before the CCD camera (polarization is indicated by black double arrow). (c) Flat Au surface with no polarizer before the CCD camera. (d) Definition of used polar θ and azimuthal φ angles (graphics adapted from [145]).

All these data were measured with the monochromatic incident beam, linearly polarized along the *x*-axis of the structure (see Figure 4.15 (d)). Figure 4.15(a) shows that the fluorescence emission from the crossed grating is concentrated to four branches corresponding to the SPP out-coupling via

diffraction modes (m=±1,n=0), (m=0,n=±1). The emission branches can be analytically explained by solving Eq. (4.2) which is indicated by dashed white lines. Figure 4.15 (b) illustrates that the SPP out-coupled branches are linearly polarized and that they carry about two orders of magnitude higher intensity than that observed for a flat Au surface in Figure 4.15 (c).

Interestingly, acquired fluorescence intensity distribution $P(\theta, \varphi)$ from crossed gratings (Figure 4.15 (a)) is independent on the polarization of the incident light beam. This is surprising as the emitting fluorophores are embedded in the PMMA polymer and thus can be assumed as static dipoles. If the intrinsic absorption dipole moment μ_{ab} is aligned with the emission dipole moment μ_{em}, one would expect that the polarized normal incident light beam at λ_{ex} excites preferably emitters oriented parallel to the incident electric field intensity. These fluorophores should then emit preferably to the same polarization. The fact that this is not observed is possibly due to the fact that coupling to SPPs is associated with the strongest enhancement of the electric field intensity component that is perpendicular ($|E_z/E_0|^2$) to the surface (see Figure 4.5 (a)). Therefore, for both excitation by TM and TE-polarized beam dipoles with out-of-plane orientation are preferably emitting and thus no preferred polarization occurs. The highest fluorescence intensity is emitted to angles at which different SPP out-coupled diffraction modes intersect. In general, this feature allows for about two orders of magnitude increase in the fluorescence signal intensity emitted from identical DiD-doped PMMA layer with respect to that for a flat Au film, which agrees with simulations summarized in Table 4.1. However, let us note that the accuracy of these measurements is limited by strong bleaching of used DiD dyes that are exposed to focused excitation beam (see Figure 4.13). That makes quantitative comparison of the absolute numbers of the fluorescence enhancement difficult. For instance, one would expect that the maximum fluorescence intensity at Figure 4.15 (b) would be half of that presented in Figure 4.15 (a), as only one of two superimposed polarizations are detected. However, as $P(\theta, \varphi)$ in Figure 4.15 (a) was measured before that in Figure 4.15 (b), strong bleaching leads to stronger decreased intensity than expected.

In Figure 4.15 (c) the fluorescence emission from DiD-doped PMMA layer on a flat Au film is shown. The maximum fluorescence intensity occurs at the center and then slowly decays with increasing θ. In contrast, the crossed sinusoidal grating shows faster decay when increasing the angle θ to higher values. The maximum intensity for the flat gold surface is not exactly at $\theta = 0$ deg due to a slight possible misalignment of the microscope objective lens in front of the substrate which can lead to such distortions.

The observed emission branches of the crossed grating are broader than predicted by numerical simulations (see section 4.3.3). Possible explanations are imperfections in the optical imaging system and the finite width of the used band-pass filters in front of the CCD-camera of around FWHM=10 nm.

Finally, let us note that $P(\theta,\varphi)$ strongly depends on the emission wavelength λ_{em}. Figure 4.16 compares two measured $P(\theta,\varphi)$ from a crossed grating for two different band-pass filters before the CCD camera which transmit the wavelengths λ_{em}=670 nm and λ_{em}=694 nm (694FS03-25 from Andover Corporation Optical Filter). By increasing the wavelength λ_{em}, the diffraction out-coupled SPP branches shift to higher polar angles θ. As the conditions for coupling light to plasmons is the same as to outcouple plasmons at a certain wavelength, it is possible to predict the position of the emission branches by the angular-wavelength measurements shown in Figure 4.11 (a). To do so from the angular wavelength measurements in Figure 4.11 (a), reflectivity values at the wavelength 670 nm and 694 nm are extracted (see Figure 4.16 (c)). For the wavelength 670 nm, the SPR resonance occurs at θ=6.8 deg, while for 694 nm the resonance is at θ=10.7 deg. This is in good agreement with the data obtained from the measurements of angular distribution of fluorescence emission, where for λ_{em}=670 nm the emission branch for $\varphi = 0$ is well below θ =10 deg and for emission wavelength of λ_{em}=694 nm the emission branch for $\varphi = 0$ is above θ =10 deg.

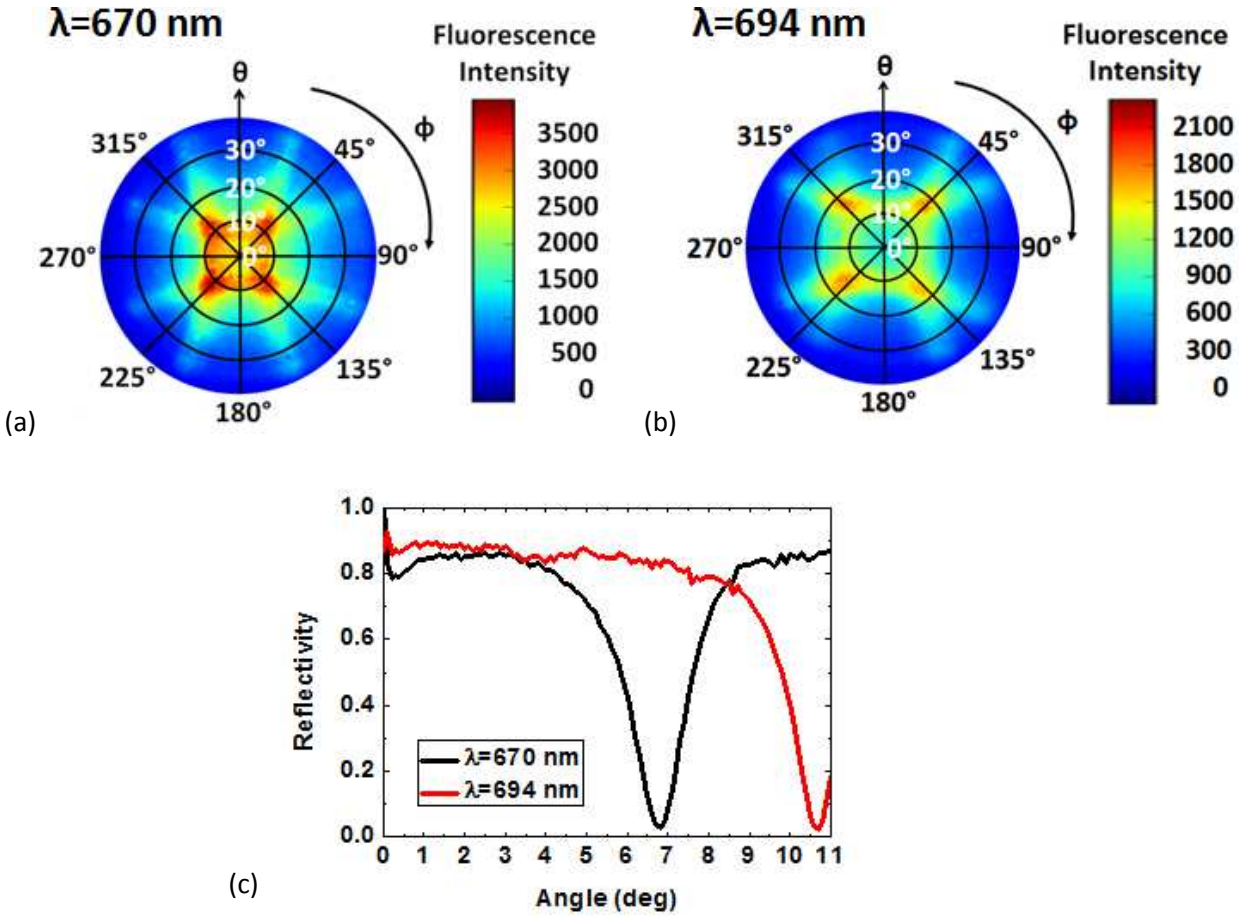

Figure 4.16 Measurements of angular fluorescence distribution at (a) λ_{em}=670 nm and (b) λ_{em}=694 nm. (c) Angle dependent reflectivity spectra of crossed grating at λ =670 nm and λ =694 nm.

4.5 Biosensor application – Interleukin 6 immunoassay

This chapter demonstrates an application of substrates that plasmonically enhance the fluorescence signal for immunoassay-based detection of molecular analytes. In particular, the implementation of crossed diffraction gratings supporting SPPs for readout with optical systems that are compatible with regular microarray fluorescence scanners was pursued. In order to evaluate how the fluorescence enhancement factor *EF* translates to the assay performance characteristics such as limit of detection, an optical system was developed that allows for fluorescence kinteics measurements for studying molecular binding events on the metal surface. Series of measurements were carried out in collaboration with XXXXXX XXXXXX from AIT (Austrian Institute of Technology). In these joint experiment, structured and reference substrates with a biointerface architecture based on thiol self-assembled monolayer were used and assay for detection of inflammation biomarker IL-6 developed.

4.5.1 Biosensor optical system

An optical system that functions similar to microarray scanners and that is depicted in Figure 4.17 was developed. A beam from a HeNe-laser operating at wavelength λ=632.8 nm was used for the excitation of fluorophore labels. The beam passes through two polarizers, followed by a narrow band pass filter (FL632.8-10 from Thorlabs) which blocks light at wavelength different from 632.8 nm. The polarizers in combination with neutral density filters (1 % and 10 %) were used to attenuate the excitation beam intensity to reduce the fluorescence bleaching. Afterwards, the beam is reflected by a dichroic mirror (XF2087 660DRLP from Omega Optical) which is reflecting the laser and hits the sensor gold surface at normal incidence. Against the surface of either flat or structured substrates that are modified with capture antibodies, a flow-cell is clamped in order to contain liquid samples. The flow cell exhibited volume of 1.5 µL and consisted of a thin PDMS gasket and a transparent fused silica cover glass with drilled inlet and outlet ports. The fluorescence emitted from the sensor surface passes through the dichroic mirror that is transparent at the angle of 45 deg to the wavelength of λ_{em}=670 nm and collected by a lens (focal length *f*=50 mm and numerical aperture of *NA*=0.2, LB1471 from Thorlabs). In order to suppress the effect of partially reflected beam at the excitation wavelength of λ_{ex}=632.8 nm, a spatial filter was placed before the collecting lens. The spatial filter was made from a glass slide where a central small circular area was covered with black tape. The dimension of the tape is chosen in a way, that it exactly blocks the narrow laser beam. Let us note that in this small region, also the fluorescence is blocked. As the sample surface is exactly placed in the focal length of the collection lens, the fluorescence light is collimated by this lens. The collimated

fluorescence beam further passes a notch filter (XNF-632.8-25.0M from CVI Melles Griot) which blocks the excitation wavelength λ_{ex}. Then, the light propagates through two band-pass filters (FB670-10 from Thorlabs and 670FS10-25 from Andover Corporation Optical Filter) that are transmissive at the emission wavelength λ_{em}=670 nm. Finally, the fluorescence light is focused at the input of a photomultiplier (H6240-01, Hamamatsu). The photomultiplier is connected to a counter and the fluorescence signal is recorded in unit of counts per second (cps) by using a software Wasplas developed at Max Planck Institute for Polymer Research in Mainz (Germany).

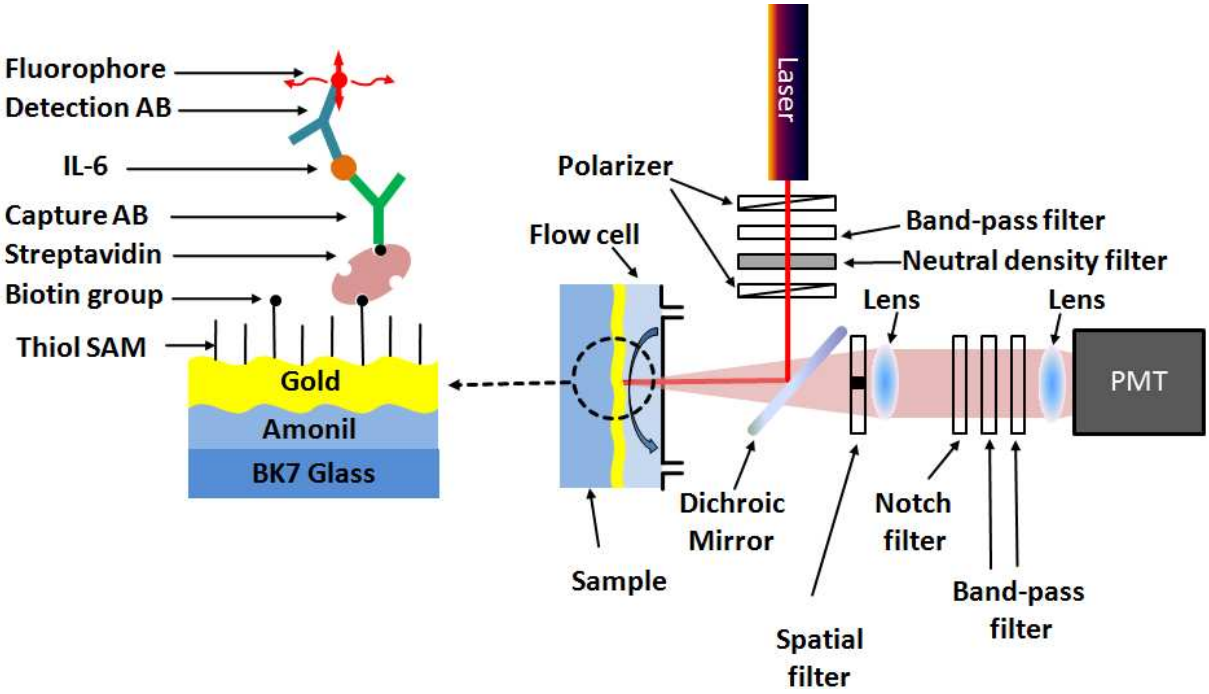

Figure 4.17 Sketch of the measurement setup for detection of fluorescence signal. The inset shows the assay used for detection of IL-6 in the experiments.

4.5.2 Modification of sensor chips

Firstly, evaporated gold film deposited either on flat (reference) glass surface or on the structured surface was modified by self-assembled monolayer (SAM) of mixed thiols. These surfaces were left overnight in ethanolic solution of thiols carrying functional biotin and passivating hydroxyl groups dissolved at a molar ratio of 1:4. The biotinylated PEG alkane thiol ($C_{33}H_{63}N_3O_8S_2$, molecular weight of 694 g/mol) was purchased from SensoPath Technologies and triethylene glycol mono-11-mercaptoundecyl ether ($C_{17}H_{36}O_4S$, molecular weight of 336.5 g/mol) was obtained from Sigma Aldrich. After reacting overnight, the samples were removed from the thiol solution, the surface was extensively rinsed with ethanol and dried with an air stream. Afterwards, the biotin groups were reacted with streptavidin (SA) (52.8 kDa, from Carl Roth GmbH+Co. KG) followed by the affinity

binding of capture antibody with biotin tag. The biotinylated capture antibody (c-Ab) (Anti-Human IL-6 Biotin, 13-7068 from eBioscience) was against human interleukin 6. The surface mass density of SA and biotin-tagged c-Ab was measured by surface plasmon resonance with Kretschmann configuration. These measurements were performed on reference flat substrates that were coated with only 50 nm of gold. The SPR measured kinetics for a surface modified with thiol SAM, after the binding of SA and after the reaction of biotin-tagged c-Ab are presented in Figure 4.18. The change of reflectivity in the kinetics measurement is calibrated by spiking PBS with 2 Vol.-% of ethylene glycol and taking the tabulated values of the refractive index unit (RIU) change [77]. The RIU shift due to the binding of SA is $\delta n_b = 0.00548$ RIU which corresponds to the streptavidin surface mass density of Γ_{SA}=2.8 ng/mm². The subsequent binding of c-Ab shifted the RIU by $\delta n_b = 0.0029$ RIU which translates to surface mass density of Γ_{c-AB}=1.5 ng/mm². This value is similar to previously reported values for IgG bound to gold surface [77].

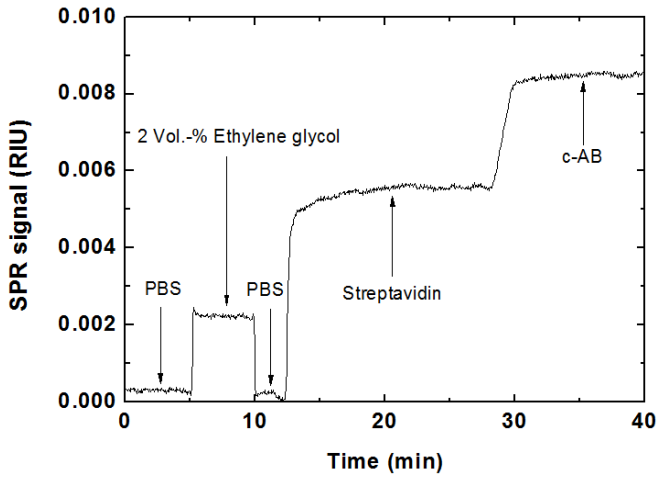

Figure 4.18 SPR kinetics of modification of Au surface with a thiol SAM followed by affinity binding of streptavidin and an IL-6 antibody [Data kindly provided by XXXXXX XXXXXX (AIT-Austrian Institute of Technology)].

Let us note, that the modification of the gold surface with protein is associated with a shift of SPR not only in angular spectrum (as shown for ATR coupling in Figure 4.18), but also in the wavelength spectrum for the grating-coupling. The modification of the surface with SA and c-Ab shifts the SPR from initially λ=631.2 nm to λ=632.5 nm, which is not very significant.

4.5.3 Assay development

Over the sensor surface with clamped flow-cell, liquid samples were flowed with a flow-rate of $15\ \mu L/min$. All experiments were performed in a phosphate buffered saline (PBS) with 0.05 Vol.-% Tween 20 (PBST). Prior to the experiment, the sensor surface was in situ functionalized by using the same flow-cell as in previous SPR studies. Firstly, SA was immobilized on biotin moieties of thiol SAM upon a 10 min flow of a solution with SA dissolved at 50 µg/mL in PBST. Afterwards the c-Ab was immobilized from a solution with c-Ab dissolved at 5 µg/mL.

For the detection of the target analyte (human interleukin 6 (IL-6)), a sandwich immunoassay was used. In this assay, the fluorescence signal was measured in real time and firstly a baseline was established. Then samples with concentrations of IL-6 between 4.3 and 43 nM was flowed through the sensor for 10 min followed by 5 min rinsing with PBST. Then, detection antibody (d-Ab) against another epitope of IL-6 that was labeled with fluorophores allowed to bind to the IL-6 analyte captured on the surface. The d-Ab was dissolved in PBST solution at the concentration of 100 µg/mL and flowed for 10 min. Finally, the sensor surface was rinsed again with PBST for 5 min and the difference in the fluorescence signal ΔF before and after the assay cycle was measured. Samples were prepared by spiking PBST with known concentration of IL-6. In this model experiment, affinity purified recombinant protein carrier-free human IL-6 was used (34-8069 from eBioscience). As a detection antibody, monoclonal anti-human IL-6 that was affinity purified and obtained from eBioscience, was used. Capture and detection antibody have been purchased as a monoclonal antibody pair which has been tested for the detection of human IL-6. The detection antibody was labeled using the Alexa Fluor 647 Protein Labeling Kit (A20173) from Molecular Probes / Invitrogen.

The assay characteristics were first investigated on the structured surfaces that provided the plasmonically amplified fluorescence signal from molecules attached to the surface. To determine the unspecific adsorption of dye labeled d-Ab, the d-Ab was injected in the flow-cell prior to the sample containing target IL-6 analyte. The difference in fluorescence signal before d-Ab injection (see Figure 4.19 (a) at t=40 min) and after rinsing with PBST (see Figure 4.19 (a) at t=55 min) was $\Delta F = 2.1 \times 10^3\ cps$. In addition, one can see that upon the flow of a solution with dissolved d-Ab, the fluorescence signal increases (abrupt increase and decrease of the response when d-Ab was injected and rinsing was started at time *t*=40 min and 50 min, respectively) by about $8.2 \times 10^3\ cps$. This increase in signal occurs due to the excitation of fluorophores present in the bulk solution passing through the flow-cell. Afterwards, PBST with the concentration of IL-6 of 4.3 nM and 43 nM were analyzed (time of injection of sample at t=60 min and t=90 min, respectively). The obtained kinetics measurement reveal much stronger fluorescence increases of $\Delta F = 2.9 \times 10^4\ cps$ and $\Delta F = 2.8 \times 10^5\ cps$ due to the specific affinity binding of d-Ab to captured IL-6. The approximately

10 fold higher fluorescence signal ΔF was measured when in increasing the IL-6 concentration by the same factor which indicates that the affinity binding of IL-6 to c-Ab is far from saturation and that the response scales linear with the IL-6 concentration.

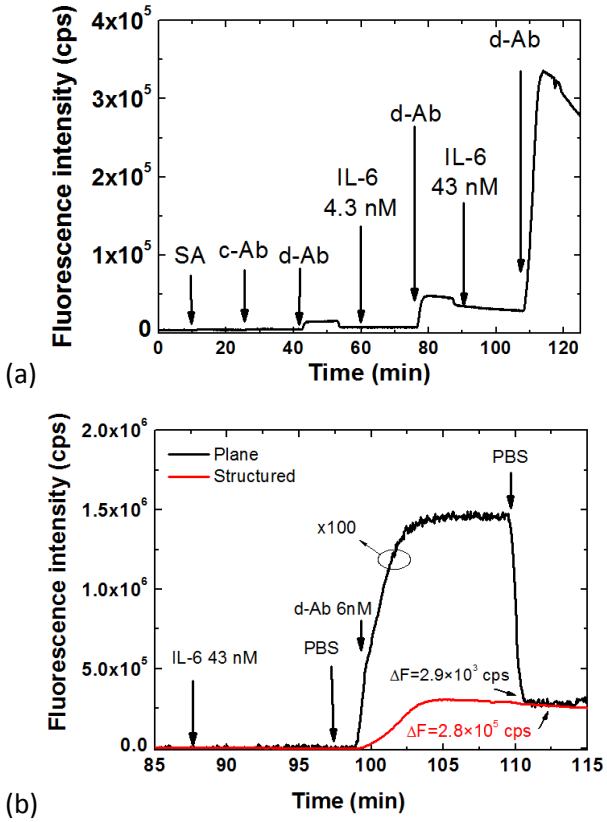

Figure 4.19 (a) Kinetics of IL-6 assay on crossed sinusoidal grating. The abbreviation SA states for streptavidin, c-Ab for capture antibody, and d-Ab for detection antibody. (b) Comparison of fluorescence signal from reference flat gold surface (black) and crossed gold grating (red) for the cycle when a sample with IL-6 concentration of 43 nM was analyzed. Fluorescence signal of flat reference structure is multiplied by a factor of 100 [Data acquisition kindly supported by XXXXXX XXXXXX (AIT-Austrian Institute of Technology)] (graphics adapted from [145]).

To investigate the effect of plasmonic amplification of the crossed grating structure, the performance was compared to a flat gold surface. A fluorescence kinetics measurement on a flat gold surface was performed with identical assay parameters where a sample with IL-6 concentration of 43 nM was analyzed. Figure 4.19 (b) compares the fluorescence kinetics measured on the flat gold surface (black curve multiplied by a factor of 100) with that on the gold grating. The sensor response due to the affinity binding of IL-6 and d-Ab before the injection (t=85 min) and after the rinsing (t=115 min) is $\Delta F = 2.9 \times 10^3\ cps$. This value is 96 times lower than on the structured surface. Let us note that the about 10^2-fold enhancement due to the structuring of the gold surface agrees well with the previous simulations and experiments presented in sections 4.3 and 4.4. The simulations were

carried out for the distance $f = 15 - 20\,nm$ between fluorophore and the Au surface. In the presented assay experiment, the distance between gold surface and fluorophore can be estimated at around $f \approx 20\,nm$ [67].

In addition, it should be noted that the selective amplification of the fluorescence signal originating from the grating surface allows for strongly reduced (relative) signal originating from the fluorescence signal of the bulk solution. This enables for more accurate fluorescence measurements of kinetics of affinity reaction that is otherwise masked by the strong bulk background signal (compare the red and black curves in Figure 4.19 (b)). The fluorescence signal of the bulk solution originates from the excitation beam that passes through the solution with dissolved fluorescence-labeled molecules.

4.6 Summary

A periodic gold grating structure that allows for coupling of incident light to SPP modes was investigated in order to amplify fluorescence signal of immunoassays in epifluorescence geometry. Numerical simulations and experiments have been carried out in order to optimize metallic surface corrugation (that was decomposed to a superposition of crossed sinusoidal modulations) to maximize the fluorescence intensity enhancement.

The structure identified by FDTD simulations was prepared by laser interference lithography. In addition nanoimprint lithography was adopted for the preparation of multiple identical copies of the structure. In order to demonstrate the ability of fluorescence signal amplification, experiments with organic fluorophores (DID) dispersed in a polymer film on the structure as well as an immunoassay was characterized.

The simulations and experiments were in excellent agreement and showed that for fluorophores emitting at around λ_{em}=670 nm, an enhancement factor of $EF \sim 10^2$ is provided by designed crossed gold grating structure when compared to a reference sample with a flat gold surface. This enhancement mainly originates from improved collection efficiency CE that was enabled by SPP-coupled directional emission (contributes to EF by a factor of ~4 compared to flat gold surface) and by locally amplified strength of the excitation field at proximity to fluorophore at λ_{ab} (factor of ~30 compared to flat Au surface). The change of the intrinsic quantum efficiency for studied fluorophores Cy5 and Alexa Fluor 647 with $\eta_0 \sim 0.3$ is of minor importance.

The achieved magnitude of *EF* for Au gratings is similar to highest reported values for Ag gratings with SiO_2 overlayer [129]. However, let us note that in their work, a glass substrate was used as a reference system, which gives about twice lower signal than herein used flat gold substrate [84].

Therefore, the herein reported values should be renormalized by this factor in order to make them comparable.

The developed structures were successfully applied for sandwich immunoassay-based detection of interleukin 6 (IL-6). The predicted and experimentally demonstrated enhancement factor of $EF \sim 10^2$ translates to improved signal-to-noise ratio in fluorescence signal due to the capture of target analyte on the surface. Besides the ability to detect smaller amounts of IL-6 analyte compared to flat gold surfaces, the amplification confined at the proximity to metallic surface offers the advantage of suppressing the effect of background signal from the bulk solution. This feature is attractive for the observation of molecular binding kinetics that are otherwise masked by strong signal associated with the excitation of fluorophores dispersed in the solution (through which the excitation beam passes).

The developed crossed grating holds potential for application in a range of devices such as fluorescence microscopes and fluorescence scanners for microarrays. The crossed gratings may provide improved accuracy of these technologies in terms of limit of detection as well as for simplified optical systems.

5 Fluorescence biosensing with nanoparticle arrays supporting cLSPs

5.1 Introduction

In the previous chapter it has been shown, that the fluorescence signal can be strongly enhanced for fluorophores in proximity of a grating supporting SPPs. In this section, metallic nanoparticles will be used for additionally confine the electric field intensity close to the nanoparticle surface and therefore further increase the excitation rate of the fluorophore. Nanoparticles exhibit tremendously different optical properties when arranged into arrays. For small periods, the nanoparticles near-field couple and form gap modes, while for larger distance the particles can couple diffractively.

Collective localized surface plasmons (cLSPs) are based on the diffractive coupling of neighboring nanoparticles and their localized surface plasmon resonance [97, 147]. The coupling results in sharp resonances and high electric field intensity enhancements [99, 148]. Nevertheless, for the application of such modes, the nanoparticles need to be embedded in a refractive index symmetric environment [98]. The potential use of such a system for plasmon enhanced fluorescence has been shown for fluorophores embedded in a polyvinyl butyral matrix (n=1.48) close to rod shaped nanoparticles which are placed on a glass substrate (n=1.52) [149]. Thus, the system have been in a refractive index symmetry of $n \approx 1.5$.

For the use of these modes for detection of analytes in aqueous solution, the particles need to be placed in refractive index symmetry similar to water (n=1.33). Due to the narrow resonances of cLSPs, it is difficult to make them overlap simultaneously with the absorption and emission band of the used fluorophore. Therefore the structure will be designed to show two resonances in epifluorescence geometry, one close to the absorption wavelength λ_{ab} and one at maximum emission λ_{em} of the considered fluorophore. While the resonance at λ_{ab} is expected to increase the excitation rate of an emitter, the resonance at λ_{em} is expected to support directional emission of fluorescence light preferentially normal to the structure surface and thus allows for efficient collection of fluorescence light.

The goal of this section is the theoretical prediction of the enhancement factor of such a system for typical distances in immunoassays and the practical realization of a structure supporting cLSPs in aqueous environment. The enhancement abilities of the LSP structure will be compared to conventional substrates used in immunoassay applications.

5.2 Investigated geometry

The structures under study are presented in Figure 5.1. The main focus in this chapter is on the structure shown in Figure 5.1 (a) which supports cLSPs. The structure consist of a 2D rectangular array of gold nanoparticles with period Λ =460 nm, diameter D=110 nm and height h=50 nm on a low refractive index polymer spacer (n=1.33) with thickness d_b=120 nm in aqueous environment. In practice the low refractive index polymer can be Teflon (n=1.32) or Cytop (n=1.34) as commercial available possibilities. In appropriate distance below the array is a thick silver mirror. The inset in Figure 5.1 (a) shows the possible immobilization of a fluorophore to the gold disk surface by an immunoassay. The final determined enhancement factor EF of the cLSP structure will be compared to a couple of reference structures.

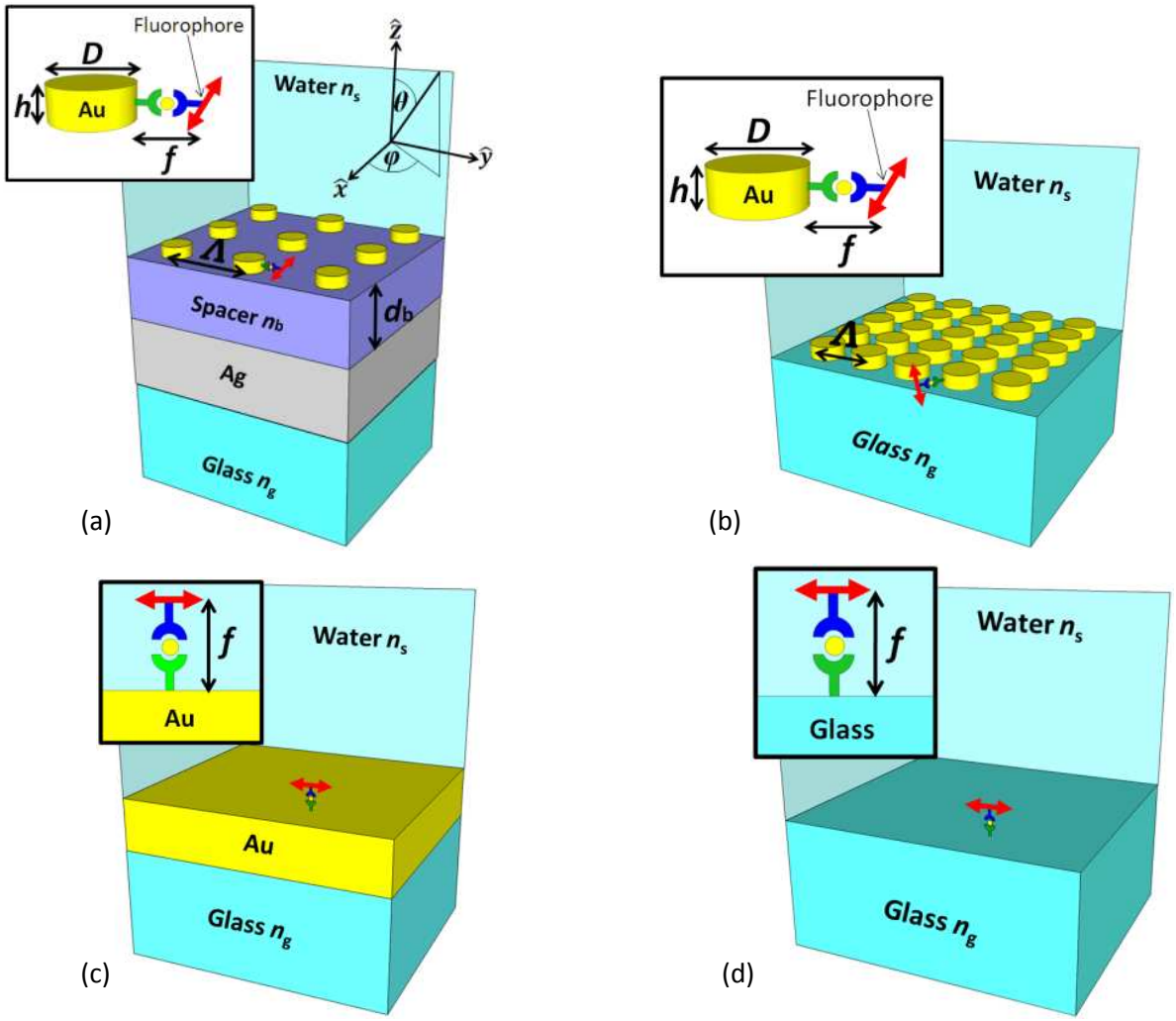

Figure 5.1 (a) cLSP structure and reference structures (b) dense gold nanodisk array on glass substrate (c) optically thick flat gold film and (d) flat glass substrate. The inset shows an immunoassay bound to the surface at distance f with capture antibody (green), analyte (yellow), detection antibody (blue) and a fluorophore (red double arrow) (graphics from [84]).

The reference structure shown in Figure 5.1 (b) is a dense particle array with same disk dimensions as in Figure 5.1 (a) but with lower period of $\Lambda = 200\ nm$ and on a glass substrate. A similar structure has been used for plasmon-enhanced fluorescence [117] and thus is a good comparison for the performance achieved by the cLSP structure. The easiest and commonly used structures as reference systems are flat optically thick gold films (see Figure 5.1 (c)) and flat glass substrates (Figure 5.1 (d)). In all figures, the inset shows a model immunoassay with a capture antibody (green) bound to a solid support, an analyte (yellow) that is captured to this biorecognition element and finally a detection antibody (blue) with a fluorophore label (red). The distance f denotes the distance between the structure surface and the fluorophore which is usually at around $f \approx 20\ nm$ [67].

5.3 Simulations

The main part of the simulation results presented in this section have been published in an article authored by Martin Bauch and Jakub Dostalek "Collective localized surface plasmons for high performance fluorescence biosensing" [84].

For the simulation of the reflectivity and the electric near-field distribution of the cLSP structure optical constants for gold and for silver are taken from literature [24]. Refractive index of water was taken as a constant, n=1.33, and the refractive index of the low refractive polymer (Cytop n=1.337), was chosen in simulations for simplicity as n=1.33. Electric field intensity enhancement, transmission and reflectivity spectra were calculated with a single unit cell. Periodic boundary conditions were applied in plus and minus x-direction and plus and minus y-direction with period Λ =460 nm. Below the silver mirror (minus z-direction), perfect metallic conductor was chosen as a boundary condition and in plus z-direction well above the particle array, a perfectly matched layer (PML) was applied. A uniform mesh of 1 nm was chosen.

As already explained in section 3.1.4 for simulation of a fluorophore in proximity to a periodic structure, one can not only model one unit cell of the structure with one dipole with periodic boundaries. Therefore one has to simulate a sufficiently big area of a periodic structure with one dipole current source (representing the fluorophore) in the center. The chosen size of the structure has to be checked for convergence. The convergence for the cLSP structure has been verified in quantum efficiency and far-field emission pattern and determined to be 41 periods by 41 periods of gold nanodisks as sufficient size. PMLs were placed in plus and minus, x- and y-directions, as well as in the plus z-direction. Below the optical thick (300 nm) silver mirror, perfect electric conductor was used as boundary condition. The emission wavelength of the dipole was chosen to be $\lambda_{em} =$

$663\ nm$. The center particle including the dipole source was modeled with a maximum mesh size of 2.5 nm, while the rest of the structure was modeled with a maximum of 5nm.

For calculating the enhancement factor (EF) defined in Eq.(3.13) and Eq. (3.14) and the average far-field fluorescence emission, 8 positions have been defined around one central disk in an array of 41 by 41 disks. The positions are at half the height of the nanoparticle and $f = 20\ nm$ away from the gold surface (see Figure 5.2).

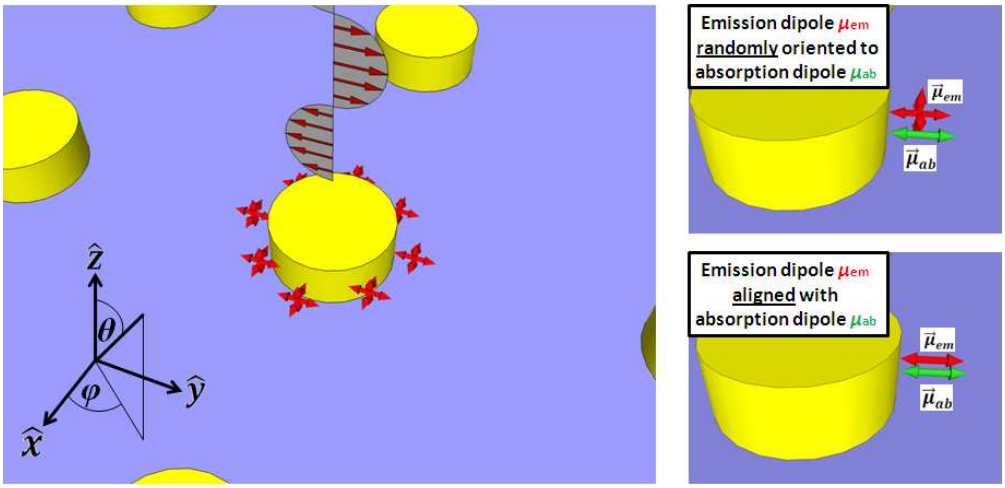

Figure 5.2 Schematic of the array of gold disks shows at which positions the interaction of a fluorophore with the gold disk array is considered (left). In addition two cases are considered for (1) emission and absorption dipole randomly oriented and (2) emission and absorption dipole aligned (right).

Though not explicitly shown here, the same positions around the gold disks are taken for the dense particle array. As the flat gold and glass surface are invariant in the x- and y-direction, the fluorescence emission needs to be calculated at one position only.

5.3.1 Spectrum of modes and near-field characteristics

An essential building block of the cLSP structure is a gold nanodisk. First, an isolated disk with same dimensions as in the cLSP structure in an aqueous environment is considered. The absorption Q_{abs}, scattering Q_{sca} and extinction coefficients Q_{ext} are shown in Figure 5.3, as well as the electric field enhancement at 20 nm distance from the surface. The broad localized surface plasmon resonance (LSPR) of the extinction coefficient peaks at around $\lambda_{LSPR} = 650\ nm$ and the electric field intensity at around $\lambda = 670\ nm$. Highest field enhancements of $|E|^2/|E_0|^2 \approx 18$ are achieved.

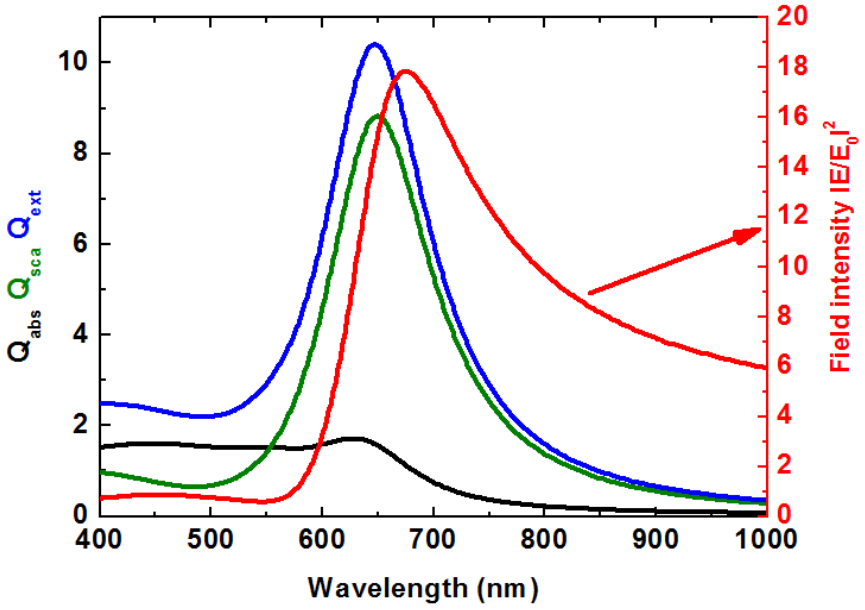

Figure 5.3 Spectra of isolated gold disk with diameter D=110 nm and height h=50 nm in water (n=1.33) with absorption coefficient Q_{abs}, scattering coefficient Q_{sca} and extinction coefficient Q_{ext}. The electric field intensity is given at distance 20 nm away from gold surface.

The reflectivity and field intensity spectra of the cLSP structure are shown in Figure 5.4. Two resonances can be seen manifested as dips in the reflectivity spectra. The first resonance occurs at $\lambda_{ab} = 634\,nm$ and can be used to efficiently excite the fluorophore. The second resonance at $\lambda_{em} = 663\,nm$ is designed for efficient emission of fluorescence light. Both resonances have different origins and in the following, the origin of both will be explained. The resonance at emission wavelength $\lambda_{em} = 663\,nm$ is due to coupled localized surface plasmons (cLSPs) and is also present without a silver mirror below the structure (see transmission spectra in Figure 5.5). An incident plane wave induces in-plane dipole moments in the gold nanodisks due to charge separation in the nanoparticles. These dipoles scatter light itself which is collected by the neighboring gold nanodisks. If the period between the particles is chosen appropriate, the LSP can be phase matched. By this process the disks are diffractively coupled without any near-field interaction of the disks between each other.

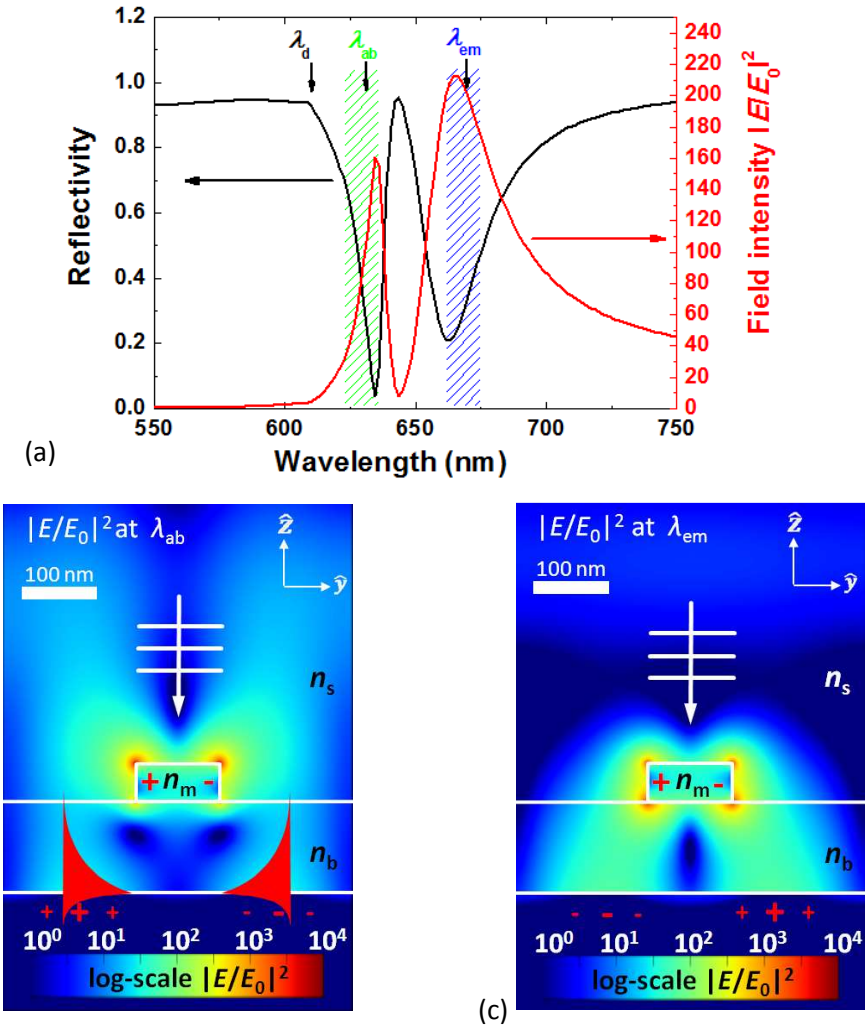

Figure 5.4 (a) Reflectivity spectra and electric field intensity for normal incident light. The electric field intensity was calculated for a point with distance of f=20 nm from the surface and along the polarization axis of the incident light. Near-field distribution with log-scale at (b) $\lambda_{ab} = 634\ nm$ and (c) $\lambda_{em} = 663\ nm$. The electric charge distribution is depicted with red plus and minus signs (graphics from [84]).

The phenomena of cLSP is efficient to trap light within the particle plane and therefore the light propagates longer within the structure, resulting in sharp resonances and high field intensity enhancements [97, 99, 150]. The resonance width of the cLSP mode is around $\Delta\lambda$ =25 nm. Let us note that for non-normal incident TM polarized light, even out-of-plane dipole moments can couple and lead to sharp resonances [100]. The resonance position is dependent on the individual particle localized surface plasmon resonance (LSPR), the period Λ of the array and the refractive index of the surrounding medium. Efficient coupling between the particles is achieved when the substrate and the material above have similar refractive index. Therefore, to fulfill this requirement, a low refractive index polymer with refractive index n_b as a spacer layer was chosen, with almost the same refractive index as water. Asymmetric refractive index configurations are possible as well, however, the existence of the cLSP resonance is dependent on the particle size and position of the diffraction

edge [98]. The position of the diffraction edge is determined by the period Λ and the refractive index of the substrate n_b and the superstrate n_s. For normal incident light, the equation for the position of the diffraction edge at a certain diffraction order (i, j) is given as [25, 99, 149]:

$$\lambda_{(i,j)} = \frac{\Lambda \cdot n}{\sqrt{(i^2 + j^2)}} \tag{5.1}$$

The diffraction edge is denoted in Figure 5.4 (a) as λ_d. In the case of the presented structure, the refractive index of substrate and superstrate is the same and a first order diffraction edge is observed at $\lambda_{(1,0)} = 612\, nm$.

The silver mirror below the disk array gives rise to the excitation of surface plasmon polaritons (SPPs). The excitation of the SPPs is possible due to the additional momentum provided by the grating vector of the 2D disk array. The dispersion relation of a 2D grating is derived in section 1.2.2 and the wavelength λ at which the resonance occurs is given by [151]:

$$\lambda_{(i,j)} = \frac{\Lambda}{\sqrt{(i^2 + j^2)}} \sqrt{\frac{\varepsilon_d \varepsilon'_m}{\varepsilon_d + \varepsilon'_m}} \tag{5.2}$$

with ε_d dielectric function of the material above the metal film, in this study the low refractive index polymer, i and j the diffraction orders and ε'_m the real part of the dielectric function of the metal, which is in our case silver. The resonance wavelength for $(i = 1, j = 0)$ calculated with Eq.(5.2) is $\lambda_{(i=1,j=0)}$=644 nm. This wavelength is 10 nm higher than the one observed in Figure 5.4 (a). This discrepancy can be explained by the interaction/coupling between the SPP mode and the cLSP mode and the reported anti crossing behavior [152, 153].

The spectral dependence of electric field intensity 20 nm away from the gold disk seen in Figure 5.4 (a) shows two peaks at the two resonances explained before. The field intensity at λ_{ab} is $|E|^2/|E_0|^2 \approx 160$ and at λ_{em} $|E|^2/|E_0|^2 \approx 210$, which is more than ten times bigger than for an isolated nanodisk with same dimensions (see Figure 5.3). Let us note that the spatial averaged electric field intensity around the gold disk surface is $\langle |E|^2/|E_0|^2 \rangle = 90$ for a distance of 20 nm at λ_{ab}.

In Figure 5.4(b) and (c) the near-field distributions for the resonances at $\lambda_{ab} = 634\, nm$ and $\lambda_{em} = 663\, nm$ are given respectively. It can be seen that at the surface of the disk, high electric fields intensities well above $|E|^2/|E_0|^2 > 1000$ are achieved. Particularly high enhancements can be observed at the edges of the nanodisk. In addition, the electric charge distribution is shown by red plus and minus signs. Both near-field distributions show that the electric field is highly confined to

the surface of the nanodisks. At λ_{ab} the exponential decaying field of the SPP from the flat silver surface is confined at the surface of the nanodisks. The charge distributions at λ_{em} of the nanodisk and the silver metal surface have opposed signs indicating the induction of image (mirror) charges in the metal surface [152, 154, 155].

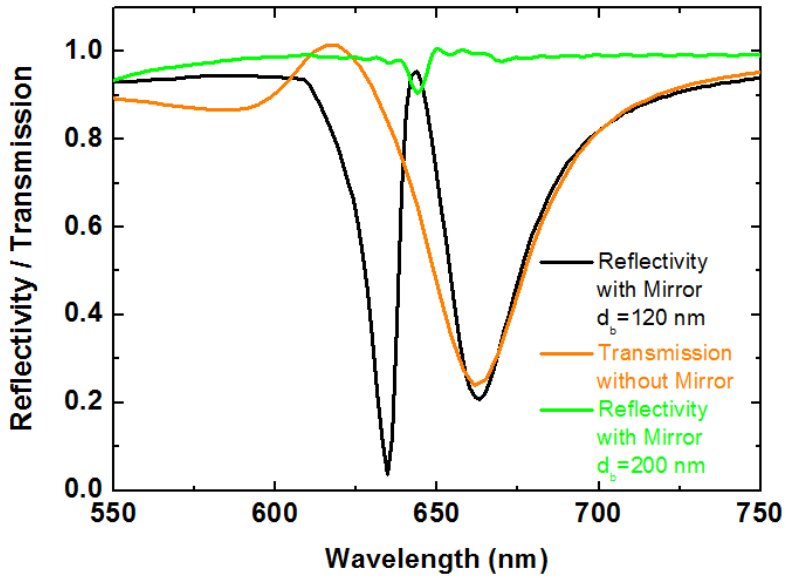

Figure 5.5 Effect of spacer thickness d_b on reflectivity and transmission spectra without silver mirror below the array at normal incident light.

A crucial design criteria for the cLSP structure with thick silver mirror below is the thickness of the polymer spacer d_b, as it defines the distance between the gold disks and the silver. To achieve efficient coupling and high field intensity, the light incident on the structure and the light reflected by the silver mirror need to be in phase to constructively interfere. Figure 5.5 shows one example of constructive interference for spacer thickness of d_b=120 nm and one example of destructive interference for spacer thickness of d_b=200 nm. For the d_b=200 nm spacer case, both resonances are almost completely suppressed. The condition of constructive interference for normal incident light on a metal that behaves as perfect conductor or dielectric (with bigger refractive index than of the medium where the light comes from) is given as [156]:

$$d_b = \frac{\lambda_0}{n_d}\frac{(2k+1)}{4} \qquad (5.3)$$

where $k = 0,1,2,\ldots$ is a positive integer and n_d is the refractive index of the spacer. Deviations of this equation can be found when the metal does not behave like a perfect metal [157, 158].

The spectral reflectivity and electric field intensity dependency as well as the near-field distribution at λ_{ab} for the dense particle array, the optically thick gold film and the flat glass substrate are shown in Figure 5.6.

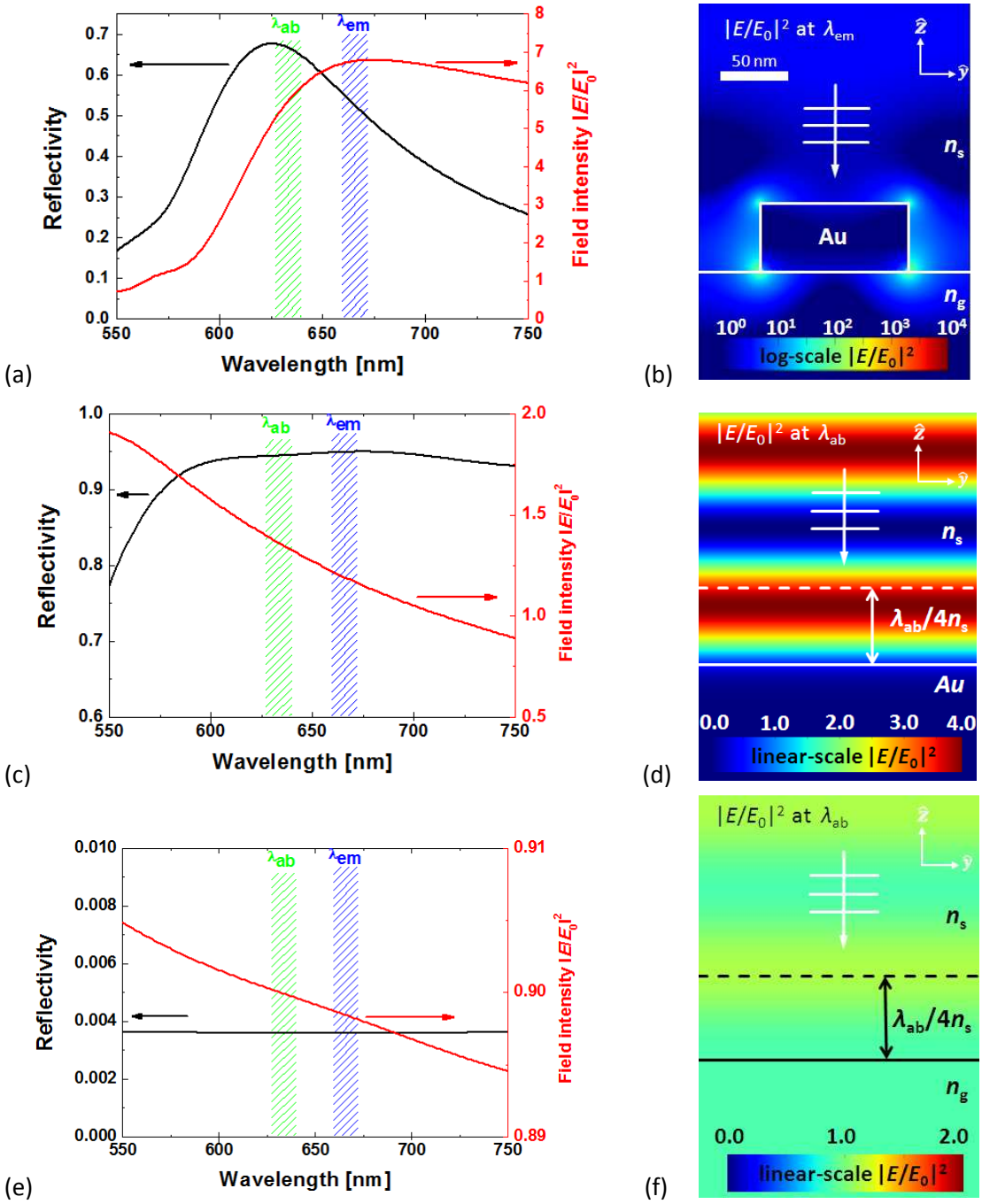

Figure 5.6 Spectral dependence of reflectivity and electric field intensity $|E/E_0|^2$ at distance 20 nm from surface (a) dense nanodisk array, (c) flat gold substrate, and (e) flat glass substrate. The near field distributions are given for the (b) dense particles array at λ_{em}=670 nm, while for the (d) flat gold and the (f) flat glass at λ_{em}=633 nm (graphics from [84]).

The reflectivity spectra of the dense particle array in Figure 5.6 (a) shows a broad resonance at 625 nm. The electric field intensity peaks at 675 nm and has a maximum value of $|E|^2/|E_0|^2 = 6.8$, which is more than twice less than for an isolated gold nanodisk the with same dimensions (see Figure 5.3). This can be understood when considering the surface coverage of the dense particle array compared to the total area, where 24 % of the area is filled with the particles. As we have seen in Figure 5.3, the extinction coefficient of an individual disk is bigger than Q_{ext}=10, which means that the particle can interact with light in a ten times bigger area than its actual cross-sectional area. In the case of the dense particle array, the nanodisks are too close to each other to make use of this potential and thus the electric field intensity decreases. In addition, the particles are too far away from each other to benefit from high intensity enhancements due to near-field interaction by gap modes. The averaged electric field intensity for the dense particle array is $\langle|E|^2/|E_0|^2\rangle = 2.6$ around the gold disk surface for a distance of 20 nm.

The reflectivity curve of the flat thick gold film in Figure 5.6 (c) shows high reflectivity above λ =600 nm of around 95% while below λ =600 nm it decreases rapidly, due to the optical properties of gold. The intensity enhancement at λ_{ab} is $|E|^2/|E_0|^2$ =1.36 at f=20 nm. In Figure 5.6 (d) the intensity near-field distribution is shown. It can be seen that when approaching the surface, intensity oscillates between $|E|^2/|E_0|^2 \approx 4$ and $|E|^2/|E_0|^2 = 0$ due to constructive and destructive interference.

The reflectivity curve of the flat glass (see Figure 5.6 (e)) is wavelength independent as the optical constant of glass and water have been set as constants in this wavelength range and intensity enhancement at λ_{ab} is with $|E|^2/|E_0|^2$ =0.9 slightly smaller than the intensity of the incident light $|E_0|^2$.

5.3.2 Metal-fluorophore interaction and fluorescence emission

The quantum efficiency and the far-field emission were calculated from an area of 41 by 41 periods. This square geometry is necessary, as the cLSPs propagating within the particle plane and the SPPs on the silver mirror propagate in orthogonal directions to each other. The SPPs propagate along the polarization of the incident light, while the cLSPs propagate perpendicular to the polarization of the light. The intrinsic quantum efficiencies of commercially available and widely used dyes such as Cy5 and AlexFluor647 in water are $\eta_0 = 0.28$ and $\eta_0 = 0.33$, respectively. For the following calculations, an intrinsic quantum efficiency of $\eta_0 = 0.30$ will be assumed when not differently stated.

The quantum efficiency in a system of a dipole and metallic nanostructure is dependent on the local density of optical states [137]. The spectral dependence of the change of intrinsic quantum efficiency η/η_0 of an emitter within the cLSP structure compared to an emitter close to an isolated

disk is shown in Figure 5.7. Both spectral dependencies are very similar. No sharp features like in the reflectivity curve of the cLSP structure (see Figure 5.4 (a)) are observed. The maximum quantum efficiency enhancement is achieved at λ =625 nm which is quite close to the maximum scattering coefficient Q_{sca} of an isolated disk (see Figure 5.3).

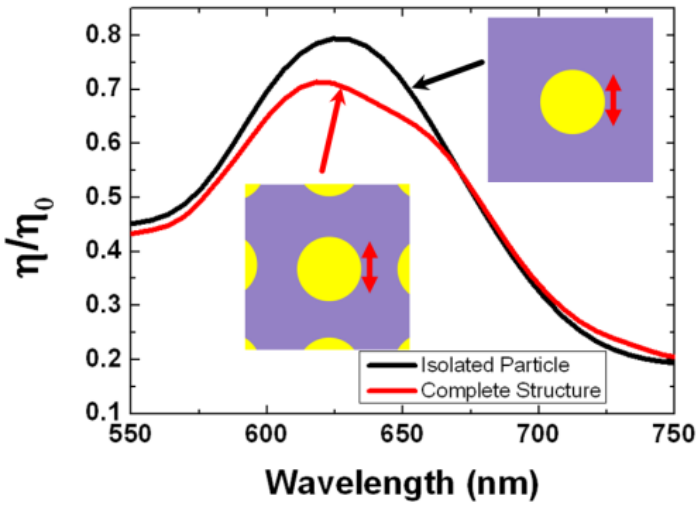

Figure 5.7 Wavelength dependency of quantum efficiency η/η^0 of an emitter close to an isolated disk and emitter in the cLSP structure for the depicted emitter orientation. The distance of the emitter to the gold surface is in both cases f=20 nm and the intrinsic quantum efficiency is $\eta_0 = 1.0$.

This is due to the fact that the dipole interacts with the local density of optical states of the disk close by, which determines the decay rates and thus the change of intrinsic quantum efficiency.

Figure 5.8 shows the emission rate enhancement $\gamma_e/\gamma_e^0 \times \eta/\eta_0$ for different distances f, which is the product of the excitation rate enhancement γ_e/γ_e^0 and the change of intrinsic quantum efficiency η/η_0. The emission rate is a measure of how many photons are emitted from a fluorophore, independent on the direction of the emission. While the excitation rate was obtained from the cLSP structure, which is related to the electric field intensity enhancement $|E|^2/|E_0|^2$ (by Eq. (1.18)), the change of intrinsic quantum efficiency was simulated from an isolated disk. This is a good approximation as it has been shown that the quantum efficiency from an isolated disk and the cLSP structure are very similar. The emission rate was calculated for $\eta_0 = 0.3$ under the assumption that the absorption dipole $\vec{\mu}_{ab}$ and the emission dipole $\vec{\mu}_{em}$ are aligned. It can be seen that the maximum emission rate is reached for a gold disk to fluorophore distance of $f = 10\,nm$. While the excitation rate is increasing for decreasing distances f, the quantum efficiency enhancement decreases for small distances f and thus the emission rate maximum is a balance between excitation rate and quantum efficiency.

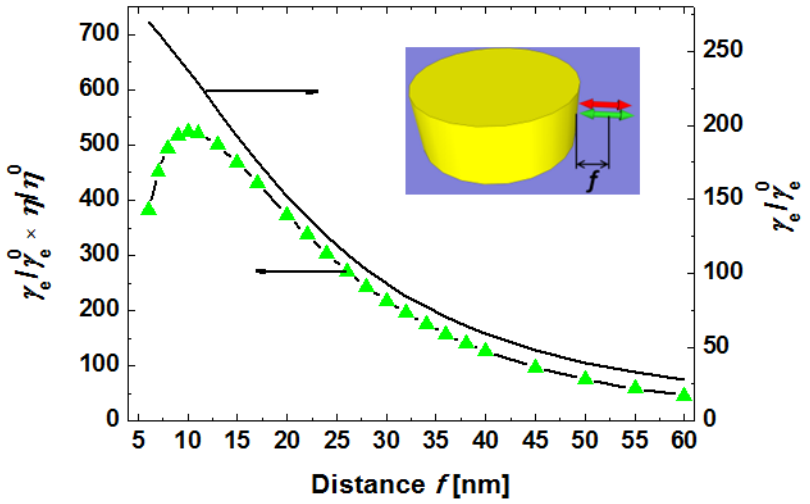

Figure 5.8 Distance f dependent emission rate enhancement $\gamma_e/\gamma_e^0 \times \eta/\eta_0$ and excition rate enhancement γ_e/γ_e^0. Inset shows the dipole orientation of absorption dipole $\vec{\mu}_{ab}$ (green arrow) and emission dipole $\vec{\mu}_{em}$ (red arrow). An intrinsic quantum efficiency of $\eta_0 = 0.3$ has been assumed (graphic from [84]).

The distance dependent quantum efficiency enhancement η/η_0 for different intrinsic quantum efficiencies η_0 is presented in Figure 5.9. While for intrinsic quantum efficiency of $\eta_0 = 1$, the quantum efficiency enhancement η/η_0 is always smaller than $\eta/\eta_0 < 1$, for intrinsic quantum efficiency of $\eta_0 = 0.3$, a factor of $\eta/\eta_0 = 2.5$ for quantum efficiency enhancement can be achieved at a distance of $f = 20\,nm$. For a low intrinsic quantum efficiency emitter a pronounced maxima with high enhancement of $\eta/\eta_0 = 12.4$ can be observed at a metal fluorophore distance of $f = 10\,nm$.

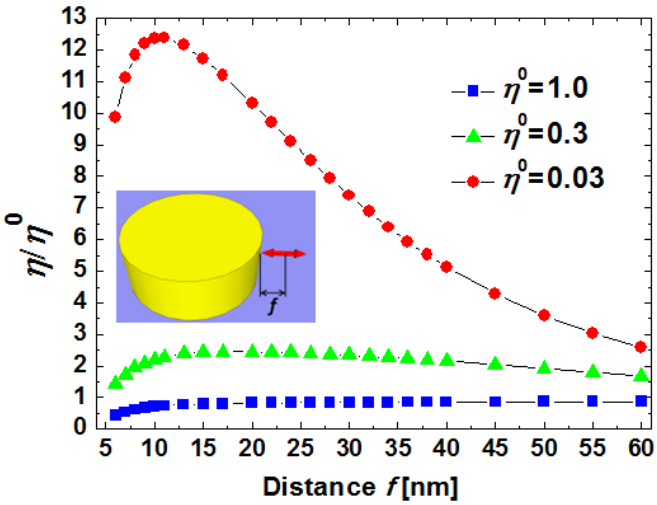

Figure 5.9 Distance f dependence of quantum efficiency enhancement η/η_0 for an isolated disk and intrinsic quantum efficiencies $\eta_0 = 1.0$, $\eta_0 = 0.3$ and $\eta_0 = 0.03$. The orientation of the emission dipole moment $\vec{\mu}_{em}$ is indicated by a red double arrow (graphic from [84]).

In Figure 5.10 the fluorescence emission to far-field of a fluorophore at f =20 nm distance from the nanoparticles surface is shown. The position and the orientation of the emission dipole moment $\vec{\mu}_{em}$ is indicated by a red double arrow. The fluorescence intensity $P(\theta, \varphi)$ is projectred to a half sphere above the cLSP structure, where the polar angle θ and azimuthal angle φ are shown. The maximum collection angle θ_{max} in water of a collection lens with NA=0.2 is shown. It can be seen that the highest fluorescence emission occurs in the range of the collection lens. This high directivity is a result of the cLSP outcoupling of the fluorescence light.

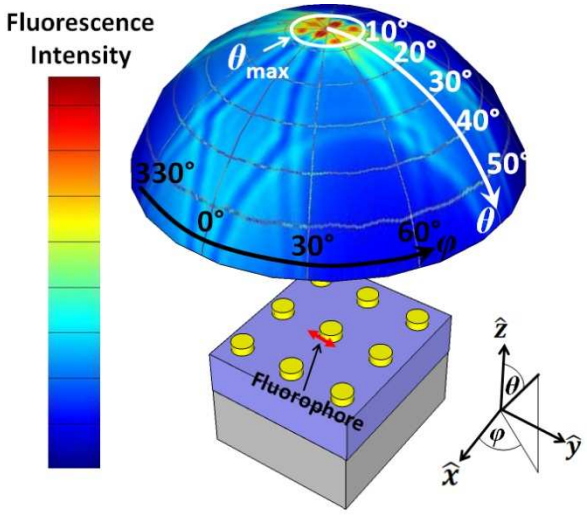

Figure 5.10 Far-field emission intensity at emission wavelength λ_{em}. The emission dipole $\vec{\mu}_{em}$ position and orientation (red double arrow) in the array, as well as the maximum collection angle θ_{max} are sketched for f=20 nm (graphic from [84]).

The cross section of the averaged fluorescence intensity $P(\theta, \varphi = 0)$ of the cLSP structure and the reference structures is shown in Figure 5.11. The average of the cLSP structure and the dense particle array is achieved by averaging the calculated far-field emission at all positions and orientations shown in Figure 5.2. The acceptance range of the collection lens (NA=0.2) is shown by black dotted lines and the fraction of total photons that is collected by the collection lens, also referred to as collection efficiency CE, is given by the red numbers. The calculation of the collection efficiency CE was performed with Eq.(1.25). Let us note that the collection efficiency values given in Figure 5.11 are calculated in 3D, though the graphics only show 2D cross sections. It can be seen in Figure 5.11 (a) that the cLSP structure directs the fluorescence light very efficiently into the range of the collection lens and no light is emitted into the substrate due to the thick silver mirror. The collection efficiency is CE=5.2%. The dense particle array (see Figure 5.11 (b)) shows no directional features and fluorescence light is emitted into the substrate and the water. The collection efficiency is only CE=0.9%. The flat thick gold film in Figure 5.11 (c) directs the fluorescence light exclusively into the water and shows a collection efficiency of CE=1.4 %. The fluorescence emission of a fluorophore

close to a flat glass substrate shows two pronounced emission lobes into the glass substrate (see Figure 5.11 (d)). This feature is referred to as supercritical angle fluorescence (SAF) [159, 160]. Most fluorescence light is emitted into the glass substrate and only a small fraction is collected by a lens above the glass substrate resulting in a collection efficiency of CE=0.5 %.

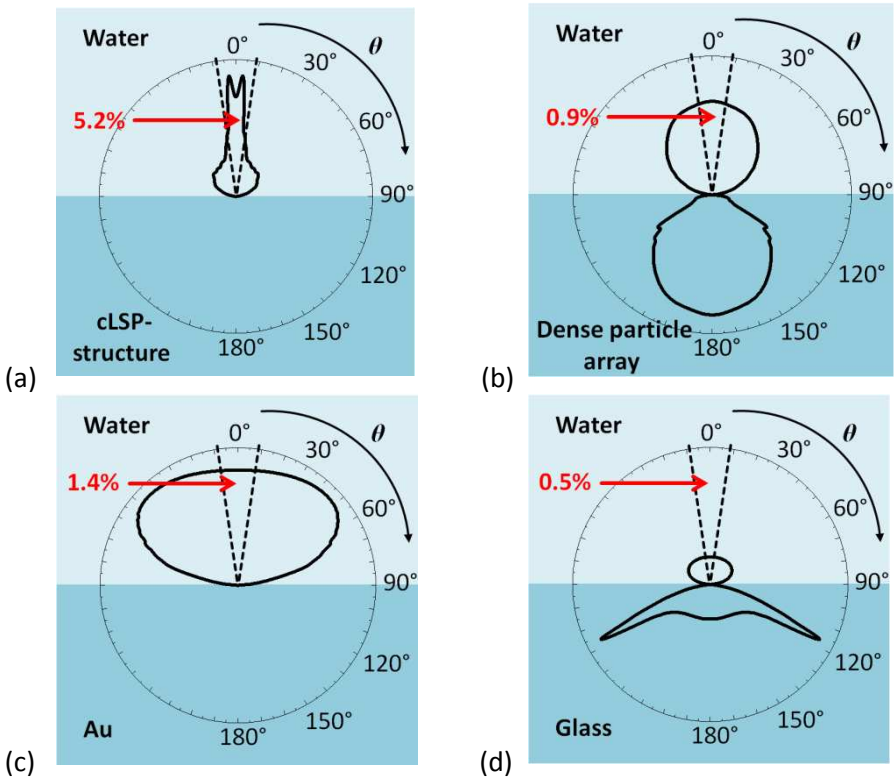

Figure 5.11 Cross section of averaged far-field emission $P(\theta, \varphi = 0)$ of (a) cLSP structure, (b) dense particle array, (c) flat gold and (d) flat glass substrate is shown. The collection range of lens with numerical aperture NA=0.2 is indicated by black dotted line. The collection efficiency CE is indicated by red numbers. (graphics from [84])

The cLSP structure in epifluorescence configuration allows collection of fluorescence light ten times more efficiently than a plane glass substrate and more than three times more than a flat thick gold substrate.

5.3.3 Amplification of fluorescence signal

The enhancement factor EF (introduced in section 3.1.6) defines by what factor the fluorescence signal of an emitter in proximity of a nanostructure is enhanced compared to an emitter in homogenous aqueous environment. The calculated enhancement factors EF for the structure supporting collective localized surface plasmons (cLSP), the flat glass substrate, the flat thick gold substrate and the dense particle array are tabulated in Figure 5.12. The enhancement factors were

calculated with Eq.(3.13) and Eq.(3.14) for three different intrinsic quantum efficiencies η_0 and a fluorophore to surface distance of f=20 nm. In addition, the two cases of (1) random orientation of emission dipole $\vec{\mu}_{em}$ to absorption dipole $\vec{\mu}_{ab}$ and (2) emission dipole $\vec{\mu}_{em}$ aligned to absorption dipole $\vec{\mu}_{ab}$ are considered.

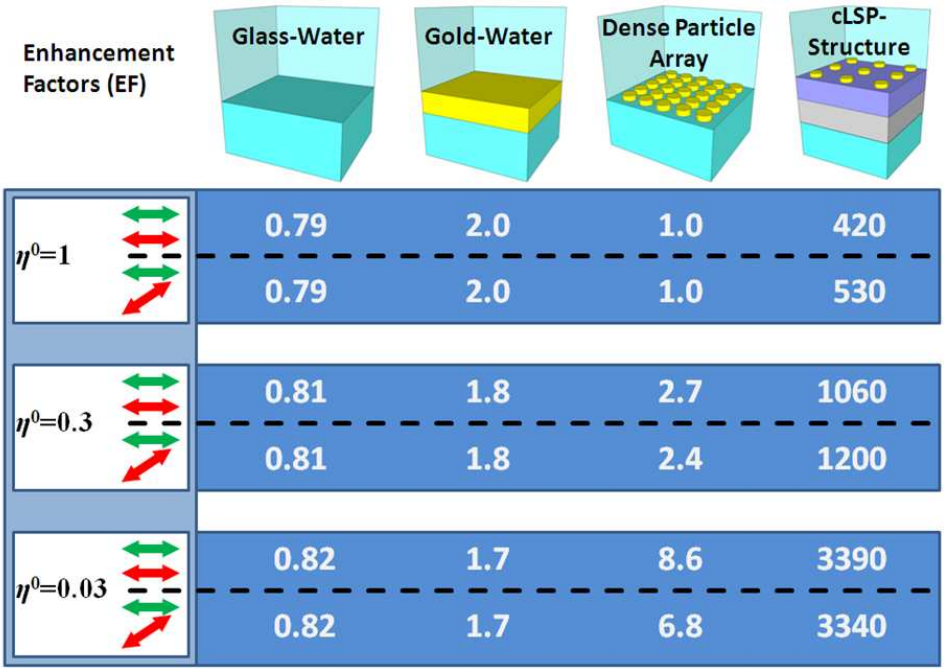

Figure 5.12 Comparison of enhancement factors EF for flat glass substrate, flat gold surface, dense particle array and structure supporting cLSPs. For the enhancement factor calculation different intrinsic quantum efficiencies η^0 are considered. Additionally, the two cases of (1) emission and absorption dipole are randomly oriented to each other and (2) emission and absorption dipole aligned, are considered. All values are given for a fluorophore to surface distance of $f = 20\ nm$ (graphic from [84]).

The glass-water interface shows an enhancement factor of $EF \approx 0.8$, which is marginal dependent on the considered intrinsic quantum efficiencies η_0. The decreased enhancement factor compared to fluorophore in aqueous environment ($EF = 1$) can be explained by the slightly reduced electric field intensity enhancement of $|E|^2/|E_0|^2$ =0.9 and the low collection efficiency due to the strong emission into the glass substrate.

The gold-water interface shows roughly two times higher enhancement factor compared to a fluorophore in aqueous environment. The enhancement can be attributed to the enhanced electric field intensity close to the interface $|E|^2/|E_0|^2$ =1.36 and an increase of collection efficiency due to the "mirror effect" of the gold. The enhancement factor slightly decreases for decreasing intrinsic quantum efficiency η_0.

The dense particle array shows no enhancement for intrinsic quantum efficiency of $\eta_0 = 1$, while for decreasing intrinsic quantum efficiency the enhancement factor increases up to EF=8.6 (6.8)

for $\eta_0 = 0.03$. The enhancement is attributed to the quantum efficiency enhancement η/η_0 and a moderate electric field intensity enhancement. This moderate field intensity enhancement is compensated for $\eta_0 = 1$ by quenching.

The cLSP structure shows highest fluorescence intensity enhancement factor of EF=420 (530) for an ideal dye with $\eta_0 = 1$ and EF=1060 (1200) for a typical dye with $\eta_0 = 0.3$ (such as Cy5 and Alexa Fluor 647). Even higher enhancements can be achieved for low quantum efficiency dyes $\eta_0 = 0.03$ leading to an enhancement factor of EF=3390 (3340). The high enhancements are attributed to the high electric field intensity enhancement $|E|^2/|E_0|^2 > 100$, the directional emission of fluorescence light (ten times more directional than a flat glass substrate) and the increase of quantum efficiency for low intrinsic quantum efficiency dyes.

In general, it can be seen that there is no significant difference in the enhancement factor EF of the structures we studied between (1) random orientation of emission dipole $\vec{\mu}_{em}$ to absorption dipole $\vec{\mu}_{ab}$ and (2) emission dipole $\vec{\mu}_{em}$ aligned to absorption dipole $\vec{\mu}_{ab}$ is observed.

5.4 Experimental

5.4.1 Structure preparation

In the following section, protocols for the preparation of the cLSP structure (introduced in section 5.2) by interference lithography and nanoimprint lithography are presented.

5.4.1.1 Interference lithography

The cLSP structure introduced in section 5.2 has been prepared by interference lithography. The basic concept of interference lithography has been introduced in section 3.2.1. The detailed preparation scheme is given in Figure 5.13.

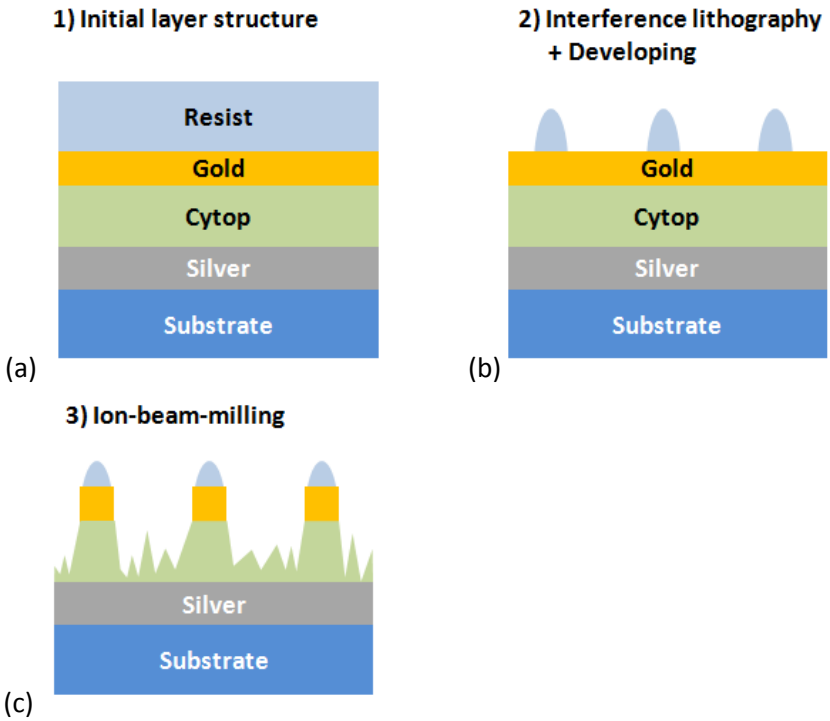

Figure 5.13 Preparation scheme of structure supporting cLSP resonance.

Firstly an initial layer structure is prepared. On a clean BK7 substrate, 4 nm chromium followed by 120 nm silver are deposited by thermal evaporation (HHV AUTO 306 from HHV LTD) in vacuum better than $1 \cdot 10^{-6}\, mBar$. Afterwards the fluoropolymer Cytop CTL-809NMD (from Asahi Glass Co.) is mixed with the solvent CT Solv 1820 (from Asahi Glass Co.) in a 1:2 ratio. The mixture is spin coated at 3500 rpm for 120 s and then baked on a hotplate for 60 min at 160°C. The resulting thickness of the polymer layer is 120 nm. On top of the Cytop layer, 50 nm of gold is deposited by thermal

evaporation. The final layer is the photoresist Microposit S1805 (from Shipley Company, USA). The resist is mixed with the solvent propylene glycol monomethyl ether acetate (from Sigma Aldrich) in a 1:2 ratio. The mixture is spin coated at 5500 rpm for 45 s, followed by a softbake on a hotplate at 95°C for 2 min. The layer thickness of the photoresist is (66 +/- 5) nm.

The substrate is then installed in the interference lithography setup (see Figure 3.8). The angle θ =20.7 deg was chosen to achieve a period of Λ =460 nm. The sample was first exposed for 5 min with 18.4 μW/cm^2 in one position, then rotated by 90 deg and exposed one more time with same duration and intensity. To achieve a proper reference spot for optical characterization (see section 3.3.1), namely a flat metal surface, one half of the sample was further exposed for 10 min by the UV laser beam with a plane wave, while the other half was blocked from irradiation. As the Microposit S1805 resist is a positive resist, this overexposure results in the development process to completely wash off of the resist on this half and thus a good reference spot is obtained. After the exposure, the sample was put into the developer AZ 303 (from MicroChemicals), mixed with distilled water in a 1:15 ratio, for 120 s. The resulting AFM data (acquired in tapping mode) plus cross section is shown in Figure 5.14.

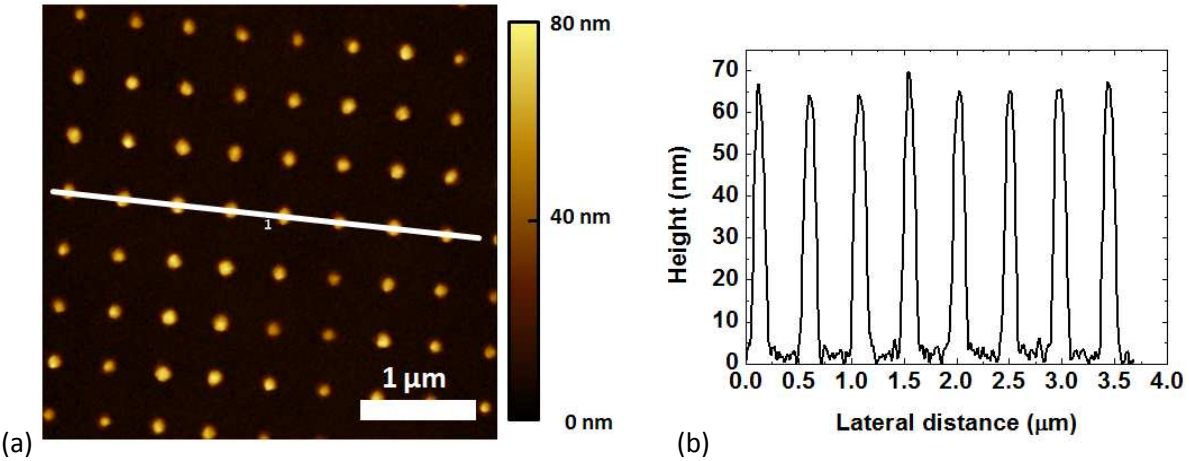

(a) (b)

Figure 5.14 (a) AFM image after interference lithography development process (b) cross section of AFM image, position indicated in (a).

The height of the produced resist nanoparticles can be seen in the AFM cross section of Figure 5.14 (b) and is around 65 nm. The period of Λ = (460 +/-2) nm agrees nicely with the desired one. The diameter of particles is hard to estimate from AFM data, as at such small dimensions the tip geometry of the AFM cantilever (PPP-NCHR from NANOSENSORS) starts to play a crucial role. It can be seen in Figure 5.13 (c) that the next step in fabrication of metallic nanoparticles is the use of the resist particles as an etch mask. The etching method applied is Ar ion beam etching, a physical etching method in which Ar ions are accelerated and knock out the target atoms from the structure. The etching rate of this method is dependent on incident angle of the ion-beam to the target, the

acceleration voltage and the target material. In Table 5.1 the etching rates of all materials used in the cLSP structure fabrication are given for 70 deg incident angle and an acceleration voltage of 500 V.

Material	Etching rate [nm/min]
Resist S1805	6.5+/- 2.1
Gold	12 +/- 2
Cytop CTL – 809NMD	120 +/- 10
Silver	9 +/-1

Table 5.1 Ar ion beam etching rates at 70 deg incident angle of several materials used in the fabrication of the cLSP structure.

Table 5.1 indicates that the photoresist S1805 has a lower etching rate than gold and is therefore suited as an etching mask. The results after 5 min of the etching process are shown in Figure 5.15.

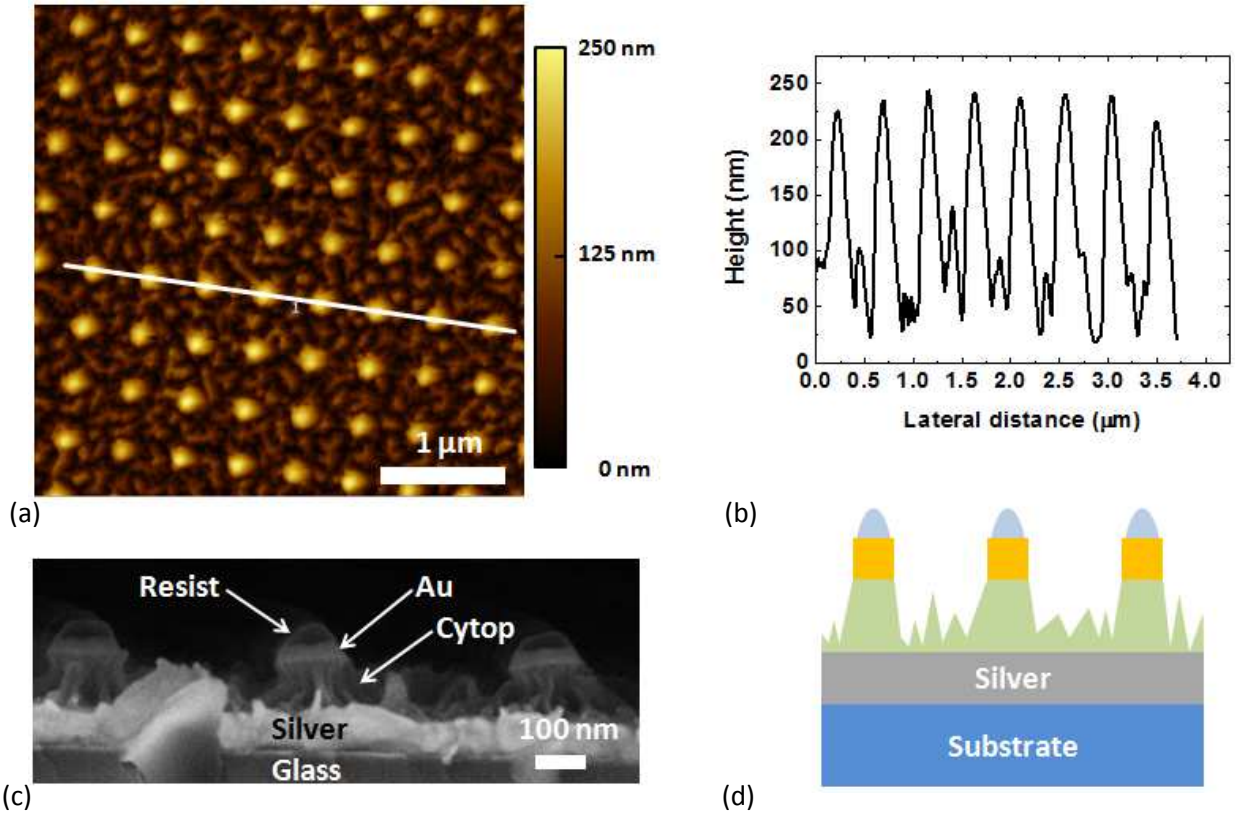

Figure 5.15 (a) AFM image of structure after ion beam milling (b) cross section of AFM image in (a) with profile line indicated by a white line.(c) SEM cross section of the structure after ion beam milling. (d) Schematic of the structure.

The AFM image in Figure 5.15 (a) and the cross section in Figure 5.15 (b) indicate that the roughness of the substrate is highly increased, as well as the particle height from before 65 nm to around 200 nm after etching. The strong increase of roughness and feature height is due to the very high etching rate of Cytop (see Table 5.1), which is around 10 times bigger than the etching rate of the resist. It

will be seen in the subsequent optical characterization that this high roughness will not influence the optical properties of the structure. To further elucidate the structure after ion beam etching, the structure was broken and a cross section image was taken by scanning electron microscope (SEM) (see Figure 5.15 (c)). It can be seen that the gold disks are placed on irregular shaped poles of Cytop and have a resist cap on top. Efforts were made to remove this resist cap by sonication in acetone for 30 min. The initial photoresist before the physical milling process is very soluble in acetone. Nevertheless, the SEM images before and after the sonication revealed that the resist cap stayed on top of the particles. This hardening of polymers is a widely known problem when using ion beam etching. Due to the etching, the polymer changes its intrinsic properties and is no longer solvable in the original solvents. The gold particle diameter is D=130 nm and the particle height is 50 nm. The side walls of the gold particles have a slight conical shape due to the etching process.

5.4.1.2 Nanoimprint lithography

Another method for large area fabrication of nanostructures is nanoimprint lithography (NIL). NIL uses a master structure for the preparation of working stamps, with which copies of the master can be produced. While NIL gives the possibility to structure a resist, for the fabrication of nanoparticles, additional processing steps, such as etching and lift off need to be applied. This is due to the fact that so far no NIL process is available, which allows for residual layer free imprint of nanometer scale features and therefore additional etching is necessary (see Figure 5.16 (a)). A possible fabrication scheme of nanoparticles is depicted in Figure 5.16.

In our work, the structure on a Si-master was a 2D array of circular posts with diameter D=150 nm, height 100 nm and period $\Lambda = 500\ nm$ on a total area of (1 x 1) mm² (from Temicon - micronano solutions). The working stamp was produced by casting PDMS (Sylgard 184 from Dow Corning) over the master and let it heat cure overnight at 60 °C. The PDMS stamp was then placed onto a pre prepared layer structure without applying any pressure. The layer structure consists of a cleaned BK7-glass substrate, 64 nm of PMMA and 110 nm of Amonil MMS 10 photoresist (from AMO GmbH). The PMMA powder (form Sigma Aldrich) was dissolved in toluene to achieve a 2 wt% solution. The PMMA solution was spin coated with 3000 rpm for 60 s and let dry overnight. Amonil MMS10 was spin coated at 3000 rpm for 120 s. The substrate with PDMS working stamp on top was placed in a UV chamber (UV lamp Bio-Link 365, Vilber Lourmat) and irradiated with a dose of $10\ J/cm^2$ at λ=365 nm. Afterwards, the PDMS stamp was easily detached from the substrate. For a lift off process the imprinted opening hole (shown in Figure 5.16 (a)) needs to reach the substrate. This can be achieved by several etching methods including wet chemical etching and physical etching. The etching method used in this work is Ar ion beam milling as a physical etching method. A sacrificial layer is needed

below the photoresist to allow for a lift off process, as the UV cured polymer is cross linked and hard to dissolve in any chemical. PMMA has been used as a sacrificial layer due to its good solubility in non-toxic solvents such as acetone. After physical etching through both polymer layers, 2 nm Cr and 40 nm Au have been deposited by vacuum thermal evaporation (HHV AUTO 306 from HHV LTD) in vacuum better than $1 \cdot 10^{-6} mBar$. Afterwards the sample was placed in acetone and sonicated for 160 min.

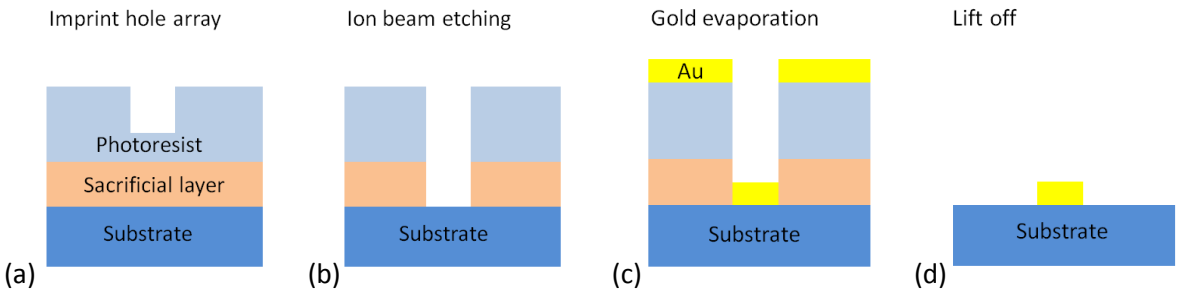

Figure 5.16 Schematic of nanoimprint lithography for fabrication of nanoparticle array.

The atomic force microscope (AFM) images after different processing steps are shown in Figure 5.17. The cantilever used was PPP-NCHR (from NANOSENSORS with force constant 42 N/m and resonance frequency around 300 kHz). Figure 5.17 (a) shows the AFM image of the replicated nanostructure in Amonil MMS 10 resist without any additional etching steps. Figure 5.17 (b) shows the AFM picture after 4 min Ar ion beam etching at 70 deg incident angle of the ion beam onto the sample. Figure 5.17 (c) shows the AFM image after a lift off in Acetone for 160 min with sonication.

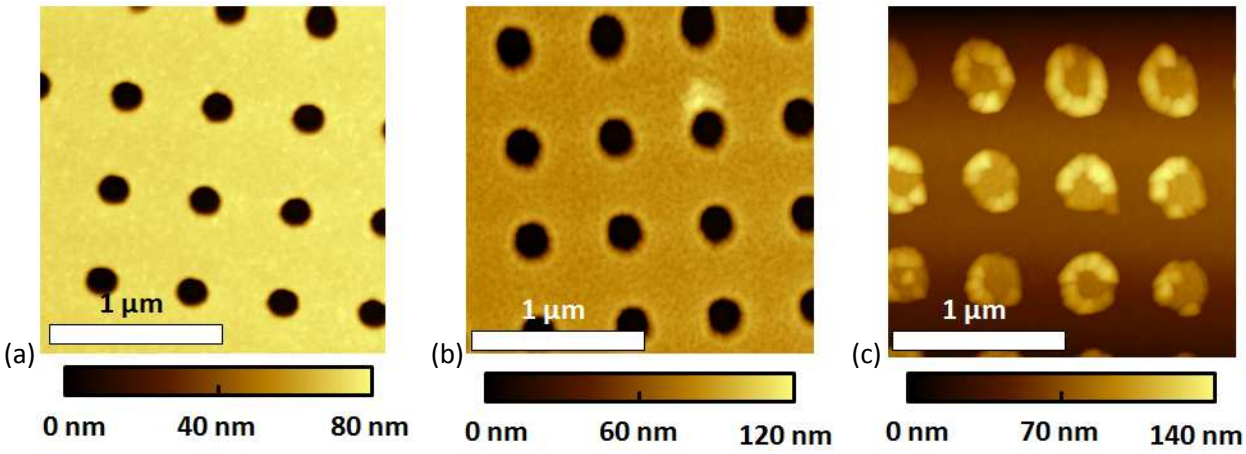

Figure 5.17 AFM images (a) after imprint into Amonil MMS 10 photoresist, (b) after 4 min of Ar-ion-beam-milling and (c) after lift off in acetone.

To further analyze the AFM images, cross section of the hole features in Figure 5.17 (a) and (b) and the nanoparticle in Figure 5.17 (c) have been extracted and summarized in Figure 5.18. It can be seen, that the profile after the imprint (black line) shows that the hole diameter at the upper rim is

around D=200 nm and the depth is 75 nm. The bottom of the hole shows a rather uneven profile. The side walls in the cross section of the holes are slightly tilted. This can be due to the imprinting process or can be an artifact of the pyramidal shape of the cantilever tip used in the AFM.

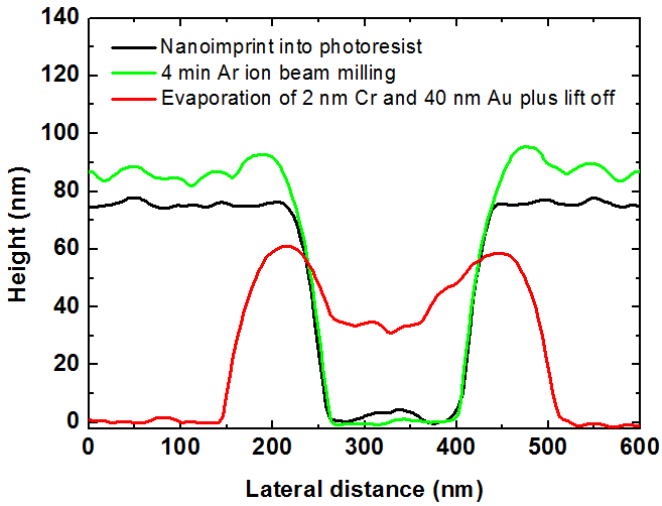

Figure 5.18 Cross sections of AFM images after different processing steps.

After the ion beam milling process (green line) the depth of the hole is increased to 85 nm due to the higher etching rate of PMMA compared to the Amonil MMS 10 photoresist (see Table 5.2). The surface roughness in the space between the holes is slightly increased and a ring modulation around the hole can be observed (see in addition Figure 5.17 (b)). The bottom of the hole is rather flat, which indicates, that the ion beam etching has been completed successfully to the glass substrate.

Material	Etching rate [nm/min]
Amonil MMS 10	17 +/- 5
PMMA	26 +/- 5
mrUV-cur-100	8.5 +/- 0.8
LOR1A	8.4 +/- 1.2
Bk7 glass	2.1 +/-0.3

Table 5.2 Ar ion beam etching rates for various materials under study for angle of incidence of 70 deg.

The cross section of the nanoparticle after evaporation of metal and lift off (red line profile in Figure 5.18) shows a much bigger diameter than the actual previous hole diameter after the ion beam milling (green line). The height of the particle in the center is around 40 nm and agrees nicely with the evaporated metal thickness of 42 nm. At the rim of the nanoparticle there is an additional ring with a height of 60 nm. The additional ring can be as well nicely seen in the AFM image (Figure 5.17 (c)) and can be explained by a polymer hardening due to the ion beam milling process.

To verify the cause of the polymer hardening, a different etching method based on reactive ion etching has been utilized. Reactive ion beam etching benefits from a combination of physical and

chemical etching mechanisms and allows for more material specific etching rates depending on the used etching gas [161]. The process parameters were 30 s etching with a gas mixture of 10 sccm O_2 and 30 sccm SF_6 at 40mTorr and power 100 W followed by 30 sccm O_2 at 100mTorr at power 100W. The results of the reactive ion etching were similar to the already shown AFM images with Ar ion beam milling.

The second possibility for the polymer hardening is the used polymers itself. To check the influence of the materials, the polymer for the sacrificial layer and the photoresist (see Figure 5.16 (a)) were changed. The initial PMMA for the sacrificial layer was replaced by LOR 1A (from MicroChem) and the photoresist was changed from Amonil MMS 10 to mr-UVCur21-100 (from micro resist technology GmbH). First 180 μl of LOR1A has been spin coated at 4000 rpm for 60 s on a cleaned BK7 substrate, followed by a softbake on the hotplate for 5 min at 200°C resulting in a polymer thickness of (100 +/- 3) nm. Afterwards 180 μl of mr-UVCur21-100 was spin coated on top of the LOR 1A layer at 3000 rpm for 60 s, followed by a softbake at 80°C for 60 s on a hotplate. For the UV curing of mr-UVcur-100 it is important that no oxygen is present in the curing process. As PDMS as a working stamp is permeable to oxygen it cannot be used for the imprint process. Therefore OrmoStamp (from micro resist technology GmbH) was used as a new working stamp material. The stamp fabrication was done by the following recipe. An adhesion promoter (OrmoPrime 08, from micro resist technology GmbH) was spin coated (4000 rpm for 60 s) onto a cleaned BK7 substrate, followed by a baking step at 150°C for 5 min at hotplate. Afterwards, $200\ \mu l$ of OrmoStamp was pipetted onto the Si-master structure and the BK7 substrate with the adhesion promoter was clamped on it. This clamped stack was then put to the oven for 2 min at 150°C and UV cured in UV chamber at $\lambda = 365\ nm$ with a dose of 30 mJ/cm². Afterwards the stack was placed for additional 10 min into an oven at 130°C. After separating the Si-master from the glass substrate with the motive transferred into the OrmoStamp, the working stamp is ready to use.

The OrmoStamp was placed on the glass substrate with the sacrificial polymer layer and the photoresist and was pressed together by a clamp. The stack was then cured in a UV chamber with 30 mJ/cm². After removing the OrmoStamp from the substrate, the sample was further processed by Ar ion beam etching. The etching was performed for 14 min until the glass substrate was reached. Let us note, that the etching is much longer for the new polymers, as the etching rates are lower (see Table 5.2) and a thicker sacrificial layer was used. The next processing step described in Figure 5.16 (c) would be the deposition of a metal. As the focus is on the effect of the polymer hardening due the ion beam milling, the metal deposition has been omitted and the lift off has been performed directly. The lift off was done by first sonicating the sample for 7 min in MF-24A (Microposit MF-24A developer from Shipley Europe), followed by 2 min sonication in acetone. The result of the lift off is shown in the AFM image in Figure 5.19. The black circular regions (with height value 0 nm) indicate a

slightly too long etching process, which results in the etching into the glass substrate. The circular regions are located at the positions of the former holes in the resist. Around some of them, bright donut shaped polymer rings are present. This indicates that the LOR1A/mr-UVCur-100 polymer system also suffers from polymer hardening. Due to these difficulties the cLSP sample preparation was not further pursued by nanoimprint lithography. In addition, it needs to be noted that the polymer ring around the particle would hinder the functionalization of the nanoparticles at the sidewalls with biorecognition elements.

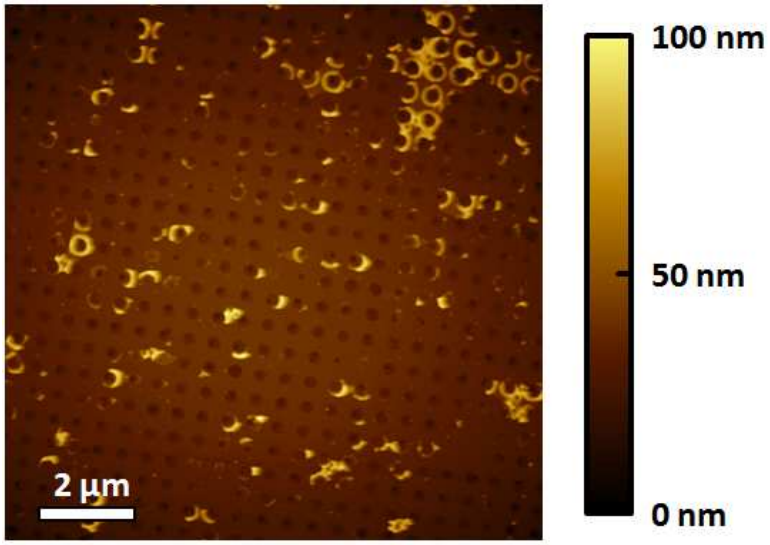

Figure 5.19 AFM image after Ar ion beam milling and lift off process with LOR1A as sacrificial layer and mr-UVCur-100 as photoresist.

5.4.2 Spectrum of modes

The optical properties of the structures produced by interference lithography (see section 5.4.1.1) are optically characterized with the angle wavelength spectrometer introduced in section 3.3.1. The samples were clamped to a flow-cell, where water was flowed during the measurements of the reflectivity spectra. At first, the samples were characterized at 0.6 deg in TM-mode. The measurement at directly 0 deg (normal incident light) is unpractical as the reflected beam is blocked by a mirror before entering the detector. In Figure 5.20 the reflectivity spectra of two samples are plotted. In the measurement curves the two resonances predicted by the simulations (see section 5.3) are clearly visible. The resonance at wavelength λ =700 nm is attributed to the collective localized surface plasmons (cLSPs). The cLSP resonance position is dependent on the period Λ of the particle array and on the particle diameter D. As the particle diameter is D=130 nm and thus 20 nm bigger than in the simulations of section 5.3.1, the resonance is shifted to higher wavelength. It has

been stated that the cLSPs need a refractive index symmetric environment. As the rough Cytop surface has the same refractive index as the water, with which the structure is covered, the nanoparticles are placed in a homogenous dielectric environment ($n \approx 1.33$) and the Cytop roughness does not influence the cLSP resonance.

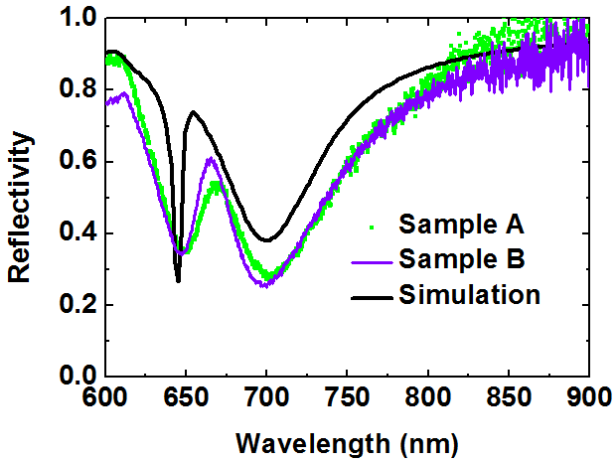

Figure 5.20 Reflectivity spectra at 0.6 deg for TM polarization of two different samples and simulation curve.

The resonance at wavelength λ =646 nm is attributed to the surface plasmon polariton (SPP) resonance on the silver surface. This value agrees perfectly with the value for analytical calculation with Eq. (1.16). Nevertheless, the value is 12 nm higher than predicted for the complex cLSP structure in the simulation section 5.3.1. This deviation can be explained by the anti-crossing behavior of the localized surface plasmons (LSPs) and the SPPs [152, 153]. Due to the occurrence of the localized surface plasmon resonance (LSPR) at higher wavelength the effect is not adequately pronounced. The width of the SPP resonance is rather broad. This can be explained by a possible etching into the flat silver layer in the fabrication process by the Ar ion beam etching, resulting in an increased roughness in the silver. The increased roughness leads to shorter propagation length and broader resonances. The reduced coupling efficiency of the SPP mode compared to simulations in section 5.3.1 can be explained by the additional resist cap on top of the gold disk. The resist cap changes the effective distance between the center of the scattering particle (gold disk plus resist cap) and thus the condition for constructive interference (see Eq. (5.3)) is not fulfilled anymore.

The FDTD simulation curve included in Figure 5.20 takes the actual geometry of the fabricated cLSP nanostructure into account. The simulation parameters are, a spacer with a thickness of $d_b = 120\,nm$, gold disk with a diameter of D=130 nm and height of 50 nm. The resist cap on top was assumed to have diameter D=130 nm, height 40 nm and refractive index of n=1.65 (refractive index value from datasheet of Microposit S1805 from Shipley Company). It can be seen that the shape and position of the cLSP mode (at around λ =700 nm) is nicely reproduced by the simulation.

For the SPP mode (at around 646 nm), the resonance position is in accurate agreement, while the shape of the simulated SPP mode is much sharper. This can be explained with the increased roughness of the silver in the experiment, which is not considered in the simulation. The angular wavelength reflectivity measurement for the produced cLSP structure is shown in Figure 5.21 for TM polarized incident light.

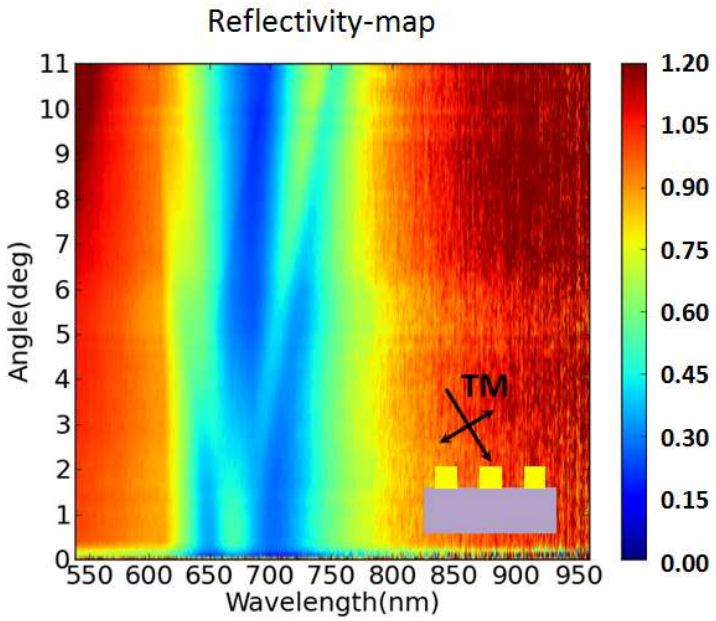

Figure 5.21 Angle and wavelength dependent reflectivity measurement of the fabricated cLSP structure for TM-polarization. The light polarization is shown in the inset.

The measurements have been performed with the setup described in section 3.3.1. The spectra for small angles (below 1 deg) has already been extensively described before. For higher angles in TM polarization one would expect, that the cLSP resonance stays at the same wavelength position, while the SPP-mode splits up into two branches ((-1,0)-mode and (+1,0)-mode). In the measurement, it can be seen that the blue regions of the different resonances never overlap which confirms the anti-crossing behavior of the cLSP mode and the SPP mode.

5.5 Effect of reduced sensing area

In this section we aim to investigate the effect of reduced binding sites (biorecognition elements B) on the detected fluorescence signal. Localized surface plasmons show an increased electric field intensity enhancement only close to the nanoparticle surface, therefore it is advantageous to only bind analytes A to the surface of the nanoparticles and leave the rest of the sensor unmodified. This situation leads to a reduced sensing surface and is illustrated in Figure 5.22.

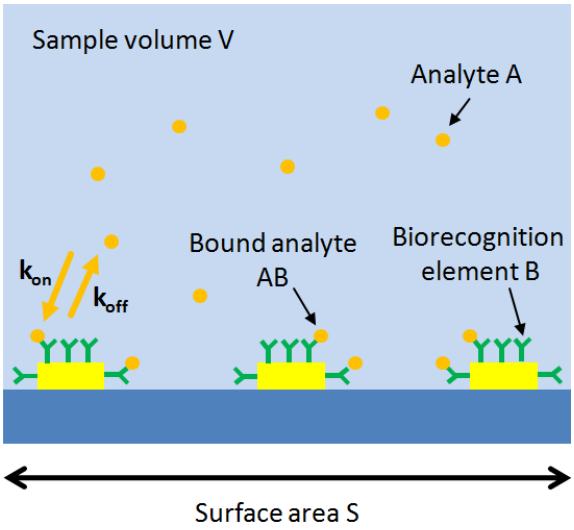

Figure 5.22 Sketch of analyte binding to the plasmonic active region.

The signal detected from a fluorescence biosensor F is proportional to the enhancement factor EF provided by plasmonic enhancement effects and the number of fluorescence labeled analytes bound to the nanoparticle surface N_{AB}:

$$F \propto EF \cdot N_{AB} \tag{5.4}$$

Using the Langmuir isotherm derived in section 1.6 (Eq. (1.32)) and combining with Eq. (5.4) the fluorescence signal F can be written as [46]:

$$F \propto EF \cdot S \frac{c_{A,0}}{\frac{K_d}{\xi c_{B,0}} + \frac{S}{V}} \tag{5.5}$$

where S is the surface area from which the signal is detected, V is the sample volume containing analyte A, ξ is the fraction of the surface area that contains biorecognition elements compared to the total surface area S, K_d is the dissociation constant, $c_{A,0}$ the total concentration of initially inserted analyte A and $c_{B,0}$ the initially free concentration of biorecognition elements B.

When the dissociation constant K_d and the sample volume V are small, the limit of $K_d V \ll S\xi c_{B,0}$ (with $S\xi c_{B,0}$ is the number of biorecognition elements B) is fulfilled and Eq. (5.5) simplifies to $F \propto EF \cdot V \cdot c_{A,0}$. In this limit of high affinity binding and low sample volumes, the fluorescence signal F is directly proportional to the concentration of analyte A and independent on the number of biorecognition elements [46]. The effect of plasmonic hotspots can be efficiently used and there is no signal loss due to the small detection area on the plasmonic nanoparticles.

Another extreme case is when $K_d V \gg S\xi c_{B,0}$ and therefore Eq. (5.5) modifies to $F \propto EF \cdot S \cdot \xi \cdot c_{B,0} \cdot c_{A,0}$. In this case the fluorescence signal is dependent on the number of biorecognition elements and the use of plasmonic hotspot with reduced surface area is not advantageous [46]. It should be noted that selective functionalization of plasmonic hotspots has been reported for nanoholes, where only the nanohole walls were functionalized while the rest of the structure was passivated [162].

5.6 Summary

We have shown that the novel approach of collective localized surface plasmons (cLSP) holds great potential for fluorescence enhancement in epifluorescence geometry. We propose a structure consisting of a rectangular array of gold disks placed on a low refractive index polymer above a silver film. Theoretical predictions show that the fluorescence for commercially available and widely used dyes can be enhanced by $EF{\sim}10^3$ compared to conventionally used substrates. This high performance has been achieved by the use of two resonances which are designed to overlap with absorption and emission band of the dye.

The simulations took into account full mechanisms of plasmon enhanced fluorescence including the plasmon driven excitation rate at λ_{ab}, change of intrinsic quantum yield and directional outcoupling of fluorophores light to far-field by plasmons at λ_{em}. In particular, the high fluorescence signal enhancement of $EF{\sim}10^3$ can be attributed to a 10-fold increase of collection efficiency, an almost 100-fold increase in excitation rate and a doubled quantum yield for $\eta_0 = 0.3$ compared to a flat glass substrate.

Moreover, cLSP structure in combination with local functionalization of the nanodisks holds great potential for future fluorescence assay applications. Let us note that due to the reduced area for capturing analytes with biorecognition elements, certain conditions need to be fulfilled to fully exploit the predicted performance and achieve low limits of detection. In particular, the binding affinity of the capture antibody needs to be high and low concentrations of analytes need to be applied (see section 5.5) to fully exploit the sensor abilities.

We have introduced a method to produce such cLSP structures by interference lithography and additional dry etching and have shown by optical characterization that two resonances have been observed. Deviations from the initial simulations have been explained by geometry deviations from the initial design and the mode spectrum has been explained.

6 Summary and conclusions

This thesis aims for plasmonic signal amplification in fluorescence assays, particularly for applications in medical diagnostics that requires highly sensitive detection of biomarkers. An introduction chapter covers an extensive literature research on state-of-the-art plasmonic structures for plasmon-enhanced fluorescence. Based on the literature search, two promising approaches were selected that allow simultaneous enhancement of the three main mechanisms of plasmon-enhanced fluorescence, namely the increase of excitation rate, improvement of intrinsic quantum efficiency and control of angular distribution of emitted fluorescence light by fluorophores that are used as labels in bioassays. The first approach utilizes crossed periodically corrugated metallic surfaces that support propagating surface plasmons. The second approach relies on arrays of metallic nanoparticles that allow for diffractive coupling of localized surface plasmons.

Both structures have been designed to operate in fluorescence detection systems with epifluorescence geometry, such as fluorescence microscopes and microarray scanners in which the fluorescence light is excited and collected from above a substrate in the direction perpendicular to the surface. In addition, the structures were optimized for the amplification of fluorescence signal in sandwich immunoassays with regularly used organic dyes with absorption and emission wavelength in the red part of spectrum (in particular Cy5 and Alexa Fluor 647) and quantum yield of $\eta \sim 0.3$.

In the theoretical part of the work (section 3.1), a complete model describing the near-field and far-field characteristics of fluorophores interacting with metallic nanostructures was developed based on finite-difference time-domain method (FDTD). This model was employed for design optimization of respective nanostructures supporting surface plasmon polaritons and localized surface plasmons. For the crossed gold periodic gratings, parameters that allow increase in the fluorescence signal by a factor of $EF \sim 10^2$ were identified. The enhancement is attributed to the intense field of SPPs and the highly directional outcoupling of fluorescence light. Collective localized surface plasmons allow for even stronger field confinement. FDTD simulations were applied to design a novel two-resonance structure in which the absorption and emission bands of a fluorophore each overlap with a plasmon resonance. This structure was tuned to provide an order of magnitude higher amplification efficiency in fluorescence signal intensity of $EF \sim 10^3$. Let us note that this value is comparable to the best reported works which were demonstrated only for dyes with much lower intrinsic quantum efficiency η_0.

In the experimental part of the work, the use of UV laser interference lithography and UV nanoimprint lithography (NIL) was applied for cost-effective large area preparation of identified metallic nanostructures. Series of crossed metallic gratings supporting surface plasmons polaritons were prepared by interference lithography and replicated by NIL. The grating showed fluorescence

enhancement that excellently matched theoretical predictions. Numerous NIL approaches in combination with lift-off for fabrication of cylindrical metallic nanoparticle arrays were investigated. The study shows possible routes for their preparation which would require improvement of the lift-off process. In order to avoid a lift-off step, an interference lithography based protocol was developed. This approach was demonstrated to allow for successful preparation of structures exhibiting collective localized surface plasmon modes similar to that predicted by simulations.

Finally, crossed gratings were applied for the fluorescence-based detection of interleukin 6 by using a sandwich immunoassay. The measured enhancement of fluorescence signal reached a value of $EF \sim 10^2$ without increasing the background. This feature was particularly interesting for the measurement of reaction kinetics that is otherwise masked by strong background signal originating from the fluorescence signal of molecules contained in the bulk solution. Compared to other works, a 2D silver grating [34] and a 1D silver groove grating [111] showed similar enhancement factors. Taking into account the different reference systems used for determining the enhancement factor, the enhancement of the gold crossed grating can be assumed to be two times higher. Moreover, the use of gold instead of silver offers plasmonic substrates that are more stable over long durations due to the absence of rapid oxidation of silver.

The thesis successfully showed new approaches that hold potential to evolve the fundamental research in plasmonic amplification of fluorescence signal into practical applications in assays for detection of various chemical and biological analytes by using commercially available antibodies and widely spread fluorescence instruments for readout of the immunoassays. In particular, the use of fabrication methods such as interference lithography and nanoimprint lithography provides attractive ways for mass-production compatible preparation of identified structures. The work investigated novel plasmonic nanostructures that hold potential for improving the sensitivity by a factor exceeding values of 10^3 that is expected to open doors for the analysis of new biomarkers that are present at minute concentrations in bodily fluids. For example, with current implementations of fluorescence assays these biomarkers are not detectable in promising matrices such as saliva (concentrations are approximately two orders of magnitude smaller with respect to that in blood serum). The presented amplification strategies can offer means for rapid and simple analysis of such samples that can be collected non-invasively and potentially bring the biomarker-based analysis closer to patients.

7 Acknowledgements

Not available in electronic version.

8 References

[1] C. J. Huang, A. Sessitsch, J. Dostalek, and W. Knoll, "Long range surface plasmon-enhanced fluorescence spectroscopy biosensor for ultrasensitive detection of E. coli O157:H7," *Analytical Chemistry,* vol. 83, pp. 674–677, 2011.

[2] O. Lazcka, F. J. Del Campo, and F. X. Munoz, "Pathogen detection: A perspective of traditional methods and biosensors," *Biosensors and Bioelectronics,* vol. 22, pp. 1205-1217, Feb 2007.

[3] P. Leonard, S. Hearty, J. Brennan, L. Dunne, J. Quinn, T. Chakraborty, and R. O'Kennedy, "Advances in biosensors for detection of pathogens in food and water," *Enzyme and Microbial Technology,* vol. 32, pp. 3-13, Jan 2003.

[4] A. I. Dragan, M. T. Albrecht, R. Pavlovic, A. M. Keane-Myers, and C. D. Geddes, "Ultra-fast pg/ml anthrax toxin (protective antigen) detection assay based on microwave-accelerated metal-enhanced fluorescence," *Analytical Biochemistry,* vol. 425, pp. 54-61, Jun 1 2012.

[5] A. P. Doherty, M. Bower, G. L. Smith, R. Miano, E. M. Mannion, H. Mitchell, and T. J. Christmas, "Undetectable ultrasensitive PSA after radical prostatectomy for prostate cancer predicts relapse-free survival," *British Journal of Cancer,* vol. 83, pp. 1432-1436, Dec 2000.

[6] Y. Wang, A. Brunsen, U. Jonas, J. Dostalek, and W. Knoll, "Prostate specific antigen biosensor based on long range surface plasmon-enhanced fluorescence spectroscopy and dextran hydrogel binding matrix," *Analytical Chemistry,* vol. 81, pp. 9625-9632, 2009.

[7] P. Domnanich, U. Sauer, J. Pultar, and C. Preininger, "Protein microarray for the analysis of human melanoma biomarkers," *Sensors and Actuators B-Chemical,* vol. 139, pp. 2-8, May 2009.

[8] V. Velusamy, K. Arshak, O. Korostynska, K. Oliwa, and C. Adley, "An overview of foodborne pathogen detection: In the perspective of biosensors," *Biotechnology Advances,* vol. 28, pp. 232-254, Mar-Apr 2009.

[9] G. S. Wilson and R. Gifford, "Biosensors for real-time in vivo measurements," *Biosensors & Bioelectronics,* vol. 20, pp. 2388-2403, Jun 2005.

[10] M. Bally, M. Halter, J. Voros, and H. M. Grandin, "Optical microarray biosensing techniques," *Surface and Interface Analysis,* vol. 38, pp. 1442-1458, Nov 2006.

[11] J. N. Anker, W. P. Hall, O. Lyandres, N. C. Shah, J. Zhao, and R. P. Van Duyne, "Biosensing with plasmonic nanosensors," *Nature Materials,* vol. 7, pp. 442-453, Jun 2008.

[12] B. Sepulveda, P. C. Angelome, L. M. Lechuga, and L. M. Liz-Marzan, "LSPR-based nanobiosensors," *Nano Today,* vol. 4, pp. 244-251, Jun 2009.

[13] H. Nakamura and I. Karube, "Current research activity in biosensors," *Analytical and Bioanalytical Chemistry,* vol. 377, pp. 446-468, Oct 2003.

[14] C. Hoppener and L. Novotny, "Exploiting the light-metal interaction for biomolecular sensing and imaging," *Quarterly Reviews of Biophysics,* vol. 45, pp. 209-255, May 2012.

[15] F. Yu, B. Persson, S. Lofas, and W. Knoll, "Attomolar sensitivity in bioassays based on surface plasmon fluorescence spectroscopy," *Journal of the American Chemical Society,* vol. 126, pp. 8902-8903, Jul 2004.

[16] G. Mie, "Beiträge zur Optik trüber Medien, speziell kolloidaler Metallösungen," *Annalen der Physik,* vol. 330, pp. 377–445, 1908.

[17] D. Sarid and W. A. Challener, *MODERN INTRODUCTION TO SURFACE PLASMONS*: CAMBRIDGE UNIVERSITY PRESS, 2010.

[18] C. F. Bohren and D. R. Huffman, *Absorption and Scattering of Light by Small Particles*: Wiley-VCH Verlag GmbH & Co. KGaA, 2004.

[19] J. Smajic, C. Hafner, L. Raguin, K. Tavzarashvili, and M. Mishrikey, "Comparison of Numerical Methods for the Analysis of Plasmonic Structures," *Journal of Computational and Theoretical Nanoscience,* vol. 6, pp. 763-774, Mar 2009.

[20] H. Raether, *Surface Plasmons on Smooth and Rough Surfaces and on Gratings*, 1 ed.: Springer-Verlag, Berlin, 1988.

[21] M. D. Arnold and M. G. Blaber, "Optical performance and metallic absorption in nanoplasmonic systems," *OPTICS EXPRESS,* vol. 17, pp. 3835-3847, Mar 2009.

[22] E. Kretschmann, "Die Bestimmung optischer Konstanten von Metallen durch Anregung von Oberflächenplasmaschwingungen," *Zeitschrift für Physik A Hadrons and Nuclei* vol. 241, pp. 313-324, 1971.

[23] G. Ruffato, G. Zacco, and F. Romanato, "Innovative Exploitation of Grating-Coupled Surface Plasmon Resonance for Sensing," in *Plasmonics - Principles and Applications*, K. Y. Kim, Ed.: INTECH, 2012.

[24] P. B. Johnson and R. W. Christy, "Optical-constants of noble-metals," *Phys. Rev. B,* vol. 6, pp. 4370-4379, 1972.

[25] K. T. Carron, W. Fluhr, M. Meier, A. Wokaun, and W. Lehmann, "Resonances of two-dimensional particle gratings in surface-enhanced Raman scattering," *Optics InfoBase,* vol. 3, pp. 430-440, 1986.

[26] J. S. Yuk, G. N. Gibson, J. M. Rice, E. F. Guignon, and M. A. Lynes, "Analysis of immunoarrays using a gold grating-based dual mode surface plasmon-coupled emission (SPCE) sensor chip," *Analyst,* vol. 137, pp. 2574-2581, 2012 2012.

[27] J. S. Yuk, E. F. Guignon, and M. A. Lynes, "Highly sensitive grating coupler-based surface plasmon-coupled emission (SPCE) biosensor for immunoassay," *Analyst,* vol. 138, pp. 2576-2582, 2013.

[28] Y. Jiang, H. Y. Wang, H. Wang, B. R. Gao, Y. W. Hao, Y. Jin, Q. D. Chen, and H. B. Sun, "Surface plasmon enhanced fluorescence of dye molecules on metal grating films," *Journal of Physical Chemistry C,* vol. 115, pp. 12636-12642, Jun 2011.

[29] Y. W. Hao, H. Y. Wang, Z. Y. Zhang, X. L. Zhang, Q. D. Chen, and H. B. Sun, "Time-Resolved Fluorescence Anisotropy of Surface Plasmon Coupled Emission on Metallic Gratings," *Journal of Physical Chemistry C,* vol. 117, pp. 26734-26739, Dec 2013.

[30] P. Andrew and W. L. Barnes, "Molecular fluorescence above metallic gratings," *Physical Review B,* vol. 64, p. 11, Sep 2001.

[31] E. Hwang, Smolyaninov, II, and C. C. Davis, "Surface plasmon polariton enhanced fluorescence from quantum dots on nanostructured metal surfaces," *Nano Letters,* vol. 10, pp. 813-820, Mar 2010.

[32] K. Ma, D. J. Kim, K. Kim, S. Moon, and D. Kim, "Target-Localized Nanograting-Based Surface Plasmon Resonance Detection toward Label-free Molecular Biosensing," *Ieee Journal of Selected Topics in Quantum Electronics,* vol. 16, pp. 1004-1014, Jul-Aug 2010.

[33] X. Zhang, H. T. Liu, and Y. Zhong, "Large-area electromagnetic enhancement by a resonant excitation of surface waves on a metallic surface with periodic subwavelength patterns," *OPTICS EXPRESS,* vol. 21, pp. 24139-24153, Oct 2013.

[34] X. Q. Cui, K. Tawa, K. Kintaka, and J. Nishii, "Enhanced Fluorescence Microscopic Imaging by Plasmonic Nanostructures: From a 1D Grating to a 2D Nanohole Array," *Advanced Functional Materials,* vol. 20, pp. 945-950, Mar 2010.

[35] C. Yasui, K. Tawa, C. Hosokawa, J. Nishii, H. Aota, and A. Matsumoto, "Sensitive Fluorescence Microscopy of Neurons Cultured on a Plasmonic Chip," *Japanese Journal of Applied Physics,* vol. 51, Jun 2012.

[36] E. Fort and S. Gresillon, "Surface enhanced fluorescence," *Journal of Physics D-Applied Physics,* vol. 41, Jan 2008.

[37] H. Aouani, O. Mahboub, N. Bonod, E. Devaux, E. Popov, H. Rigneault, T. W. Ebbesen, and J. Wenger, "Bright unidirectional fluorescence emission of molecules in a nanoaperture with plasmonic corrugations," *Nano Letters,* vol. 11, pp. 637-644, Feb 2011.

[38] P. Bharadwaj and L. Novotny, "Spectral dependence of single molecule fluorescence enhancement," *OPTICS EXPRESS,* vol. 15, pp. 14266-14274, Oct 2007.

[39] W. Deng and E. M. Goldys, "Plasmonic Approach to Enhanced Fluorescence for Applications in Biotechnology and the Life Sciences," *Langmuir,* vol. 28, pp. 10152-10163, Jul 10 2012.

[40] D. Magde, R. Wong, and P. G. Seybold, "Fluorescence quantum yields and their relation to lifetimes of rhodamine 6G and fluorescein in nine solvents: Improved absolute standards for quantum yields," *Photochemistry and Photobiology,* vol. 75, pp. 327-334, Apr 2002.

[41] G. W. Ford and W. H. Weber, "Electromagnetic interactions of molecules with metal surfaces," *Physics Reports,* vol. 113, pp. 195-287, 1984.

[42] Y. Teng, K. Ueno, X. Shi, D. Aoyo, J. Qiu, and H. Misawa, "Surface plasmon-enhanced molecular fluorescence induced by gold nanostructures," *Annalen der Physik,* vol. 524, pp. 733-740, Nov 2012.

[43] J. R. Lakowicz, K. Ray, M. Chowdhury, H. Szmacinski, Y. Fu, J. Zhang, and K. Nowaczyk, "Plasmon-controlled fluorescence: a new paradigm in fluorescence spectroscopy," *Analyst,* vol. 133, pp. 1308-1346, 2008.

[44] A. Kinkhabwala, Z. F. Yu, S. H. Fan, Y. Avlasevich, K. Mullen, and W. E. Moerner, "Large single-molecule fluorescence enhancements produced by a bowtie nanoantenna," *Nature Photonics,* vol. 3, pp. 654-657, Nov 2009.

[45] P. Bharadwaj, "Optical Antennas," *Advances in Optics and Photonics,* vol. 1, pp. 438-483, 2009.

[46] M. Bauch, K. Toma, M. Toma, Q. Zhang, and J. Dostalek, "Plasmon-Enhanced Fluorescence Biosensors: a Review," *Plasmonics,* vol. 9, pp. 781-799, 2014.

[47] R. Gill, L. J. Tian, W. R. C. Somerville, E. C. Le Ru, H. van Amerongen, and V. Subramaniam, "Silver nanoparticle aggregates as highly efficient plasmonic antennas for fluorescence enhancement," *Journal of Physical Chemistry C,* vol. 116, pp. 16687-16693, Aug 2012.

[48] C. W. Blackledge, T. Tabarin, E. Masson, R. J. Forster, and T. E. Keyes, "Silica nanoparticles containing a rhodamine dye and multiple gold nanorods," *Journal of Nanoparticle Research,* vol. 13, pp. 4659-4672, Oct 2011.

[49] S. Y. Liu, L. Huang, J. F. Li, C. Wang, Q. Li, H. X. Xu, H. L. Guo, Z. M. Meng, Z. Shi, and Z. Y. Li, "Simultaneous Excitation and Emission Enhancement of Fluorescence Assisted by Double Plasmon Modes of Gold Nanorods," *Journal of Physical Chemistry C,* vol. 117, pp. 10636-10642, May 2013.

[50] A. E.-d. E. A. Ragab, A. Gadallah, M. B. Mohamed, and I. M. Azzouz, "Effect of silver NPs plasmon on optical properties of fluorescein dye," *Optics and Laser Technology,* vol. 52, pp. 109-112, Nov 2013.

[51] Aouani, "Large molecular fluorescence enhancement by a nanoaperture with plasmonic corrugations," *OPTICS EXPRESS,* vol. 19, pp. 13056 - 13062, 2011.

[52] H. Aouani, O. Mahboub, E. Devaux, H. Rigneault, T. W. Ebbesen, and J. Wenger, "Plasmonic antennas for directional sorting of fluorescence emission," *Nano Letters,* vol. 11, pp. 2400-2406, Jun 2011.

[53] A. G. Curto, G. Volpe, T. H. Taminiau, M. P. Kreuzer, R. Quidant, and N. F. van Hulst, "Unidirectional emission of a quantum dot coupled to a nanoantenna," *Science,* vol. 329, pp. 930-933, Aug 2010.

[54] C. A. Balanis, *Antenna theory: analyses and design*: John Wiley and Sons, 2005.

[55] T. H. Taminiau, F. D. Stefani, and N. F. van Hulst, "Enhanced directional excitation and emission of single emitters by a nano-optical Yagi-Uda antenna," *OPTICS EXPRESS,* vol. 16, pp. 10858-10866, Jul 2008.

[56] D. Dregely, R. Taubert, J. Dorfmuller, R. Vogelgesang, K. Kern, and H. Giessen, "3D optical Yagi-Uda nanoantenna array," *Nature Communications,* vol. 2, p. 7, Apr 2010.

[57] C. Rodriguez-Emmenegger, M. Houska, A. B. Alles, and E. Brynda, "Surfaces Resistant to Fouling from Biological Fluids: Towards Bioactive Surfaces for Real Applications," *Macromolecular Bioscience,* vol. 12, pp. 1413-1422, Oct 2012.

[58] C. Vericat, M. E. Vela, G. Benitez, P. Carro, and R. C. Salvarezza, "Self-assembled monolayers of thiols and dithiols on gold: new challenges for a well-known system," *Chemical Society Reviews,* vol. 39, pp. 1805-1834, 2010.

[59] N. K. Chaki and K. Vijayamohanan, "Self-assembled monolayers as a tunable platform for biosensor applications," *Biosensors & Bioelectronics,* vol. 17, pp. 1-12, Jan 2002.

[60] J. C. Love, L. A. Estroff, J. K. Kriebel, R. G. Nuzzo, and G. M. Whitesides, "Self-assembled monolayers of thiolates on metals as a form of nanotechnology," *Chemical Reviews,* vol. 105, pp. 1103-1169, Apr 2005.

[61] H. Kim, J. Noh, M. Hara, and H. Lee, "Characterization of mixed self-assembled monolayers for immobilization of streptavidin using chemical force microscopy," *Ultramicroscopy,* vol. 108, pp. 1140-1143, Sep 2008.

[62] W. Knoll, M. Zizlsperger, T. Liebermann, S. Arnold, A. Badia, M. Liley, D. Piscevic, F. J. Schmitt, and J. Spinke, "Streptavidin arrays as supramolecular architectures in surface-plasmon optical sensor formats," *Colloids and Surfaces a-Physicochemical and Engineering Aspects,* vol. 161, pp. 115-137, Jan 15 2000.

[63] R. C. Weast, M. J. Astle, and B. W. H., *Handbook of Chemistry & Physics*: CRC Press, 1984.

[64] M. Schaeferling, S. Schiller, H. Paul, M. Kruschina, P. Pavlickova, M. Meerkamp, C. Giammasi, and D. Kambhampati, "Application of self-assembly techniques in the design of biocompatible protein microarray surfaces," *Electrophoresis,* vol. 23, pp. 3097-3105, Sep 2002.

[65] J. Homola, "Surface Plasmon Resonance Sensors for Detection of Chemical and Biological Species," *Chemical Reviews,* vol. 108, pp. 462 - 493, 2008.

[66] S. P. Song, L. H. Wang, J. Li, J. L. Zhao, and C. H. Fan, "Aptamer-based biosensors," *Trac-Trends in Analytical Chemistry,* vol. 27, pp. 108-117, Feb 2008.

[67] M. L. M. Vareiro, J. Liu, W. Knoll, K. Zak, D. Williams, and A. T. A. Jenkins, "Surface plasmon fluorescence measurements of human chorionic gonadotrophin: Role of antibody orientation in obtaining enhanced sensitivity and limit of detection," *Analytical Chemistry,* vol. 77, pp. 2426-2431, Apr 15 2005.

[68] Y. Wang, J. Dostalek, and W. Knoll, "Biosensor for detection of aflatoxin M_1 in milk based on long range surface plasmon enhanced fluorescence spectroscopy," *Biosensors and Bioelectronics,* vol. 24, pp. 2264-2267, 2009.

[69] J. S. Yuk, B. D. MacCraith, and C. McDonagh, "Signal enhancement of surface plasmon-coupled emission (SPCE) with the evanescent field of surface plasmons on a bimetallic paraboloid biochip," *Biosensors & Bioelectronics,* vol. 26, pp. 3213-3218, Mar 2011.

[70] S. Lofas, B. Johnsson, A. Edstrom, A. Hansson, G. Lindquist, R. M. M. Hillgren, and L. Stigh, "METHODS FOR SITE CONTROLLED COUPLING TO CARBOXYMETHYLDEXTRAN SURFACES IN

SURFACE-PLASMON RESONANCE SENSORS," *Biosensors & Bioelectronics,* vol. 10, pp. 813-822, 1995.

[71] K. B. Lee, S. J. Park, C. A. Mirkin, J. C. Smith, and M. Mrksich, "Protein nanoarrays generated by dip-pen nanolithography," *Science,* vol. 295, pp. 1702-1705, Mar 2002.

[72] T. Neumann, M. L. Johansson, D. Kambhampati, and W. Knoll, "Surface-plasmon fluorescence spectroscopy," *Advanced Functional Materials,* vol. 12, pp. 575-586, Sep 2002.

[73] K. Tawa, D. F. Yao, and W. Knoll, "Matching base-pair number dependence of the kinetics of DNA-DNA hybridization studied by surface plasmon fluorescence spectroscopy," *Biosensors & Bioelectronics,* vol. 21, pp. 322-329, Aug 2005.

[74] R. B. M. Schasfoort and A. J. Tudos, *Handbook of Surface Plasmon Resonance*: The Royal Society of Chemistry, 2008.

[75] L. L. H. Christensen, "Theoretical analysis of protein concentration determination using biosensor technology under conditions of partial mass transport limitation," *Analytical Biochemistry,* vol. 249, pp. 153-164, Jul 1997.

[76] D. A. Edwards, "The Effect of a Receptor Layer on the Measurement of Rate Constants," *Bulleting of Mathematical Biology,* vol. 63, pp. 301-327, 2001.

[77] Y. Wang, C. J. Huang, U. Jonas, T. X. Wei, J. Dostalek, and W. Knoll, "Biosensor based on hydrogel optical waveguide spectroscopy," *Biosensors & Bioelectronics,* vol. 25, pp. 1663-1668, Mar 2010.

[78] P. R. West, S. Ishii, G. V. Naik, N. K. Emani, V. M. Shalaev, and A. Boltasseva, "Searching for better plasmonic materials," *Laser & Photonics Reviews,* vol. 4, pp. 795-808, Nov 2010.

[79] D. J. Wu, Y. Cheng, and X. J. Liu, ""Hot spots" induced near-field enhancements in Au nanoshell and Au nanoshell dimer," *Applied Physics B-Lasers and Optics,* vol. 97, pp. 497-503, Oct 2009.

[80] A. M. Kern and O. J. F. Martin, "Excitation and reemission of molecules near realistic plasmonic nanostructures," *Nano Letters,* vol. 11, pp. 482-487, Feb 2011.

[81] D. Punj, M. Mivelle, S. B. Moparthi, T. S. van Zanten, H. Rigneault, N. F. van Hulst, M. F. Garcia-Parajo, and J. Wenger, "A plasmonic 'antenna-in-box' platform for enhanced single-molecule analysis at micromolar concentrations," *Nature Nanotechnology,* vol. 8, pp. 512-516, Jul 2013.

[82] J. Parsons, E. Hendry, C. P. Burrows, B. Auguie, J. R. Sambles, and W. L. Barnes, "Localized surface-plasmon resonances in periodic nondiffracting metallic nanoparticle and nanohole arrays," *Physical Review B,* vol. 79, Feb 2009.

[83] F. Xie, J. S. Pang, A. Centeno, M. P. Ryan, D. J. Riley, and N. M. Alford, "Nanoscale control of Ag nanostructures for plasmonic fluorescence enhancement of near-infrared dyes," *Nano Research,* vol. 6, pp. 496-510, Jul 2013.

[84] M. Bauch and J. Dostalek, "Collective localized surface plasmons for high performance fluorescence biosensing," *Optics Express,* vol. 21, pp. 20470-20483, 2013.

[85] R. Gordon, A. G. Brolo, D. Sinton, and K. L. Kavanagh, "Resonant optical transmission through hole-arrays in metal films: physics and applications," *Laser & Photonics Reviews,* vol. 4, pp. 311-335, Mar 2010.

[86] J. F. Masson, M. P. Murray-Methot, and L. S. Live, "Nanohole arrays in chemical analysis: manufacturing methods and applications," *Analyst,* vol. 135, pp. 1483-1489, 2010.

[87] D. X. Wang, T. Yang, and K. B. Crozier, "Optical antennas integrated with concentric ring gratings: electric field enhancement and directional radiation," *Optics Express,* vol. 19, pp. 2148-2157, Jan 2011.

[88] P. Genevet, J. P. Tetienne, E. Gatzogiannis, R. Blanchard, M. A. Kats, M. O. Scully, and F. Capasso, "Large enhancement of nonlinear optical phenomena by plasmonic nanocavity gratings," *Nano Letters,* vol. 10, pp. 4880-4883, Dec 2010.

[89] N. J. Halas, S. Lal, W. S. Chang, S. Link, and P. Nordlander, "Plasmons in strongly coupled metallic nanostructures," *Chemical Reviews,* vol. 111, pp. 3913-3961, Jun 2011.

[90] P. K. Jain, K. S. Lee, I. H. El-Sayed, and M. A. El-Sayed, "Calculated absorption and scattering properties of gold nanoparticles of different size, shape, and composition: Applications in biological imaging and biomedicine," *Journal of Physical Chemistry B,* vol. 110, pp. 7238-7248, Apr 2006.

[91] L. Shao, K. C. Woo, H. J. Chen, Z. Jin, J. F. Wang, and H. Q. Lin, "Angle- and energy-resolved plasmon coupling in gold nanorod dimers," *Acs Nano,* vol. 4, pp. 3053-3062, Jun 2010.

[92] R. K. Harrison and A. Ben-Yakar, "Role of near-field enhancement in plasmonic laser nanoablation using gold nanorods on a silicon substrate," *Optics Express,* vol. 18, pp. 22556-22571, Oct 2010.

[93] H. Fischer and O. J. F. Martin, "Engineering the optical response of plasmonic nanoantennas," *Optics Express,* vol. 16, pp. 9144-9154, Jun 2008.

[94] C. E. Talley, J. B. Jackson, C. Oubre, N. K. Grady, C. W. Hollars, S. M. Lane, T. R. Huser, P. Nordlander, and N. J. Halas, "Surface-enhanced Raman scattering from individual Au nanoparticles and nanoparticle dimer substrates," *Nano Letters,* vol. 5, pp. 1569-1574, Aug 2005.

[95] W. L. Johnson, S. A. Kim, Z. N. Utegulov, J. M. Shaw, and B. T. Draine, "Optimization of Arrays of Gold Nanodisks for Plasmon-Mediated Brillouin Light Scattering," *Journal of Physical Chemistry C,* vol. 113, pp. 14651-14657, Aug 20 2009.

[96] C. L. Haynes, A. D. McFarland, L. L. Zhao, R. P. Van Duyne, G. C. Schatz, L. Gunnarsson, J. Prikulis, B. Kasemo, and M. Kall, "Nanoparticle optics: The importance of radiative dipole coupling in two-dimensional nanoparticle arrays," *Journal of Physical Chemistry B,* vol. 107, pp. 7337-7342, Jul 31 2003.

[97] B. Lamprecht, G. Schider, R. T. Lechner, H. Ditlbacher, J. R. Krenn, A. Leitner, and F. R. Aussenegg, "Metal nanoparticle gratings: influence of dipolar particle interaction on the plasmon resonance," *Physical Review Letters,* vol. 84, pp. 4721-4724, May 2000.

[98] B. Auguie, X. M. Bendana, W. L. Barnes, and F. J. G. de Abajo, "Diffractive arrays of gold nanoparticles near an interface: Critical role of the substrate," *Physical Review B,* vol. 82, p. 7, Oct 2010.

[99] Y. Z. Chu, E. Schonbrun, T. Yang, and K. B. Crozier, "Experimental observation of narrow surface plasmon resonances in gold nanoparticle arrays," *Applied Physics Letters,* vol. 93, p. 3, Nov 2008.

[100] W. Zhou and T. W. Odom, "Tunable subradiant lattice plasmons by out-of-plane dipolar interactions," *Nature Nanotechnology,* vol. 6, pp. 423-427, Jul 2011.

[101] I. Gryczynski, J. Malicka, Z. Gryczynski, and J. R. Lakowicz, "Surface plasmon-coupled emission with gold films," *Journal of Physical Chemistry B,* vol. 108, pp. 12568-12574, Aug 2004.

[102] E. G. Matveeva, I. Gryczynski, A. Barnett, N. Calander, and Z. Gryczynski, "Red blood cells do not attenuate the SPCE fluorescence in surface assays," *Analytical and Bioanalytical Chemistry,* vol. 388, pp. 1127-1135, Jul 2007.

[103] J. S. Yuk, M. Trnavsky, C. McDonagh, and B. D. MacCraith, "Surface plasmon-coupled emission (SPCE)-based immunoassay using a novel paraboloid array biochip," *Biosensors and Bioelectronics,* vol. 25, pp. 1344-1349, Feb 15 2010.

[104] K. Toma, M. Vala, P. Adam, J. Homola, W. Knoll, and J. Dostalek, "Compact surface plasmon-enhanced fluorescence biochip," *OPTICS EXPRESS,* vol. 21, pp. 10121-10132, Apr 22 2013.

[105] T. Liebermann and W. Knoll, "Surface-plasmon field-enhanced fluorescence spectroscopy," *Colloids and Surfaces a-Physicochemical and Engineering Aspects,* vol. 171, pp. 115-130, Oct 2000.

[106] J. Dostalek, A. Kasry, and W. Knoll, "Long range surface plasmons for observation of biomolecular binding events at metallic surfaces," *Plasmonics,* vol. 2, pp. 97-106, 2007.

[107] C. J. Huang, J. Dostalek, and W. Knoll, "Optimization of layer structure supporting long range surface plasmons for surface plasmon-enhanced fluorescence spectroscopy biosensors," *Journal of Vacuum Science and Technology B,* vol. 28, pp. 66-72, 2010.

[108] K. Toma, J. Dostalek, and W. Knoll, "Long range surface plasmon-coupled fluorescence emission for biosensor applications," *OPTICS EXPRESS,* vol. 19, pp. 11090-11099, Jun 2011.

[109] S. C. Kitson, W. L. Barnes, J. R. Sambles, and N. P. K. Cotter, "Excitation of molecular fluorescence via surface plasmon polaritons," *Journal of Modern Optics,* vol. 43, pp. 573-582, Mar 1996.

[110] W. Knoll, M. R. Philpott, and J. D. Swalen, "Emission of light from Ag metal gratings coated with dye monolayer assemblies," *Journal of Chemical Physics,* vol. 75, pp. 4795-4799, 1981.

[111] K. Tawa, M. Umetsu, T. Hattori, and I. Kumagai, "Zinc Oxide-Coated Plasmonic Chip Modified with a Bispecific Antibody for Sensitive Detection of a Fluorescent Labeled-Antigen," *Analytical Chemistry,* vol. 83, pp. 5944-5948, Aug 2011.

[112] L. Touahir, E. Galopin, R. Boukherroub, A. C. Gouget-Laemmel, J. N. Chazalviel, F. Ozanam, and S. Szunerits, "Localized surface plasmon-enhanced fluorescence spectroscopy for highly-sensitive real-time detection of DNA hybridization," *Biosensors and Bioelectronics,* vol. 25, pp. 2579-2585, Aug 2010.

[113] Z. D. Xu, Y. Chen, M. R. Gartia, J. Jiang, and G. L. Liu, "Surface plasmon enhanced broadband spectrophotometry on black silver substrates," *Applied Physics Letters,* vol. 98, p. 3, Jun 2011.

[114] E. G. Matveeva, Z. Gryczynski, and J. R. Lakowicz, "Myoglobin immunoassay based on metal particle-enhanced fluorescence," *Journal of Immunological Methods,* vol. 302, pp. 26-35, Jul 2005.

[115] M. Schmelzeisen, Y. Zhao, M. Klapper, K. Muellen, and M. Kreiter, "Fluorescence enhancement from individual plasmonic gap resonances," *Acs Nano,* vol. 4, pp. 3309-3317, Jun 2010.

[116] H. W. Yoo, J. M. Jung, S. K. Lee, and H. T. Jung, "The fabrication of highly ordered silver nanodot patterns by platinum assisted nanoimprint lithography," *Nanotechnology,* vol. 22, p. 7, Mar 2011.

[117] M. T. Zin, K. Leong, N.-Y. Wong, H. Ma, M. Sarikaya, and A. K. Y. Jen, "Surface-plasmon-enhanced fluorescence from periodic quantum dot arrays through distance control using biomolecular linkers," *Nanotechnology,* vol. 20, Jan 7 2009.

[118] W. Zhang, F. Ding, W. Li, Y. Wang, J. Hu, and S. Y. Chou, "Giant and uniform fluorescence enhancement over large areas using plasmonic nanodots in 3D resonant cavity nanoantenna by nanoimprinting," *Nanotechnology,* vol. 23, p. 225301, 2012.

[119] J. W. Attridge, P. B. Daniels, J. K. Deacon, G. A. Robinson, and G. P. Davidson, "Sensitivity enhancement of optical immunosensors by the use of a surface-plasmon resonance fluoroimmunoassay," *Biosensors and Bioelectronics,* vol. 6, pp. 201-214, 1991.

[120] A. E. Vasdekis and G. P. J. Laporte, "Enhancing Single Molecule Imaging in Optofluidics and Microfluidics," *International Journal of Molecular Sciences,* vol. 12, pp. 5135-5156, Aug 2011.

[121] K. Tawa, H. Hori, K. Kintaka, K. Kiyosue, Y. Tatsu, and J. Nishii, "Optical microscopic observation of fluorescence enhanced by grating-coupled surface plasmon resonance," *Optics Express,* vol. 16, pp. 9781-9790, Jun 23 2008.

[122] A. Renier, T. Mangeat, H. Benalia, C. Elie-Caille, C. Pieralli, and B. Wacogne, "Gold/silica thin film for biosensors applications: Metal enhanced fluorescence," *Laser Physics,* vol. 20, pp. 591-595, Mar.

[123] D. Volpati, A. E. Job, R. F. Aroca, and C. J. L. Constantino, "Molecular and morphological characterization of bis benzimidazo perylene films and surface-enhanced phenomena," *Journal of Physical Chemistry B,* vol. 112, pp. 3894-3902, Apr 2008.

[124] J. A. Fan, C. H. Wu, K. Bao, J. M. Bao, R. Bardhan, N. J. Halas, V. N. Manoharan, P. Nordlander, G. Shvets, and F. Capasso, "Self-assembled plasmonic nanoparticle clusters," *Science,* vol. 328, pp. 1135-1138, May 2010.

[125] P. Bharadwaj and L. Novotny, "Plasmon-enhanced photoemission from a single Y(3)N@C(80) fullerene," *Journal of Physical Chemistry C,* vol. 114, pp. 7444-7447, Apr 2010.

[126] Y. Fu, J. Zhang, and J. R. Lakowicz, "Large enhancement of single molecule fluorescence by coupling to hollow silver nanoshells," *Chemical Communications,* vol. 48, pp. 9726-9728, 2012.

[127] K. Ray, R. Badugu, and J. R. Lakowicz, "Polyelectrolyte layer-by-layer assembly to control the distance between fluorophores and plasmonic nanostructures," *Chem Mater,* vol. 19, pp. 5902-5909, Nov 27 2007.

[128] A. G. Brolo, S. C. Kwok, M. G. Moffitt, R. Gordon, J. Riordon, and K. L. Kavanagh, "Enhanced fluorescence from arrays of nanoholes in a gold film," *Journal of the American Chemical Society,* vol. 127, pp. 14936-14941, Oct 2005.

[129] K. Tawa, X. Q. Cui, K. Kintaka, J. Nishii, and K. Morigaki, "Sensitive bioimaging in microfluidic channels on the plasmonic substrate: Application of an enhanced fluorescence based on the reverse coupling mode," *Journal of Photochemistry and Photobiology a-Chemistry,* vol. 221, pp. 261-267, Jun 2011.

[130] A. F. Oskooi, D. Roundy, M. Ibanescu, P. Bermel, J. D. Joannopoulos, and S. G. Johnson, "MEEP: A flexible free-software package for electromagnetic simulations by the FDTD method," *Computer Physics Communications,* vol. 181, pp. 687-702, Mar 2010.

[131] A. Taflove and S. C. Hagness, *Computational Electrodynamics - The Finite-Difference Time-Domain Method*, Third Edition ed.: Artech House, 2005.

[132] A. F. Oskooi, L. Zhang, Y. Avniel, and S. G. Johnson, "The failure of perfectly matched layers, and towards their redemption by adiabatic absorbers," *OPTICS EXPRESS,* vol. 16, pp. 11376-11392, Jul 21 2008.

[133] B. E. A. Saleh and M. C. Teich, *Fundamentals of photonics*: John Wiley and Sons, Inc., 1991.

[134] M. H. Chowdhury, J. Pond, S. K. Gray, and J. R. Lakowicz, "Systematic computational study of the effect of silver nanoparticle dimers on the coupled emission from nearby fluorophores," *Journal of Physical Chemistry C,* vol. 112, pp. 11236-11249, Jul 2008.

[135] M. Slootsky and S. R. Forrest, "Full-wave simulation of enhanced outcoupling of organic light-emitting devices with an embedded low-index grid," *Applied Physics Letters,* vol. 94, Apr 20 2009.

[136] A. Chutinan, K. Ishihara, T. Asano, M. Fujita, and S. Noda, "Theoretical analysis on light-extraction efficiency of organic light-emitting diodes using FDTD and mode-expansion methods," *Organic Electronics,* vol. 6, pp. 3-9, Feb 2005.

[137] W. L. Barnes, "Fluorescence near interfaces: the role of photonic mode density," *Journal of Modern Optics,* vol. 45, pp. 661-699, Apr 1998.

[138] K. A. Neyts, "Simulation of light emission from thin-film microcavities," *Journal of the Optical Society of America a-Optics Image Science and Vision,* vol. 15, pp. 962-971, Apr 1998.

[139] C. Vieu, F. Carcenac, A. Pepin, Y. Chen, M. Mejias, A. Lebib, L. Manin-Ferlazzo, L. Couraud, and H. Launois, "Electron beam lithography: resolution limits and applications," *Applied Surface Science,* vol. 164, pp. 111-117, Sep 2000.

[140] A. A. Tseng, "Recent developments in micromilling using focused ion beam technology," *Journal of Micromechanics and Microengineering,* vol. 14, pp. R15-R34, Apr 2004.

[141] A. Boltasseva, "Plasmonic components fabrication via nanoimprint," *Journal of Optics a-Pure and Applied Optics,* vol. 11, p. 11, Nov 2009.

[142] S. Y. Chou, P. R. Krauss, W. Zhang, L. J. Guo, and L. Zhuang, "Sub-10 nm imprint lithography and applications," *Journal of Vacuum Science & Technology B,* vol. 15, pp. 2897-2904, Nov-Dec 1997.

[143] K. Toma, M. Toma, P. Adam, M. Vala, J. Homola, W. Knoll, and J. Dostalek, "Surface plasmon-coupled emission on plasmonic Bragg gratings," *Optics Express,* vol. 20, pp. 14042-14053, 2012.

[144] J. Dostalek and W. Knoll, "Biosensors based on surface plasmon-enhanced fluorescence spectroscopy," *Biointerphases,* vol. 3, pp. FD12-FD22, Sep 2008.

[145] M. Bauch, S. Hageneder, and J. Dostalek, "Plasmonic amplification for bioassays with epi-fluorescence readout," *OPTICS EXPRESS,* vol. 22, pp. 32026-32038, 2014.

[146] N. Bowden, W. T. S. Huck, K. E. Paul, and G. M. Whitesides, "The controlled formation of ordered, sinusoidal structures by plasma oxidation of an elastomeric polymer," *Applied Physics Letters,* vol. 75, pp. 2557-2559, Oct 1999.

[147] B. Auguie and W. L. Barnes, "Diffractive coupling in gold nanoparticle arrays and the effect of disorder," *Optics Letters,* vol. 34, pp. 401-403, Feb 2009.

[148] B. Auguie and W. L. Barnes, "Collective resonances in gold nanoparticle arrays," *Physical Review Letters,* vol. 101, p. 4, Oct 2008.

[149] G. Vecchi, V. Giannini, and J. G. Rivas, "Shaping the Fluorescent Emission by Lattice Resonances in Plasmonic Crystals of Nanoantennas," *Physical Review Letters,* vol. 102, p. 4, Apr 2009.

[150] G. Vecchi, V. Giannini, and J. G. Rivas, "Surface modes in plasmonic crystals induced by diffractive coupling of nanoantennas," *Physical Review B,* vol. 80, p. 4, Nov 2009.

[151] N. Papanikolaou, "Optical properties of metallic nanoparticle arrays on a thin metallic film," *Physical Review B,* vol. 75, Jun 2007.

[152] Y. Z. Chu and K. B. Crozier, "Experimental study of the interaction between localized and propagating surface plasmons," *Optics Letters,* vol. 34, pp. 244-246, Feb 2009.

[153] A. Ghoshal and P. G. Kik, "Theory and simulation of surface plasmon excitation using resonant metal nanoparticle arrays," *Journal of Applied Physics,* vol. 103, p. 8, Jun 2008.

[154] W. R. Holland and D. G. Hall, "Frequency Shifts of an Electric-Dipole Resonance near a Conducting Surface," *Physical Review Letters,* vol. 52, pp. 1041-1044, 1984.

[155] P. Nordlander and E. Prodan, "Plasmon hybridization in nanoparticles near metallic surfaces," *Nano Letters,* vol. 4, pp. 2209-2213, Nov 2004.

[156] S. McDaniel and S. Blair, "Increased OLED radiative efficiency using a directive optical antenna," *OPTICS EXPRESS,* vol. 18, pp. 17477-17483, Aug 2010.

[157] M. A. Kats, D. Sharma, J. Lin, P. Genevet, R. Blanchard, Z. Yang, M. M. Qazilbash, D. N. Basov, S. Ramanathan, and F. Capasso, "Ultra-thin perfect absorber employing a tunable phase change material," *Applied Physics Letters,* vol. 101, p. 5, Nov 2012.

[158] A. D. Rakic, A. B. Djurisic, J. M. Elazar, and M. L. Majewski, "Optical properties of metallic films for vertical-cavity optoelectronic devices," *Applied Optics,* vol. 37, pp. 5271-5283, Aug 1998.

[159] T. Ruckstuhl, M. Rankl, and S. Seeger, "Highly sensitive biosensing using a supercritical angle fluorescence (SAF) instrument," *Biosensors & Bioelectronics,* vol. 18, pp. 1193-1199, Aug 2003.

[160] T. Ruckstuhl and D. Verdes, "Supercritical angle fluorescence (SAF) microscopy," *OPTICS EXPRESS,* vol. 12, pp. 4246-4254, Sep 2004.

[161] G. Barbillon, "Plasmonic Nanostructures Prepared by Soft UV Nanoimprint Lithography and Their Application in Biological Sensing," *Micromachines,* vol. 3, pp. 21-27, Mar 2012.

[162] L. Feuz, P. Jonsson, M. P. Jonsson, and F. Hook, "Improving the limit of detection of nanoscale sensors by directed binding to high-sensitivity areas," *Acs Nano,* vol. 4, pp. 2167-2177, Apr 2010.

Curriculum vitae

Not available in electronic version.

Publications

M. Bauch, S. Hageneder, J. Dostalek,
Plasmonic amplification for fluorescence assays with epifluorescence readout,
Optics Express (2014) 22(26) pp 32026-32038

M. Bauch, K. Toma, M. Toma, Q. Zhang, J. Dostalek,
Surface plasmon-enhanced fluorescence biosensors: a review,
Plasmonics (2014) 9(4) pp 781-799

M. Bauch, J. Dostalek,
Collective localized surface plasmon-enhanced fluorescence for high performance biosensors,
Optics Express (2013) 21(17) pp 20470-20483

A. A. Kordyuk, T. K. Kim, V. B. Zabolotnyy, D. V. Evtushinsky, **M. Bauch**, C. Hess, B. Büchner, H. Berger, S. V. Borisenko,
Photoemission-induced gating of topological insulators,
Phys. Rev. B (2011) 83 pp 081303